Nanocalorimeter Platform for Point-of-Care Medical Applications

By

Evan Kazura

Dissertation

Submitted to the Faculty of the

Graduate School of Vanderbilt University

in partial fulfillment of the requirements

for the degree of

DOCTOR OF PHILOSOPHY

in

Biomedical Engineering

May 31, 2020

Nashville, Tennessee

Approved:

Franz Baudenbacher, Ph.D., Chair

Frederick Haselton, Ph.D.

Craig Duvall, Ph.D.

William Grissom, Ph.D.

Raymond Mernaugh, Ph.D.

Acknowledgements

First and foremost, I would like to thank my family and my girlfriend, Kristina. I would not have made it to this point without their love, support, and guidance every day. I cannot properly express how appreciative I am for the environment and opportunities my mom and dad created for me, which have allowed me to pursue my passions and are responsible for everything I have accomplished. I am proud and thankful for my brothers, Andrew and Adam, who put up with my intermittent contact and make every moment we have together as a family special. Kristina, you inspire me each day to not just be a better researcher, but to be an informed and active citizen, a bigger part of my community, and a better friend. And to the rest of my family and Kristina's family, thank you for your support, prayers, and help throughout this journey.

Thank you, Franz. Your guidance during my time at Vanderbilt has been invaluable. Your ability to see problems clearly and solve them elegantly and efficiently will be the most important skill I take away from my graduate studies. Thank you to my committee for accepting this work. Thank you, Ray, for being such a great partner in our research and indispensable source of knowledge and expertise. And I would like to thank Dr. Haselton for having an open door for me and lending the resources of his lab whenever I asked. Dr. Lowery and Dr. Russ, thank you for being understanding with me as your TA, and I appreciate the opportunities you trusted me with to grow as a teacher. Dr. Byram and the Byram lab, thank you for allowing me to intrude on your office space for so long. And I would also like to thank John Dunbar, who always had an answer for me, no matter what I asked of him.

I have been blessed with fantastic teachers for my entire life. Thank you, Professor Richard Goldberg, for advising me during my time at Carolina and helping me find what I love to do and crafting my major to match that. Thank you to Professor Rich Superfine, Dr. Jerome Carpenter, and the rest of CISMM, for bringing me into the world of research and showing me what it is all about. C. W. Stacks, you taught me so much more than high school physics. You helped foster a lifelong passion for science and learning outside the classroom, and a sense of service to my community. Ken Kneidel, you introduced me to the wondrous study of biology, and went above and beyond as my high school advisor. Tom Dubick, you took my fascination for taking apart and building things and steered me towards engineering, which has been a lifelong path so far.

I am so lucky to have the friends I do. When I think about my time at Vanderbilt, my foremost memories are with the people I have met here, who have made this an amazing time of my life. Jeremy, Tiffany, Kristy, Wilson, Kat, Megan, Frances, Meredith, Jake, Sinead, and Jaime, thank you for making the good times great and the rough times manageable. To Michael, Ben, Jeremy, Rob, Patrick, Jenn, Mary, Helen, Kaitlin, Zack, Clint, Stilwell, Dutra, H., Frank, Darvin, and David, thank you for making my four years in the best place on earth that much better. And with the daily texts/emails/groupmes/slacks coming in, I never had to give up the feeling of having all my best friends right down the hall. To my friends from Latin, having a friendship this long is special, and that is not lost on me. I appreciate everything you guys have done to make sure that bond is strong, through every phase of life. Matt, Austin, Carl, Drew, Bickers, and Ethan, I love you guys.

Table of Contents

Page

Copyright II
Acknowledgements III
Table of Contents IV
List of Figures VII
List of Tables IX

Chapter

I: Introduction To Nanocalorimeter Platform for Point-Of-Care Medical Applications 1

Introduction 1
Objective 2
Specific Aims 2
Background 3
Calorimetry *3*
Thermoelectric Sensor Theory *4*
Calorimeter Platform Properties *6*
Calorimeter Platform Calibration and Performance *8*
Modeling *10*
Biosensors *11*
Enzymes *12*
Point-of-Care *13*
Medical Applications - Phenylketonuria *15*
References 15

II: Microfabricated Calorimeters for Thermometric Enzyme-Linked Immunosorbent Assay in One-Nanoliter Droplets 23

Abstract 23
Introduction 24
Materials and Methods 27
Device Design *27*
Device Fabrication *29*
Device Operation *30*

Materials *31*
Surface Functionalization *31*
Detection of Trastuzumab *32*
Results and Discussion 33
Calorimeter Characterization *33*
Quantification of Trastuzumab *34*
Conclusions 35
References 36

III: Nano-Calorimetry Based Point of Care Biosensor for Metabolic Disease Management 39

Abstract 40
Introduction 40
Materials and methods 44
Reagents and materials *44*
Device modeling *45*
Device fabrication *46*
Device characterization *47*
Enzymatic measurements *48*
Results and discussion 49
Modeling Design Results *49*
Device performance *52*
Hydrogen peroxide assay *53*
Phenylalanine assay *55*
Conclusions 55
References 56

IV: A Capillary Perfused Nanocalorimeter Platform for Thermometric Enzyme-Linked Immunosorbent Assay with Attomole Sensitivity 58

Abstract 59
Introduction 59
Experimental Section 62
Nanocalorimeter Platform Layout *62*
Model Construction *65*
Model Operation and Data Processing *66*
Catalase Experiment *67*
Results and Discussion 67
Enzyme-Based Model Operation *67*
Validation of Numerical Model *69*

Model-Assisted TELISA *71*
Determining TELISA Limit of Detection *72*
Conclusion 73
References 74

V: Nanocalorimeter-Based Adaptable Point of Care Biosensor Platform 76

Abstract 77
Introduction 77
Methods 80
Results and Discussion 80
Wicking Fluid Handling *80*
Magnetic bead delivery *83*
Conclusion 86
References 86

VI: Conclusions and Future Research 88

Summary of Findings 88
Future Research 91

Appendix

A: COMSOL-Generated MATLAB Code for Finite Element Numerical Model 93

B: MATLAB Code 102

Calorimeter Platform Design Optimization 102
Catalase Model-assisted TELISA 104

List of Figures

Figure Page

Chapter I: Introduction to Nanocalorimeter Platform for Point-of-Care Medical Applications

1. Calorimetry properties diagram..... 6
2. Heat flux in a calorimeter..... 8

Chapter II: Microfabricated Calorimeters for Thermometric Enzyme-Linked Immunosorbent Assay in One-Nanoliter Droplets

1. TELISA steps 26
2. Microcalorimeter microfabrication steps 29
3. Baseline correction and τ calculation 31
4. Calorimeter optimization 33
5. Calorimeter characterization 34
6. Trastuzumab response..... 35
7. TELISA signal in PBS and serum..... 35

Chapter III: Nano-Calorimetry Based Point of Care Biosensor for Metabolic Disease Management

1. Differential nanocalorimeter layout 43
2. 3D model configuration for optimizing device sensitivity 44
3. Device characterization..... 45
4. Model predictions of sensitivity by channel dimensions..... 50
5. Junction separation modeling..... 50
6. Hydrogen peroxide diffusion modeling 51
7. Catalase assay 53
8. Phenylalanine assay 54

Chapter IV: A Capillary Perfused Nanocalorimeter Platform for Thermometric Enzyme-Linked Immunosorbent Assay with Attomole Sensitivity

1. Capillary-powered nanocalorimeter platform layout..... 63
2. 3D calorimeter platform model constructed in COMSOL Multiphysics 64
3. Modeled calorimeter response to enzymatic reaction..... 68
4. Enzyme deactivation in the model..... 70
5. Model-assisted TELISA 71
6. Limit of detection for catalase-based TELISA..... 72

Chapter V: Nanocalorimeter-Based Adaptable Point of Care Biosensor Platform

1. Diagram of paper wicking for multistep calorimetric assay 81
2. Filling artifact signals..... 82
3. Properties of filling artifacts for different volumes 83
4. Diagram of enzyme-based assay with magnetic bead capture 83
5. Capture of magnetic beads on channel perfusion..... 84

List of Tables

Table Page

Chapter I: Introduction to Nanocalorimeter Platform for Point-of-Care Medical Applications

1. Thermal conductivities of relevant materials 7
2. Comparison of different microcalorimeters 9
3. Selected enzymatically-catalyzed reactions 13

Chapter II: Microfabricated Calorimeters for Thermometric Enzyme-Linked Immunosorbent Assay in One-Nanoliter Droplets

1. Figure of merit for potential thermopile materials 28

Chapter III: Nano-Calorimetry Based Point of Care Biosensor for Metabolic Disease Management

1. Device properties 52

Chapter I: Introduction to Nanocalorimeter Platform for Point-of-Care Medical Applications

Introduction

Here we present the design and optimization of a point-of-care platform built around a microfabricated thermopile nanocalorimeter with capillary-powered fluidics for the quantification of biological reactions. Advances in microfabrication have given rise to calorimeters with smaller reaction volumes, which maximizes the sensitivity and reduces the time constant by reducing the thermal mass of the sample and measurement system. Our nanocalorimeters are capable of detecting heat in the nanojoule range with sub second resolution. The calorimeters are constructed on thin membranes made of the polymer Su-8, a thermally-isolating material that reduces heat flow away from the sensing apparatuses while providing a robust platform that withstands months of repeated use. The thermopiles are fabricated using standard microfabrication and photolithography techniques and transduce temperature gradients into a voltage difference. We use energy generated in enzymatic reactions to develop assays for the quantification of target analytes termed thermometric enzyme-linked immunosorbent assays (TELISA). By combining the capillary fluidics with magnetic bead capture to deliver the analyte to the reaction volume, the platform is adapted for point-of-care use. This makes it a prime candidate for biosensor applications that would benefit from being quantitative without the need for expensive assay read out systems. Our applications for the platform will focus on the sensitive quantification of trastuzumab in human serum and the monitoring of phenylalanine blood levels for the metabolic disorder phenylketonuria through the quantification of heat produced by enzyme-based reactions.

Objective

The goal of this work is to develop a nanocalorimeter platform and adapt techniques for point-of-care biomedical applications.

Specific Aims

Aim 1: Develop nanocalorimeter platform with capillary-driven fluid delivery.

The first aim of this dissertation was to design and produce highly sensitive differential thermopile calorimeters with on-chip fluid handling powered by capillary forces. Iterative heat flow modeling led to an optimized design capable of operation as an enzyme-based biosensor. This was accomplished through model assays quantifying a target analyte in a liquid sample through measuring the heat produced by an enzyme-catalyzed reaction. The proof of concept assays provided the base for improvement in the next aim.

Aim 2: Determine sensitivity on the calorimeter platform through finite element numerical modeling.

The second aim used comprehensive finite element modeling to investigate the full time course of the common hydrogen peroxide-catalase enzymatic reaction employed by TELISAs, as well as the heat flow and resulting signal from the reaction on the nanocalorimeter platform. Calibrating for changing enzyme parameters and determining enzyme amounts through modeling improved the robustness of a model TELISA. Successful completion of this aim predicted the viability and improved the assay sensitivity of the biosensor application pursued in aim 3.

Aim 3: Extraction of sample analyte and delivery to calorimeter for point-of-care biosensor operation.

The final aim simplified reagent delivery to optimize the nanocalorimeter platform for point-of-care operation. Pulling fluid through the microfluidic channel using wicking paper reduced noise from

the filling of the chamber, and magnetic bead capture and delivery of the target analyte allowed for hand-pipetting for all steps of the assay.

Background

Calorimetry

All reactions, whether molecular, chemical, or biological, include a transfer of energy according to the laws of thermodynamics. This energy flow is governed by the first law of thermodynamics:

$$\Delta U = Q - W$$

where ΔU is the change in internal energy, Q is the heat added or removed from the system, and W is the work performed on or by the system. In a closed system, U remains constant, so any work done either consume or produce heat. This heat can be measured and used to characterize the reaction.

The field of calorimetry pertains to the measurement of heat as a function of temperature. Applications of calorimetry include the study of heat and energy changes of chemical reactions [1], biological reactions [2] and metabolism [3], material deposition [4] [5] and phase changes [6], and molecular binding events [7] [8]. In order to compare the capabilities and effectiveness of different calorimeters, it is useful to establish the characterizing features of different calorimeter designs and modes of operations. The most common calorimetry techniques are differential thermal analysis, which measures temperature differences, and differential scanning calorimetry, which measures heat flow rate differences, each between a sample and a reference material [9] [10]. Isothermal titration calorimetry (ITC) is the method most used to explore the small amounts of energy produced by chemical reactions or biological reactions at the cellular or molecular level [11]. In one form of ITC, the reaction and a reference volume are maintained at a constant temperature above the environmental temperature using electrical heaters. A thermally conductive material directs heat generated by the

heater from the reaction volume to the environment requiring constant heating. Initiating an exothermic chemical reaction will require less heat generated by the heater to maintain the same temperature as the reference volume. Monitoring the current through at constant voltage across the heater allows for determination of the heat generated in the reaction [12]. With advances in microfabrication, calorimeter environments can be constructed that hold near adiabatic conditions while being sensitive enough to monitor the small amounts of heat produced by molecular or biological reactions at scales at the edge of modern detection [13]. This form of ITC is used to study reaction enthalpies including characterization of enzyme interactions and chemical reaction heat output profiles over time without external power compensation [14]. Thermal isolation of the reaction area maximizes heat flow to the temperature sensing elements of the calorimeter and minimizes reaction heat loss into the environment. Temperature sensing technologies include thermistors [15], resonance changes in microbeams [3], and thermoelectric sensors [16].

Thermoelectric Sensor Theory

The calorimeters described in this work are based on thermoelectric sensors, which produce a voltage as a response to a difference in temperature and thereby convert a thermal gradient into an electric signal. This method relies on the Seebeck effect, discovered by Thomas Seebeck in 1821 [16]. It states that if a temperature difference is applied to a length of conducting or semiconducting material, phonons drag either electrons or holes, depending on the material property, from the hot end to the cold end [17]. This causes a charge to build up at the ends of the material. By joining two dissimilar materials together and applying a temperature difference at their junction, the difference in the amount of charge carriers produces an open circuit voltage between the cold ends [16]. The magnitude of this voltage potential ΔV depends on the magnitude of the temperature difference ΔT and the properties of the two materials [18]. This is expressed in the equation:

$$\Delta V = S\Delta T$$

where S is the combined Seebeck coefficient of the two materials, in V/K. The joining of two materials with differing Seebeck coefficients is known as a thermocouple. The voltage produced by a single thermocouple is quite small, but by placing them in series, their respective ΔV is additive and allows for higher sensitivity. Thermocouples in series are known as thermopiles. Thermocouples have several advantages over thermistors or resonators for measuring the small temperature changes in isothermal titration calorimetry. Relevant materials show linearity over temperature difference ranges on the order of 60 degrees K [18]. Voltage is self-generated by the sensing apparatus, so it does not suffer from self-heating issue of thermistors. Additionally, thermopiles are easy to produce with modern thin film deposition and patterning techniques.

The effectiveness of the thermocouple is governed by a combination of the materials' Seebeck coefficients, resistivities, and thermal conductivities. The thermocouple's effective Seebeck coefficient is the difference between the Seebeck coefficients of each material. Materials with a high effective S make for the most sensitive thermopiles. However, materials with high thermal conductance will contribute to the heat loss in specific calorimeters. Additionally, since the thermopiles are resistors which self-generate voltage, Johnson-Nyquist noise represents the limiting factor to the limit of detection of the calorimeter. The noise is white and can be described by the power spectral noise density:

$$V_n = \sqrt{4k_B TR}$$

where k_b is the Boltzmann's constant, T is the temperature of the resistor, and R is the resistance of the thermopile. Therefore, the most sensitive thermoelectric sensors use thermocouple materials that combine high effective S, low resistance, and low thermal conductance.

Calorimeter Platform Properties

Overall calorimeter device performance can be defined by the power sensitivity P_{sens} and response time τ. Device sensitivity P_{sens} (V/W) is the combination of thermopile Seebeck coefficient S_{tot} (V/K), which relates the amount of heat input to the magnitude of the output signal, and the heat flux away from the sensing area G_{tot} (W/K), which dictates the amount of heat lost to the environment.

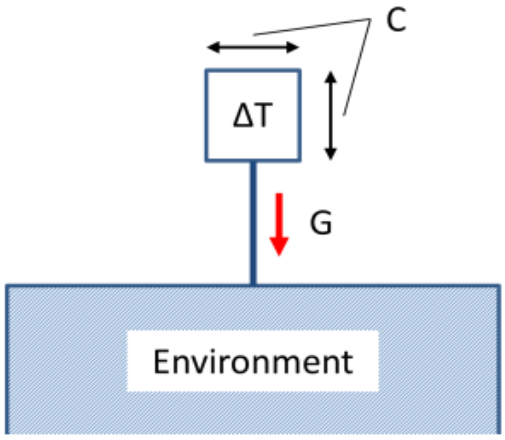

Figure 1. Calorimetry properties diagram. For a given change in heat for a system ΔQ, a change in temperature ΔT occurs scaled by the thermal capacity of the system C. The amount of ΔT measured by the calorimeter is determined by the thermal flux G away from the sensing apparatus and to the environment outside the system.

$$P_{sens} = S_{tot}/G_{tot}$$

Calorimeters featuring a high S_{tot} transduce small temperature differences into detectable output signals. A device's G_{tot} is composed of fluxes through the thermopiles, supporting substrate, air, and radiation (Figure 2). By minimizing thermal conductance away from the sample, the reaction heat remains at the sensing junctions of the thermoelectric sensor for more time. Minimization of these fluxes is accomplished by reducing the cross sections, the design of fluidics and selection of the device materials surrounding the sample. An open chamber or freestanding sample drop limits the surface area of sample contact with the device material, taking advantage of the low thermal conductance of air. Open chambers require precise sample placement and suffer from quick evaporation of small sample volumes, limiting sensing times and introducing baseline drift to the signal. Closed channels and microfluidic channels increase the thermal flux away from the sample but simplify sample handling.

Material	Thermal Conductivity (W/(m*K))
Silicon (bulk) [19]	156
Silicon Dioxide (thin film) [20]	1.03
Silicon Nitride (thin film) [21]	9
Su-8 (thin film) [22]	0.3
Air (bulk) [23]	0.03

Table 1. Thermal conductivities of relevant materials for microfabrication of thin membrane calorimeters.

The most sensitive calorimeters place the reaction volumes on thin membranes, reducing G_{tot} by limiting the cross section of the material (Table 1). Traditionally silicon nitride and silicon dioxide have been used as membrane materials due to their strength and compatibility with microfabrication techniques. Using materials with lower thermal conductivities, such as a polymer, can reduce membrane heat flux by as high as a factor of 30 [21]. Recent calorimeters have used parylene-C or Su-8 polymer membranes to achieve high sensitivity [13] [22]. In particular, Su-8 is a well-suited membrane material as it possesses a very low thermal conductivity, is patternable with standard photolithography techniques, withstands high temperatures, and is resistant to all but the harshest chemicals [24].

The other defining characteristic for the calorimeter is the response time to heat input, represented by the time constant τ. Reactions that are quick or have distinct steps in time are best recorded by calorimeters with a fast response time. A device's τ is inversely related to G_{tot} by the following equation.

$$\tau = C_{tot}/G_{tot}$$

C_{tot} is the total specific heat capacity of the sensing area, including the sample volume. It relates the amount of energy absorbed by the reaction volume to the resulting temperature change of the materials. For calorimeters with sensing areas located on thin membranes, this can functionally be reduced to the heat capacity of the sample itself.

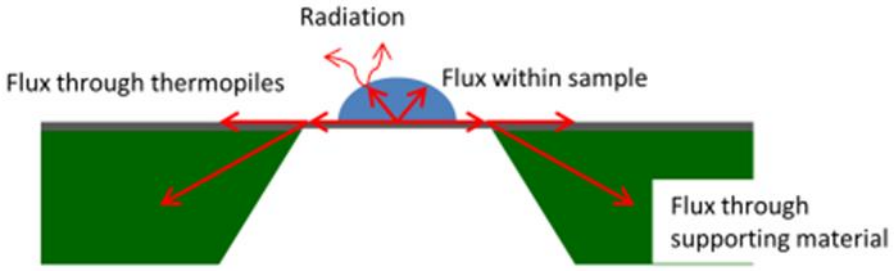

Figure 2. Heat flux in a calorimeter. The heat flux away from the sensing area of a calorimeter is a critical property that affects the power sensitivity and the response time of the device. In a thin membrane thermopile calorimeter, heat is primarily drawn away from the reaction site through the membrane and thermopiles and into the supporting material. This is due to the very low thermal conductance of air compared to most materials. Flux through the membrane is minimized by reducing the thickness and using low conductance materials.

Calorimeter Platform Calibration and Performance

Characterization of calorimeter performance is best done by experimental measurement of the parameters τ and P_{sens}. From those, G_{tot} and C_{tot} can be calculated, giving a full picture of the expected response over time to a specific input of heat. The time constant can be measured directly by heating the sample with a built-in resistive heater or laser and measuring the time required for the temperature to reach a steady state. P_{sens} is determined experimentally by inputting a known amount of energy into the system and measuring the resulting output signal. This can be done in the same manner as the τ measurement, but electrical heaters contribute to the heat loss and it is difficult to determine the exact amount of optical energy adsorbed by the calorimeter from exposing the membrane to a laser beam. The most accurate method closest to our application is to perform a well-characterized reaction on the calorimeter, such as the injection of acid into a drop of base [25]. A review of the modern

Source		Chamber		Configuration			Operation		
Group	Year	Type	Volume (nL)	Sensing Method	Operation Mode	Sample Handling	Responsivity and Thermal Insulation	Response Time (ms)	Resolution
Penn State	2004-2005 [26] [27]	Closed	15	Polysilicon/ gold thermopile	Isothermal	Syringe pump	0.94 V/W, 5,000 µW/K	1.6	300 nW
Katholieke Universiteit Leuven	2000 [28]	Open	10^5-10^7	Aluminum/ polysilicon thermopile	Isothermal	Micropipette	20 V/W, 5,000 µW/K	70,000	5,000 nW
University of Glasgow	2002 [29]	Open	0.75	Gold/ nickel thermopile	Isothermal	Micropipette	100 µW/K	12	13 nW
Scripps Palo Alto Research Center	2004-2008 [30] [31]	Open	500	Amorphous silicon thermistor/ vanadium oxide	Isothermal	Electrostatic merging	1000 µW/K	1,300	100 nW
Columbia University	2008-2019 [32] [33] [34]	Closed	1,000	Antimony-bismuth thermopile	Temperature scanning/ isothermal	Syringe pump	4-8 V/W, 1000 µW/K	1,500	20 nW
Caltech University/ KAIST	2009-2019 [13] [35]	Closed	3.5	Gold-nickel thermopile/ vanadium oxide	Isothermal	Multilevel microfluidics	7.1 V/W, 6.7-12 µW/K	1,300	4.2-10 nW
Marquette University	2014 [36]	Closed	200	Nickel RTD	Differential scanning/ isothermal		58.87 K/W	1,330	N/A
Virginia Tech	2016-2019 [37] [38] [39]	Closed	1,000	Vanadium oxide	Temperature scan	Syringe	6 V/W, 800 µW/K	7,200	35 nW
TU Bergakademie Freiberg/ Eurotronics	2005-2019 [40] [41] [42] [43] [44] [45] [46] [47] [48] [49]	Closed	10,000	BiSb-Sb thermopile	Isothermal	Micropipette	4-6 V/W, 30,000 µW/K	16,000	10-50 nW
Xensor Integration	2012-2016 [50] [51]	Closed	15	Silicon thermopile	Fast scanning	Syringe	5.5 V/W, 2 kK/W		1000 nW
Tohoku University	2016-2019 [52] [53] [54] [55] [56]	Closed		Silicon thermopile, vanadium oxide	Isothermal		0.44 V/W	20	0.5 mK/$\sqrt{}$Hz
Vanderbilt University	2008-2019 [57] [58] [59] [60]	Open	2.5-50	Titanium-bismuth thermopile	Isothermal	Micropipette	3-80 V/W, 65-220 µW/K	95	0.375 nW
Vanderbilt University	2015-2019 [59] [61]	Closed	470	Titanium-bismuth thermopile	Isothermal	Hand-pipette	7.2 V/W, 300 µW/K	300	1.4 nJ/$\sqrt{}$Hz

Table 2. Comparison of different microcalorimeters. Adapted *[59] [13] [62]*

microcalorimeters and their characteristics are shown in Table 2. Generally, open chamber calorimeters feature the best resolution and response time. However, the closed calorimeters from

Columbia University, Caltech University, and Virginia Tech combine good response times on the order of seconds with 4.2-35 nW resolutions. Our closed calorimeter features the best in both of those integral characteristics, with a resolution of 1.4 nW and a response time of 300 ms.

Modeling

Biomedical and engineering problems, such as designing a microcalorimeter platform or interpreting biological reactions for an assay, are complex systems. One approach to study these systems is to represent them in a physical or mathematical model [63]. Pertinent for this work, mathematical modeling simulates the system's response to relevant inputs, allowing for fast design choices for instruments, techniques, applications, and experiments before running time-consuming tests with potentially rare or expensive supplies. Approximating the system as a collection of a finite number of well-defined components makes complicated problems solvable with modern computers [64]. Finite Element Analysis (FEA) divides the system as a mesh of nodes, dividing a large or complicated system into discrete partitions with more easily solvable conditions. The condition to a node is affected by the previous condition, adjacent nodes, and the mathematical equations governing the properties. In this way, the total solution of the system is found as the assembly of the nodes individually solved as a standard discrete problem [64]. The Finite Element Method (FEM) of discretization divides up the system in a flexible manner [63]. By placing more nodes in regions of interest, more detailed study can occur. Conversely, a coarser mesh lessens computing requirements. With software like COMSOL Multiphysics, 3D models of the calorimeter platform can be built to simulate multiple properties simultaneously. By defining material properties of the platform and a reaction within the microfluidic channel volume, FEA was used in simulating analyte diffusion in a liquid, reaction kinetics in a 3D volume, and heat flow [65]. COMSOL and MATLAB combine these FEA approaches in a single model and can be automated over variables including physical dimensions of the modelled platform design, analyte and enzyme concentrations, and reaction kinetics.

Biosensors

Biosensors are devices that incorporate biological systems to detect and quantify chemicals. The most commonly used biological systems are antibodies or enzymes, which are used to interact with the target analytes. Biosensing was first proposed by Clark and Lyons in 1962, who designed a system to detect blood glucose levels by flowing blood through a glucose oxidase-containing membrane located on an electrode. The enzyme converts glucose to gluconic acid, generating H_2O_2 near the electrode, which gets converted in an electrochemical reaction to a current [66]. Biosensors using enzymatic methods of chemical recognition feature high selectivity and sensitivity [67]. Enzymatic biosensors often use enzymes to interact directly with the target chemical, eliciting a change in pH, color, fluorescence, or temperature that can be measured by the device. Enzyme linked immunosorbent assays (ELISAs) have become the gold standard for measuring antibodies and antigens in biological samples [68]. Of the many commercially available microtiter-based ELISA kits, most utilize an enzyme linked to a detecting antibody to produce a signal that can be quantified using a microtiter plate reader. The need to increase sensitivity and reduce sample consumption and assay time drives research toward a rapid, low-volume, direct readout ELISA system [69]. Mattiasson et al was the first to create an ELISA system with a calorimetric readout, termed Thermometric Enzyme Linked Immunosorbent Assay (TELISA). The original TELISA system was based on inhibition binding of a catalase linked albumin to an antibody coated calorimetry column [70]. These flow through systems required a large sample volume (>0.5 ml) and the use of temperature-controlled thermistor columns, but sensitivity to the µg/ml level for insulin, human IgG, and albumin were achieved [71]. However, in the years following, fluorescent and chemiluminescent ELISA systems achieved much higher sensitivity, so TELISA has seen little use in the past decade.

Recent advances in chip calorimetry using standard Micro-ElectroMechanical Systems (MEMS) techniques have pushed the limits of heat-sensing capabilities. Chip calorimeters miniaturize the

calorimetry process, which reduces sample consumption and device time constants, allowing for study of cellular and molecular level interactions. Microcalorimeters are used in the characterization of biological systems and interactions, as well as replacing fluorescence and secondary markers in concentration assays. These calorimeters hold the potential for designs of TELISA systems competitive with fluorescent and chemiluminescent ELISAs [60].

Enzymes

The primary transducers for our thermal signals are enzymes. Enzymes are proteins used to catalyze biological reactions. This catalysis can speed up the rate of reactions by factors upwards of 10^9 [72]. The specificity of most enzymes makes them well suited for use in biosensors [73]. Many different biological assays rely on enzyme-catalyzed reactions to effect a change, producing a signal. Signals can take the form of a color change, pH change, fluorescence, bioluminescence, chemiluminescence, or heat, for example [73]. Enzymatic reactions can be studied using the Gibbs equation to find the change in energy:

$$\Delta G = \Delta H - T\Delta S$$

where, at a constant temperature, ΔG is free energy, ΔH is the total heat change, T is the temperature, and ΔS is the change in entropy. The total heat change, or reaction enthalpy, produces any change in temperature, the quantification of which forms the basis for all calorimetric biosensors [74]. When selecting enzyme-catalyzed reactions for a biosensor assay, a reaction that is exergonic (-ΔG) near room temperature is preferred to ensure the reaction will proceed towards the products [59]. Additionally, rates of the enzymatic reactions are governed by the Michaelis-Menten equation:

$$v = \frac{k_{cat}[E_0][S]}{K_m + [S]}$$

where v is the overall reaction velocity, k_{cat} is the maximum turnover rate, K_m is the substrate concentration at which the reaction rate is half the k_{cat} value, $[E_0]$ is the enzyme concentration, and [S] is

the substrate concentration. Selecting an enzymatic reaction with fast kinetic properties and a high ΔH for enzyme-based assays allows for pushing the limits of detections of target analytes. Table 3 includes some of the most common enzymes and reactions used in calorimetric biosensors, as well as the characteristics that make them advantageous.

Reaction	**ΔH (kJ/mol)**	**Enzyme**	**K_m (mM)**	**K_{cat}/K_m ($mM^{-1}s^{-1}$)**
$H_2O_2 \leftrightarrow H_20 + ½\ O_2$	-98	Catalase	1.1	3.6×10^6
$3\ H_2O_2 + 2$ OPD $\leftrightarrow 6\ H_20$ + DAP	-297	Horseradish Peroxidase (HRP)	0.6	2.5×10^3
$C_6H_{12}O_6 + ½\ O_2 \leftrightarrow C_6H_{10}O_6 + H_20_2$	-80	Glucose Oxidase (GOx)	6.0	3.0×10^2
$CO_2 + H_2O \leftrightarrow H_2CO_3$	-20	Carbonic Anhydrase	0.012	8.3×10^7
L-phenylalanine ↔ trans-cinnamic acid + NH_3	+25	Phenylalanine Ammonia-Lyase (PAL)	0.2	6.0×10^2
$2\ NH_3 + CO_2 \leftrightarrow$ urea + H_20	+58	Urease	12	2.5×10^1

Table 3. Select enzymatically-catalyzed reactions and their properties *[75] [76] [77] [78] [71] [79]*. Adapted *[59]*

Point-of-Care

The expansion of point-of-care (POC) diagnostics over the past decade has allowed for near instantaneous results for many common blood tests that previously required expensive laboratory equipment and personnel time. With a worldwide market value of over $15.5 billion in 2013, POC diagnostics represents one of the fastest growing health care technology segments [80]. The largest POC segment, blood glucose monitoring, allows patients themselves to monitor blood glucose levels anywhere [81] [82] [83]. The information provided by the testing is essential for diabetic patients to regulate their glucose levels through medication and diet.

Biosensors are the basis for most POC diagnostic technologies. An enzymatic reaction with the analyte of interest produces a quantifiable signal transduced by one of several different methods; amperometric, optical, calorimetric, or acoustic to name a few [84] [12]. Calorimetry is an attractive

detection method as most enzymatic reactions produce heat on the order of 20-300 kJ/mole substrate and are measured directly, not requiring the use of secondary or labeling reactions for transduction as most optical methods do [74]. Calorimetry is based on a temperature measurement and senses heat changes from chemical or physical processes present at the sensor, necessitating the elimination of noise from side reactions and temperature fluctuations [85]. Calorimetric biosensors of the past relied on flow-through columns with enzymes immobilized on a support matrix and thermistors for temperature sensing [84]. These required large sample volumes (>0.5 ml), temperature controls, complex pumping systems, and were only suited to the laboratory setting [85]. Many were successful in measuring sub-milimolar concentrations of common blood analytes like cholesterol, urea, lactate, glucose, and ethanol [71] [86]. The current trend is towards miniaturization, microfluidic sample handing, and on-chip thermoelectric based sensing [87]. In this way sample volume requirements are reduced to the microliter range and minimum detectable energies approaching 1 nJ are possible [13] [58]. A few calorimetric biosensors suited to POC have been developed pertaining to the measurement of blood glucose or urine urea due to the large enthalpy changes associated with these reactions (-80 and -61 kJ/mol) [88] [89]. In the case of Davaji and Lee, a thin film resistive temperature detector is employed, with a minimum detectable temperature change of 26 mK and noise limited minimum glucose concentration of 1.51 mM. A paper strip held the glucose oxidase enzyme in close proximity to the sensing surface, however enzyme was added to the flow strip at the beginning of each measurement, and evaporative effects caused a large drift in the calorimeter signal. Lai and Tadigadapa's device relied on a Y-cut quartz resonator for temperature sensing, giving higher temperature sensitivity. However, the entire device had to be placed in a 37 ˚C oven during measurements, microfluidic pumping systems were required, and the uncertainty in their urea detection results were too high for reliable use. In order to create a user-friendly calorimeter based POC device,

common mode temperature signals must be eliminated, temperature sensitivity increased, sample volume reduced, liquid handing automated, and be insensitive to user error.

Medical Applications - Phenylketonuria

Phenylketonuria (PKU) represents another disease where at-home monitoring is needed to help effectively manage the disease. Affecting 1 in 15,000 people worldwide, PKU prevents the metabolism of the essential amino acid phenylalanine (Phe), leading to high blood concentrations that can cause mental retardation if not treated through diet and/or enzyme replacement therapy [90]. Though much faster and more accurate than the bacterial inhibition assays of the 1960's, tandem mass spectrometry (MS/MS) testing of blood Phe levels is still limited to larger scale clinical laboratories [91]. At home Phe monitoring to dictate dosing and diet would save patients from constant visit to clinics and greatly improve their quality of life. With new enzyme replacement therapies for PKU undergoing human clinical trials, the need for Phe monitoring with immediate results to dictate dosing and diet is even greater.

References

[1] B. Grob and R. Riesen, "Reaction calorimetry for the development of chemical reactions," *Thermochimica Acta,* vol. 114, no. 1, pp. 83-90, 1987.

[2] M. L. Bianconi, "Calorimetry of enzyme-catalyzed reactions," *Biophysical Chemistry,* vol. 126, no. 1-3, pp. 59-64, 2007.

[3] N. Inomata, M. Toda, M. Sato, A. Ishijima and T. Ono, "Pico calorimeter for detection of heat produced in an individual brown fat cell," *Applied Physics Letters,* vol. 100, no. 15, 2012.

[4] H. Hikawa, M. Oguni and H. Suga, "Construction of an adiabatic calorimeter for a vapor-deposited sample and thermal characterization of amorphous butyronitrile," *Journal of Non-Crystalline Solids,* vol. 101, no. 1, pp. 90-100, 1988.

[5] M. Ahrenberg, E. Shoifet, K. R. Whitaker, H. Huth, M. D. Ediger and C. Schick, "Differential alternating current chip calorimeter for in situ investigation of vapor-deposited thin films," *Review of Scientific Instruments,* vol. 83, no. 3, 2012.

[6] A. Lazaro, C. Peñalosa, A. Solé, G. Diarce, T. Haussmann, M. Fois, B. Zalba, S. Gshwander and L. F. Cabeza, "Intercomparative tests on phase change materials characterisation with differential scanning calorimeter," *Applied Energy,* vol. 109, pp. 415-420, 2013.

[7] M. W. Freyer and E. A. Lewis, "Isothermal Titration Calorimetry: Experimental Design, Data Analysis, and Probing Macromolecule/Ligand Binding and Kinetic Interactions," *Methods in Cell Biology,* vol. 84, pp. 79-113, 2008.

[8] R. Talhout, A. Villa, A. E. Mark and J. B. F. N. Engberts, "Understanding Binding Affinity: A Combined Isothermal Titration Calorimetry/Molecular Dynamics Study of the Binding of a Series of Hydrophobically Modified Benzamidinium Chloride Inhibitors to Trypsin," *Journal of the American Chemical Society,* vol. 125, no. 35, pp. 10571-10579, 2003.

[9] J. Rouquerol, I. Wadsö, T. J. Lever and P. J. Haines, "Developments in Nomenclature," in *Handbook of Thermal Analysis and Calorimetry*, vol. 5, M. E. Brown and P. K. Gallagher, Eds., Amsterdam, Elsvier, 2008, pp. 13-54.

[10] P. Le Parlouër, "Thermal Analysis and Calorimetry Techniques for Catalytic Investigations," in *Calorimetry and Thermal Methods in Catalysis*, Heidelberg, Springer Berlin, 2013, pp. 51-101.

[11] O. Braissant, D. Wirz, B. Göpfert and A. Daniels, "Biomedical Use of Isothermal Microcalorimeters," *Sensors,* vol. 10, no. 10, pp. 9369-9383, 2010.

[12] J. De Corcuera and R. P. Cavalieri, in *Encyclopedia of agricultural, food, and biological engineering*, Taylor and Francis, 2007, pp. 119-123.

[13] W. Lee, W. Fon, B. W. Axelrod and M. L. Roukes, "High-sensitivity microfluidic calorimeters for biological and chemical applications," *PNAS USA,* vol. 106, no. 36, pp. 15225-15230, 2009.

[14] L. D. Hansen, "Toward a standard nomenclature for calorimetry," *Thermochimica Acta,* vol. 371, no. 1-2, pp. 19-22, 2001.

[15] B. Xie, K. Ramanathan and B. Danielsson, "Principles of Enzyme Thermistor Systems: Applications to Biomedical and Other Measurements," in *Thermal Biosensors, Bioactivity, Bioaffinitty*, Berlin, Springer, 2001, pp. 1-33.

[16] A. Van Herwaarden and P. Sarro, "Thermal sensors based on the seebeck effect," *Sensors and Actuators,* vol. 10, no. 3-4, pp. 321-346, 1986.

[17] C. Hu, "Motion and Recombination of Electrons and Holes," in *Modern Semiconductor Devices for Integrated Circuits*, Prentice Hall, 2010, pp. 35-58.

[18] A. Boyer and E. Cissé, "Properties of thin film thermoelectric materials: application to sensors using the Seebeck effect," *Materials Science and Engineering,* vol. 13, no. 2, pp. 103-111, 1992.

[19] C. J. Glassbrenner and G. A. Slack, "Thermal conductivity of silicon and germanium from 3 K to the melting point," *Physical Review,* vol. 134, no. 4A, pp. 1058-1069, 1964.

[20] T. Yamane, N. Nagai, S.-i. Katayama and M. Todoki, "Measurement of thermal conductivity of silicon dioxide thin films using a 3ω method," *Journal of Applied Physics,* vol. 91, no. 12, pp. 9772-9776, 2002.

[21] X. Zhang and C. P. Grigoropoulos, "Thermal conductivity and diffusivity of free-standing silicon nitride thin films," *Review of Scientific Instruments,* vol. 66, no. 2, pp. 1115-1120, 1995.

[22] C. Mattsson, G. Thungström, K. Bertilsson, H.-E. Nilsson and H. Martin, "Development of an infrared thermopile detector with a thin self-supporting SU-8 membrane," in *IEEE Sensors*, New York, 2007.

[23] E. W. Lemmon and R. T. Jacobsen, "Viscosity and Thermal Conductivity Equations for Nitrogen, Oxygen, Argon, and Air," *International Journal of Thermophysics,* vol. 25, no. 1, pp. 21-69, 2004.

[24] H. Lorenz, M. Despont, N. Fahrni, J. Brugger, P. Vettiger and P. Renaud, "High-aspect-ratio, ultrathick, negative-tone near-UV photoresist and its applications for MEMS," *Sensors and Actuators A: Physical,* vol. 64, no. 1, pp. 33-39, 1998.

[25] L.-E. Briggner and I. Wadsö, "Test and calibration processes for microcalorimeters, with special reference to heat conduction instruments used with aqueous systems," *Journal of Biochemical and Biophysical Methods,* vol. 22, no. 2, pp. 101-118, 1991.

[26] Y. Zhang and S. Tadigadapa, "Calorimetric biosensors with integrated microfluidic channels," *Biosensors and Bioelectronics,* vol. 19, no. 12, pp. 1733-1743, 2004.

[27] Y. Zhang and S. Tadigadapa, "Thermal characterization of liquids and polymer thin films using a microcalorimeter," *Applied Physics Letters,* vol. 86, no. 3, p. 034101, 2005.

[28] K. Verhaegen, K. Baert, J. Simaels and W. Van Driessche, "A high-throughput silicon microphysiometer," *Sensors and Actuators A: Physical,* vol. 82, no. 1-3, pp. 186-190, 2000.

[29] E. A. Johannessen, J. M. R. Weaver, L. Bourova, P. Svobada, P. H. Cobbold and J. M. Cooper, "Micromachined nanocalorimetric sensor for ultra-low-volume cell-based assay," *Analytical Chemistry,* vol. 74, no. 9, pp. 2190-2197, 2002.

[30] F. E. Torres, P. Kuhn, D. De Bruyker, A. G. Bell, M. V. Wolkin, E. Peeters, J. R. Williamson, G. B. Anderson, G. P. Schmitz, M. I. Recht, S. Schweizer, L. G. Scott, J. H. Ho, S. A. Elrod, P. G. Schultz, R. A. Lerner and R. H. Bruce, "Enthalpy Arrays," *Proceedings of the National Academy of Sciences of the United States of America,* vol. 101, no. 26, pp. 9517-9522, 2004.

[31] M. I. Recht, D. De Bruyker, A. G. Bell, M. V. Wolkin, E. Peeters, G. B. Anderson, A. R. Kolatkar, M. W. Bern, P. Kuhn, R. H. Bruce and F. E. Torres, "Enthalpy array analysis of enzymatic and binding reactions," *Analytical Biochemistry,* vol. 377, no. 1, pp. 33-39, 2008.

[32] L. Wang, D. M. Sipe, Y. Xu and Q. Lin, "A MEMS thermal biosensor for metabolic monitoring applications," *Journal of Microelectromechanical Systems,* vol. 17, no. 2, pp. 318-327, 2008.

[33] L. Wang, B. Wang and Q. Lin, "Demonstration of MEMS-based differential scanning calorimetry for determining thermodynamic properties of biomolecules," *Sensors and Actuators B: Chemical,* vol. 134, no. 2, pp. 953-958, 2008.

[34] B. Wang, Y. Jia and Q. Lin, "A microfabrication-based approach to quantitative istothermal titration calorimetry," *Biosensors and Bioelectronics,* vol. 78, pp. 438-446, 2016.

[35] J. Koh, W. Lee and J. H. Shin, "HIgh-sensitivity chip calorimeter platform for sub-nano watt thermal measurement," *Sensors and Actuators A: Physical,* vol. 241, pp. 60-65, 2016.

[36] B. Davaji, H. Jeong Bak, W.-J. Chang and C. Hoon Lee, "A novel on-chip three-dimensional micromachined calorimeter with fully enclosed and suspended thin-film chamber for thermal characterization of liquid samples," *Biomicrofluidics,* vol. 8, no. 3, 2014.

[37] S. Wang, S. Yu, M. S. Siedler, P. M. Ihnat, D. I. Filoti, M. Lu and L. Zuo, "Micro-differential scanning calorimeter for biological samples," *Review of Scientific Instruments,* vol. 87, no. 10, 2016.

[38] S. Wang, S. Yu, M. Siedler, P. M. Ihnat, D. I. Filoti, M. Lu and L. Zuo, "A power compensated differential scanning calorimeter for protein stability characterization," *Sensors and Actuators B: Chemical,* vol. 256, pp. 946-952, 2018.

[39] S. Yu, Y. Wu, S. Wang, M. Lu and L. Zuo, "Thermodynamic analysis of a MEMS based differential scanning calorimeter model," *Sensors and Actuators B: Physical,* vol. 291, pp. 150-155, 2019.

[40] J. Lerchner, A. Wolf, H. J. Schneider, F. Mertens, E. Kessler, V. Baier, A. Funfak, M. Nietzsch and M. Krügel, "Nano-calorimetry of small-sized biological samples," *Thermochimica Acta,* vol. 477, no. 1-2, pp. 48-53, 2008.

[41] T. Maskow, J. Lerchner, M. Peitzsch, H. Harms and G. Wolf, "Chip calorimetry for the monitoring of whole cell biotransformation," *Journal of Biotechnology,* vol. 122, no. 4, pp. 431-442, 2006.

[42] V. Baier, R. Födisch, A. Ihring, E. Kessler, J. Lerchner, G. Wolf, J. M. Köhler, M. Nietzsch and M. Krügel, "Highly sensitive thermopile heat power sensor for micro-fluid calorimetry of biochemical processes," *Sensors and Actuators A: Physical,* Vols. 213-124, pp. 354-359, 2005.

[43] L. M. Ahmad, B. Towe, A. Wolf, F. Mertens and J. Lerchner, "Binding events measurement using a chip calorimeter coupled to magnetic beads," *Sensors and Actuators B: Chemical,* vol. 145, no. 1, pp. 239-245, 2010.

[44] J. Lerchner, T. Maskow and G. Wolf, "Chip calorimetry and its use for biochemical and cell biological investigations," *Chemical Engineering and Processing: Process Intensification,* vol. 47, no. 6, pp. 991-999, 2008.

[45] F. Buchholz, J. Lerchner, F. Mariana, U. Kuhlicke, T. R. Neu, H. Harms and T. Maskow, "Chip-calorimetry provides real time insights into the inactivation of biofilms by predatory bacteria," *Biofouling,* vol. 28, no. 3, pp. 351-362, 2012.

[46] F. Mariana, F. Buchholz, J. Lerchner, T. R. Neu, H. Harms and T. Maskow, "Chip-calorimetric monitoring of biofilm eradication with antibiotics provides mechanistic information," *International Journal of Medical Microbiology,* vol. 303, no. 3, pp. 158-165, 2013.

[47] T. Hartmann, N. Barros, A. Wolf, C. Siewert, P. L. O. Volpe, J. Schemberg, A. Grodrian, E. Kessler, F. Hänschke, F. Mertens and J. Lerchner, "Thermopile chip based calorimeter for the study of aggregated biological samples in segmented flow," *Sensors and Actuators B: Chemical,* vol. 201, pp. 460-468, 2014.

[48] A. Wolf, T. Hartmann, M. Bertolini, J. Schemberg, A. Grodrian, K. Lemke, T. Förster, E. Kessler, F. Hänschke, F. Mertens, R. Paus and J. Lerchner, "Toward high-throughput chip calorimetry by use of segmented-flow technology," *Thermochimica Acta,* vol. 603, pp. 172-183, 2015.

[49] J. Lerchner, P. L. O. Volpe, C. Lanaro, K. Y. Fertrin, F. F. Costa, D. M. Albuquerque, F. Hänschke and F. Mertens, "A chip calorimetry-based method for the real-time investigation of metabolic activity changes in human erythrocytes caused by cell sickling," *Journal of Thermal Analysis and Calorimetry,* vol. 136, pp. 771-781, 2019.

[50] R. Splinter, A. W. van Herwaarden, I. A. van Wetten, A. Pfreundt and W. E. Svendsen, "Fast differential scanning calorimetry of liquid samples with chips," *Thermochimica Acta,* vol. 603, pp. 162-171, 2015.

[51] R. Splinter, A. W. van Herwaarden, S. Pastorekova, T. C. Linders, T. Korse and D. van den Broek, "Measuring human blood serum with chip based fast liquid differential scanning calorimetry," *Thermochimica Acta,* vol. 693, pp. 76-83, 2016.

[52] N. Inomata, L. Pan, Z. Wang, M. Kimura and T. Ono, "Vanadium oxide thermal microsensor integrated in a microfluidic chup for detecting cholesterol and glucose concentrations," *Microsystem Technologies,* vol. 23, pp. 2873-2879, 2017.

[53] Z. Wang, M. Kimura and T. Ono, "Manufacturing and characterization of simple cantilever thermal biosensor with Si-metal thermocouple structure for enzymatic reaction detection," *Thermochimica Acta,* vol. 668, pp. 110-115, 2018.

[54] N. Inomata, M. Toda and T. Ono, "Microfabricated temperature-sensing devices using a microfluidic chip for biological applications," *International Journal of Automation Technologies,* vol. 12, no. 1, pp. 15-23, 2018.

[55] Z. Wang, L. Jinlong, Z. An, M. Kimura and T. Ono, "Enzyme immobilization in completely packaged freestanding SU-8 microfluidic channel by electro click chemistry for compact thermal biosensor," *Process Biochemistry,* vol. 79, pp. 57-64, 2019.

[56] Z. Wang, M. Kimura, M. Toda and T. Ono, "Silicon-based micro calorimeter with single thermocouple structure for thermal characterization," *IEEE Electron Device Letters,* vol. 40, no. 7, pp. 1198-1200, 2019.

[57] J. Xu, R. Reiserer, J. Tellinghuisen, J. P. Wikswo and F. J. Baudenbacher, "A Microfabricated Nanocalorimeter: Design, Characterization, and Chemical Calibration," *Analytical Chemistry,* vol. 80, no. 8, pp. 2728-2733, 2008.

[58] B. Lubbers and F. Baudenbacher, "Isothermal Titration Calorimetry in Nanoliter Droplets with Sub-Second Time Constants," *Analytical Chemistry,* vol. 83, no. 20, p. 7955, 2011.

[59] B. Lubbers, Nano-Calorimetry for Point of Care Diagnostics, Nashville, TN: PhD Thesis, Vanderbilt University, 2015.

[60] B. Lubbers, E. Kazura, E. Dawson, R. Mernaugh and F. Baudenbacher, "Microfabricated calorimeters for thermometric enzyme linked immunosorbent assay in one-Nanoliter droplets," *Biomedical Microdevices,* vol. 21, no. 4, p. 85, 2019.

[61] E. Kazura, B. R. Lubbers, E. Dawson, J. A. Phillips and F. Baudenbacher, "Nano-Calorimetry based point of care biosensor for metabolic disease management," *Biomedical Microdevices,* vol. 19, no. 3, p. 50, 2017.

[62] S. Wang, X. Sha, S. Yu and Y. Zhao, "Nanocalorimeters for biomolecular analysis and cell metabolism monitoring," *Biomicrofluidics,* vol. 14, no. 1, 2020.

[63] Y. H. Desai, T. I. Eldho and A. H. Shah, Finite element method with applications in engineering, New Delhi: Dorling Kindersley, 2011.

[64] O. C. Zienkiewicz, R. L. Taylor and J. Z. Zhu, The finite element method: its basis and fundamentals, Amsterdam: Elsevier Butterworth-Heinemann, 2005.

[65] J. N. Reddy and D. K. Gartling, The Finite Element Method in Heat Transfer and Fluid Dynamics, 3rd ed., Boca Raton: CRC Press, 2010.

[66] C. Lyons and L. C. Clark Jr., "Electrode systems for continuous monitoring in cardiovascular surgery," *Annals of the New York Academy of Sciences,* vol. 102, pp. 29-45, 1962.

[67] C. Chen, Q. Xie, D. Yang, H. Xiao, Y. Fu, Y. Tan and S. Yao, "Recent advances in electrochemical glucose biosensors: a review," *RSC Advances,* vol. 3, no. 14, pp. 4473-4491, 2013.

[68] S. Premjeet, G. Deepika, B. Sudeep, J. Sonam, K. Sahil, R. Devashish and K. Sunil, "Enzyme-Linked Immuno-Sorbent Assay (ELISA), basics and it's application: a comprehensive review," *Journal of Pharmacy Research,* vol. 4, no. 12, pp. 4581-4583, 2011.

[69] A. H. Ng, U. Uddayasankar and A. R. Wheeler, "Immunoassays in microfluidic systems," *Analytical and Bioanalytical Chemistry,* vol. 397, no. 3, pp. 991-1007, 2010.

[70] B. Mattiasson, C. Borrebaeck, B. Sanfridson and K. Mosbach, "Thermometric enzyme linked immunosorbent assay: TELISA," *Biochimica et Biophysica Acta (BBA)-Enzymology,* vol. 483, no. 2, pp. 221-227, 1977.

[71] F. Lammers and T. Scheper, "Thermal Biosensors in Biotechnology," in *Thermal Biosensors, Bioactivity, Bioaffinitty*, Berlin Heidelberg, Springer, 1999, p. 35.

[72] R. Phillips, J. Kondev and J. Theriot, Physical Biology of the Cell, New York: Garland Science, 2010.

[73] M. P. Byfield and R. A. Abuknesha, "Biochemical aspects of biosensors," *Biosensors and Bioelectronics,* vol. 9, no. 4-5, pp. 373-399, 1994.

[74] B. Danielsson, "Calorimetric biosensors," *Journal of Biotechnology,* vol. 15, no. 3, pp. 187-200, 1990.

[75] D. L. Nelson, A. L. Lehninger and M. M. Cox, Lehninger Principles of Biochemistry, New York: W. H. Freeman, 2008.

[76] H. Liu, Z. Wang, Y. Liu, J. Xiao and C. Wang, "Enthalpy change and mechanism of oxidation of o-phenylenediamine by hydrogen peroxide catalyzed by horseradish peroxidase," *Thermochimica Acta,* vol. 443, no. 2, pp. 173-178, 2006.

[77] T. M. Hamilton, A. A. Dobie-Galuska and S. M. Wietstock, "The o-Phenylenediamine-Horseradish Peroxidase System: Enzyme Kinetics in the General Chemistry Laboratory," *Journal of Chemical Education,* vol. 76, no. 5, pp. 642-644, 1999.

[78] E. S. Domalski, "Selected Values of Heats of Combustion and Heats of Formation of Organic Compounds Containing the Elements C, H, N, O, P, and S.," *Journal of Physical and Chemical Reference Data 1,* vol. 1, no. 2, pp. 221-227, 1972.

[79] R. N. Goldberg, Y. B. Tewari and T. N. Bhat, "Thermodynamics of enzyme-catalyzed reactions - a database for quantitative biochemistry," *Bioinformatics,* vol. 20, no. 16, pp. 2874-2877, 2004.

[80] M. Elder, "Point of Care Diagnostics," BCC Research, 2014.

[81] J. Wang, "Electrochemical glucose biosensors," *Chemical Reviews,* vol. 108, no. 2, pp. 814-825, 2008.

[82] L. Ben Mohammadi, T. Klotzbuecher, S. Sigloch, K. Welzel, M. Goeddel, T. R. Pieber and L. Schaupp, "Clinical performance of a low cost near infrared sensor for continuous glucose monitoring applied with subcutaneous microdialysis," *Biomedical Microdevices,* vol. 17, no. 4, 2015.

[83] A. Soni and S. K. Jha, "A paper strip based non-invasive glucose biosensor for salivary analysis," *Biosensors and Bioelectronics,* vol. 67, pp. 763-768, 2015.

[84] B. Danielsson, "The enzyme thermistor," *Applied Biochemistry and Biotechnology,* vol. 7, no. 1, pp. 127-134, 1982.

[85] F. Lammers and T. Scheper, "On-line monitoring of enzyme-catalyzed biotransformations with biosensors," *Enzyme and Microbial Technology,* vol. 20, no. 6, pp. 432-436, 1997.

[86] B. Xie, K. Ramanathan and B. Danielsson, "Principles of Enzyme Thermistor Systems: Applications to Biomedical and Other Measurements," in *Thermal Biosensors, Bioactivity, Bioaffinitty*, Berlin Heidelberg, Springer, 1999, p. 1.

[87] K. Verhaegen, J. Simaels, W. Van Driessche, K. Baert, W. Sansen, B. Puers, L. Hermans and R. Mertens, "A Biomedical Microphysiometer," *Biomedical Microdevices,* vol. 2, no. 2, pp. 93-98, 1999.

[88] B. Davaji and C. H. Lee, "A paper-based calorimetric microfluidics platform for bio-chemical sensing," *Biosensors and Bioelectronics,* vol. 59, pp. 120-126, 2014.

[89] S. V. H. Lai and S. Tadigadapa, "Calorimetric sensing system for real-time urea and creatinine measurements," in *Sensors, 2012 IEEE*, Taipei, 2012.

[90] A. Gámez, L. Wang, M. Straub, M. G. Patch and R. C. Stevens, "Toward PKU Enzyme Replacement Therapy: PEGylation with Activity Retention for Three Forms of Recombinant Phenylalanine Hydroxylase," *Molecular Therapy,* vol. 9, no. 1, pp. 124-129, 2004.

[91] S. A. Banta-Wright and R. D. Steiner, "Tandem Mass Spectrometry in Newborn Screening: A Primer for Neonatal and Perinatal Nurses," *Journal of Perinatal & Neonatal Nursing,* vol. 18, no. 1, pp. 41-60, 2004.

Chapter II: Microfabricated calorimeters for thermometric enzyme-linked immunosorbent assay in one-nanoliter droplets[1]

By

Brad Lubbers, Evan Kazura, Elliott Dawson, Ray Mernaugh, and Franz Baudenbacher

In Chapter II, we describe the design of a differential thermopile calorimeter using standard microfabrication techniques. Two-point material testing determined bismuth (Bi) and titanium (Ti) as the best combination of thermocouple materials maximizing the Seebeck coefficient in combination with in-house ease of deposition and patterning. Constructing the thermopile calorimeter on a thin Su-8 membrane led to a more thermally isolated reaction volume while producing a more rugged reusable platform than the standard silicon nitride membranes. Designing and fabricating our own platform allows for customization, including adding on-chip fluid handling. The material selection, in combination with geometrical optimization, allowed us to fabricate a calorimeter much more sensitive than commercially available ones. A sandwich thermometric enzyme-linked immunosorbent assay (TELISA) to quantify trastuzumab in human serum achieved sensitivity to therapeutic levels, showing the viability of micromachined calorimeters to compete as biosensors.

Abstract

Advances in microfabrication allow for highly sensitive calorimeters with dramatically reduced volume, decreased response time and increased energy resolution. These calorimeters hold the

[1] Reproduced with permission from Lubbers, B. R., Kazura, E., Dawson, E., Mernaugh, R., & Baudenbacher, F. (2019). Microfabricated calorimeters for thermometric enzyme-linked immunosorbent assay in one-nanoliter droplets. Biomedical Microdevices, 21(85).

potential for designs of ELISA platforms competitive with fluorescent and chemiluminescent technologies. We have developed a new assay platform using conventional ELISA reagents to produce a thermal signal quantifiable using calorimetry. Our optimized micromachined calorimeters have nL reaction volumes and a minimum detectable power of 375 pW/Hz$^{1/2}$. We demonstrate rapid quantification in a model system of trastuzumab, a humanized monoclonal antibody used in the treatment of HER2 overexpressing breast cancers, in human serum using a HER2 peptide mimetic. Trastuzumab concentration and reaction time constant correlated well (R^2=0.954) and can be used to determine trastuzumab concentrations. The limit of detection for the ThermometricELISA (TELISA) was 10 µg/ml trastuzumab in human serum. TELISA allows for a simple readout, reduction in assay time, sample and reagent volumes and has the potential to become a point-of-care multiplexed platform technology.

Introduction

Therapeutic monoclonal antibodies (mAbs) are of particular interest as an emerging alternative to small-molecule drugs for the treatment of conditions such as cancer, infections, cardiovascular disease, and immune disorders [1] [2]. The first mAb approved for solid tumor cancer treatment, trastuzumab (Herceptin®, Genentech USA), is a humanized IgG1κ useful against HER2 positive breast cancers [3]. However, in some patients, cellular Fc receptors responsible for binding to and recycling trastuzumab are atypical; and as such, trastuzumab is cleared quicker from the body resulting in reduced therapeutic efficacy [4]. In order to improve patient outcome and limit high cost treatment courses, serum titer measurements can be used to determine patient trastuzumab clearance rates and appropriate dosages for efficient treatment. The most abundant class/subclass of antibody present in human serum is IgG1 and normally ranges in concentration from 9-12 mg/ml of serum [5]. Trastuzumab is a genetically engineered humanized IgG1 kappa light chain mAb, however since it incorporates human IgG1 constant domains it is difficult to distinguish from normal human antibodies [6]. To overcome this,

Jiang et. al. used phage display to select for the HER2 peptide mimotope (designated Ch-19, sequence: CGSGSGSQLGPYELWELSH) that trastuzumab binds [7]. Another phage displayed recombinant antibody (2B4 scFv) has been successfully immobilized onto a gold sensor surface for use in a piezoimmunosensor (i.e. quartz crystal microbalance) assay to capture and detect trastuzumab present in solution [8].

Enzyme linked immunosorbent assays (ELISAs) have become the gold standard for measuring antibodies and antigens, both native and introduced, in biological samples [9] since the 1970s. Of the many commercially available microtiter-based ELISA kits, most utilize an enzyme linked to a detecting antibody to produce a colorimetric, chemiluminescent, or fluorescent signal that can be quantified using a microtiter plate reader. The need to increase sensitivity and reduce sample consumption and assay time drives research toward a rapid, low-volume, direct readout ELISA system [10].

The most frequent substrate in ELISA is hydrogen peroxide, which is catalytically reduced by horseradish peroxidase (HRP, EC 1.11.1.7). The reaction enthalpy associated with the decomposition of H_2O_2 is large (-98 kJ/mol) making it an attractive target for calorimetric determination. Mattiasson et al was the first to create an ELISA system with a calorimetric readout, termed Thermometric Enzyme Linked Immunosorbent Assay (TELISA). The original TELISA system was based on inhibition binding of a catalase linked albumin to an antibody coated calorimetry column [11]. These flow through systems required a large sample volume (>0.5 ml) and the use of temperature controlled thermistor columns, but sensitivity to the µg/ml level for insulin, human IgG, and albumin were achieved [12]. However, in the years following, fluorescent and chemiluminescent ELISA systems achieved much higher sensitivity, so TELISA has seen little use in the past decade.

Advances in microfabrication allow for highly sensitive calorimeters with dramatically reduced volume, which decreases response time and increases energy resolution. These calorimeters hold the potential for designs of TELISA systems competitive with fluorescent and chemiluminescent ELISAs.

Previous calorimeters based on off-the-shelf thin film IR sensors showed a minimum energy resolution of 1.5 nW/Hz$^{1/2}$ and suffered from evaporative droplet loss [13]. The Zuo group used a polyimide film and PDMS chamber to minimize heat conduction and sample evaporation in a vanadium oxide thermistor-based calorimeter, but suffer from time constants of several seconds [14]. Other micro-calorimeter designs utilize a Si based membrane or quasi 2-D microfluidic flow channels that decrease heat flow and result in minimum power sensitivity of several nanowatts [15][16][17][18]. Previous micro-calorimeter designs have utilized materials like gold and nickel that are easy to fabricate and have low resistance, but lack the high Seebeck coefficient needed for high sensitivity [17][19]. Therefore, new calorimeters were designed to incorporate high Seebeck coefficient materials in the thermopile, a low thermal conductivity polymer membrane, better vapor sealing, and optimized geometries.

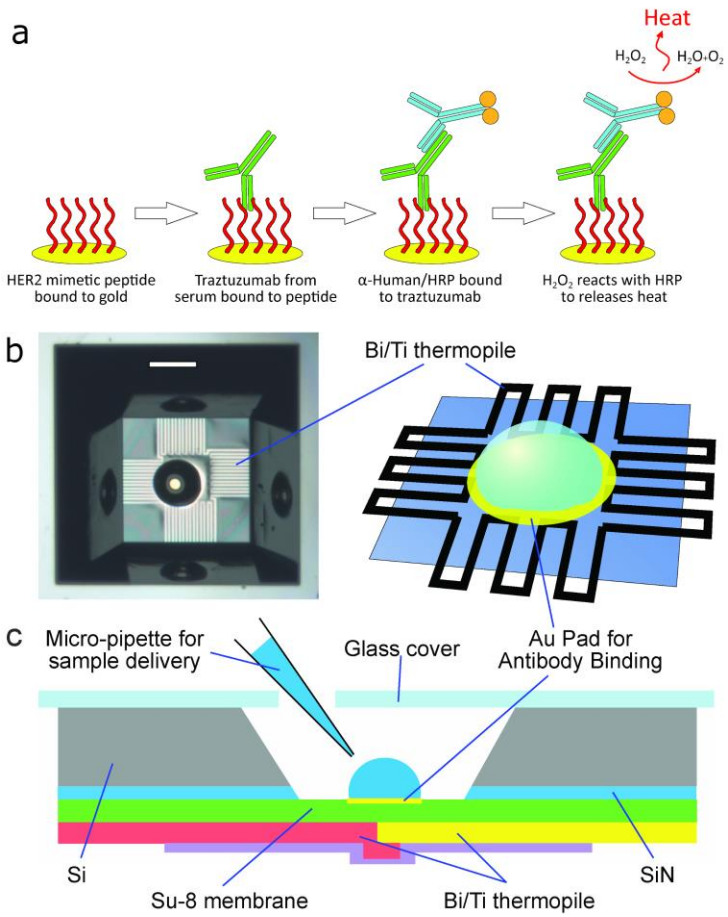

Fig 1. TELISA steps. (a) The binding steps of the TELISA follow that of a traditional sandwich ELISA. However, in the detection step, the heat from the reaction of H_2O_2 and OPD with HRP is quantified, rather than a chromogenic or fluorescent measurement. All steps can be carried out in a 1-nanoliter volume, greatly reducing reagent and sample consumption. (b) A 1 nl sample drop sits atop a suspended Su-8 membrane on which a 28 Bi/Ti thermopile junction has been patterned. The Su-8 membrane and gold pad are used to immobilize the HER2 peptide mimetic, confine the sample droplet, and carry out the reaction for trastuzumab detection. Scale bar 200 µm. (c) The sample drop sits in an anisotropically etched Si pit and is accessed through a hole in the cover via a glass micropipette.

Here, we report utilization of a micromachined calorimeter for a sandwich based thermal ELISA with nanoliter sample volumes. Fig. 1a shows the ELISA construct, antibody binding steps, and the thermal readout step with HRP. Since a known amount of energy is released when a finite substrate supply is consumed, the area under the curve is preserved. The time course then indicates the amount of enzyme present. Furthermore, reduction of the sample volume maximizes the surface area to volume ratio to increase assay sensitivity. By operating in a 1nl reaction volume, antibody and sample consumption is also greatly diminished. This has the added benefit of minimizing antibody binding time by reducing diffusion distance, such that a multi-step sandwich ELISA can be performed in less than 5 minutes [20]. This allows for the potential of pinprick point-of-care measurements that incorporate on-chip microfluidics to automate sample handling. Since many commercial ELISA systems already rely on a peroxidase/peroxide reporter system, many off-the-shelf kits can be converted for use in TELISA. Significant advantages of the TELISA over traditional ELISAs are a reduction in assay times, conservation of sample volume, and direct readout.

Materials and Methods

Device Design

Since the energies involved in the enzymatic reactions of ELISA in nanoliter volumes can be quite small (< 100 nJ) and over a time period greater than 100 seconds, a highly sensitive calorimeter capable of sub-nanowatt resolution is needed. In order to maximize sensitivity, our microcalorimeter features a small working volume, low thermal conductivity membrane, and materials with a high absolute Seebeck coefficient (Fig. 1b-c). The ideal calorimeter would have a very wide membrane on which the reaction droplet and thermopile sit to minimize thermal conduction away from the droplet. However, this creates long thermopile tracks with high electrical resistance. This leads to an increase in Johnson noise, the limiting factor in minimum detectable power. Since the resistance and thermoelectric properties of

thin film metals can vary greatly from the bulk properties [21], we performed four point sheet resistance and thermoelectric measurement of various metals to find those most suitable for our calorimeter. Material pairs were evaluated on experimentally found Seebeck coefficient (S) and electrical resistivity (ρ), as well as literature thermal conductivity (κ) in a figure of merit Z*.

$$Z^* = \frac{S}{0.25\kappa + \sqrt{\rho}}$$

Results for metal pairs we had the capability to deposit and pattern are shown in Table 1. A full description of material properties and the process can be found in Lubbers 2015. Bismuth and antimony provided the best combination of high conductivity and high absolute Seebeck coefficient, but proved difficult to pattern in thin traces together. Bi/chromium and Bi/nichrome both form a rough surface with high resistance when deposited over Su-8. Therefore, bismuth and titanium proved to be the best combination of Z* and ease of patterning.

Table 1. Figure of merit for potential thermopile materials [22].

	Z*	thin film Z*
Bi/Sb	3.446	2.517
Ni/Au	0.337	0.288
Ni/Ti	0.900	0.644
Ni/Cr	1.097	0.680
Bi/Ti	**2.447**	**1.682**
Bi/Cr	2.288	1.516
Bi/NiCr	2.421	1.754

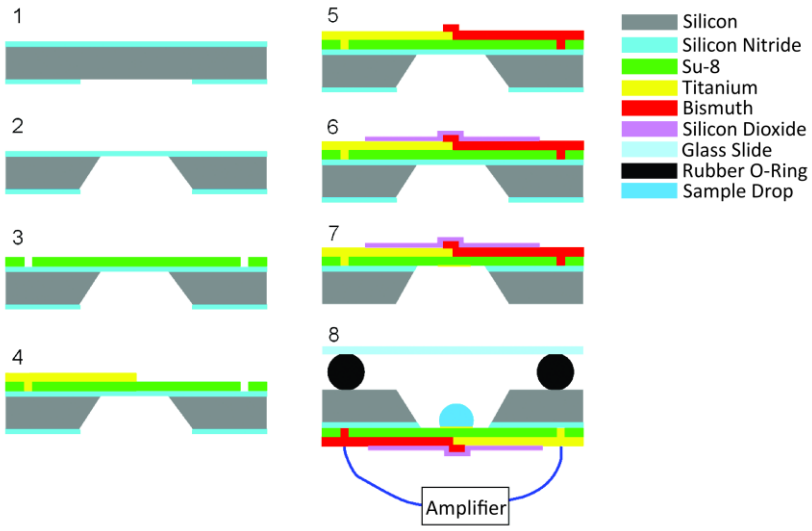

Fig 2**.** Microcalorimeter microfabrication steps. (1-2) Anisotropically etched pit is formed in the silicon substrate, revealing a sacrificial silicon nitride membrane. (3) Su-8 polymer membrane is applied. (4-5) Bismuth and titanium thermopile tracks are deposited and patterned. (6) Silicon dioxide passivation layer is applied. (7) The remaining silicon nitrite under the membrane is removed and the gold binding spot applied. (8) The finished device is paired with a glass lid and o-ring to prevent sample evaporation and attached to a low noise amplifier during measurements.

A COMSOL Multiphysics/ MATLAB model was built based on previous calorimeter designs [13]. Variables were introduced to change the sensing area and membrane size while maximizing sensitivity and minimizing thermopile resistance. An iterative approach showed for a 1 nl drop, the optimal calorimeter had a membrane width of 525 µm and a sensing area width of 200 µm with 28 junctions. 1 nl was chosen as the optimal drop size as previous work had shown that as drop volume decreases, sensitivity increases, but must be balanced with sample evaporation to allow sufficient measurement time [13]. Variables for thermopile thickness were also introduced and it was found that a Ti thickness of 200 nm and a Bi thickness of 400 nm provided the best balance of thermal and electrical conductivity.

Device Fabrication

All micromachining was performed in the cleanrooms at Vanderbilt University. 75 mm diameter silicon wafers, <100> orientation, double side polished, with 500 nm low stress silicon nitride (SiN) coated on both sides were obtained from WRS Materials (San Jose, CA). Chrome on soda-lime photomasks were produced by Advance Reproductions Corp. (North Andover, MA). Photoresist and

developer were procured from MicroChem Corp. (Westborough, MA). All other chemical were from Fisher Scientific (Pittsburgh, PA). The microfabrication steps are displayed in Fig. 2. Pits are etched anisotropically in the silicon substrate, revealing a sacrificial silicon nitride membrane. An Su-8 polymer membrane is applied to the untouched side of the wafer, forming a base on which to construct the microcalorimeter. Titanium and bismuth thermopile tracks are deposited by e-beam thermal deposition and patterned by hydrofluoric acid chemical etch and ion milling, respectively. Silicon dioxide passivation layer is applied for electrical isolation of the thermopiles. Reactive ion etching removes the remaining silicon nitrite under the membrane, freeing the thermally-isolated sensing areas of the microcalorimeters. Finally, gold contact pads are deposited by e-beam thermal evaporation through a shadow mask.

Device Operation

Reaction chamber was formed by securing a rubber o-ring to the chip surface around the microcalorimeter sensing area. Device was attached to a custom, low-noise, DC chopper amplifier. The reaction chamber was then sealed with mineral oil and a glass slide. Liquid samples were delivered via an air driven Picospritzer II (Parker Hannifin, Cleveland, OH) using a glass micropipette positioned by a micromanipulator (MP-285, Sutter Instrument Co, Novato, CA). Access to the device was achieved through a hole drilled in glass slide and sealed with mineral oil to prevent sample evaporation. As reaction occurred on the calorimeter, voltage from thermopiles was recorded in LabView over time. Once reaction reached equilibrium, recording was stopped. Microcalorimeter devices can be reused by rinsing the sample well with toluene to remove any manufacturing residue or protein left from previous tests.

Materials

In this study, we used Ch-19M (BioVentures, Murfreesboro, TN), a modified version that includes a biotin linker and an improved sequence to minimize serum matrix effects. Negative controls were carried out using another HER2 mimotope peptide, PINC (PINCTHSCVDLDDKGCPAEQRASPLTSIISK-Ahx-biotin, United Biosystems), in place of Ch-19M, and using Avastin® from Genentech USA (i.e. Bevacizumab: a humanized IgG1 kappa light chain mAb specific for vascular endothelial growth factor) in lieu of trastuzumab. Pooled human serum (H4522) and peroxidase conjugated, goat anti-human IgG (Fc-specific) antibody (#A0170) were obtained from Sigma Aldrich.

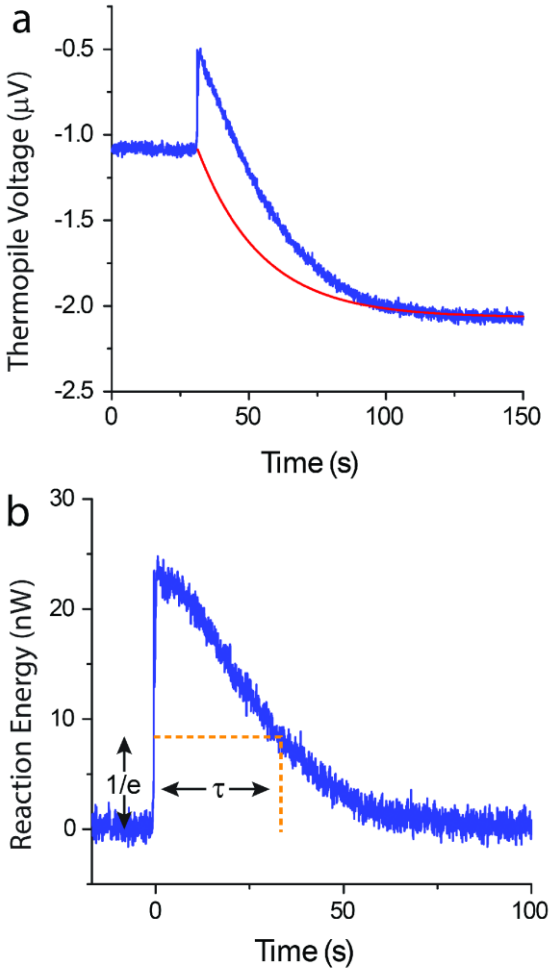

Fig 3. Baseline correction and τ calculation (a) Uncorrected thermopile output voltage from TELISA detection of 50 µg/ml trastuzumab in human serum. The negative offset after peroxide injection is due to changes in the evaporation rate of the sample droplet. An exponential (red line) is fit to the curve so that the offset can be removed. (b) After the offset is removed, voltage can be converted to heat energy based on calorimeter sensitivity (45 V/W). The 1/e decay time (τ) of the signal is used to determine trastuzumab concentration.

Surface Functionalization

A thermally deposited gold spot on the topside of the calorimeter membrane allowed for attachment of the Ch-19M peptide and subsequent trastuzumab binding. Streptavidin was passively adsorbed to the Au surface by incubating streptavidin diluted in PBS (20 µg/ml) on the Au surface for 30 minutes at room temperature in a humidified petri dish [23]. The sensor surface was rinsed and blocked for 15 seconds with PBS containing 0.2% Tween 20 (PBS-T). The biotinylated HER2 peptide mimetic Ch-19M was diluted to 3 µM in PBS-T and coupled to

the adsorbed streptavidin by incubating for 20 minutes at room temperature. The sensor was again rinsed with PBS-T.

Detection of Trastuzumab

Pooled human serum with varying concentrations of trastuzumab (0-100 μg/ml) was diluted 1:4 in PBS-T and allowed to bind for 20 minutes to Ch-19M on the gold sensor surface. After a PBS-T wash, a peroxidase conjugated, goat anti-human IgG (Fc-specific) antibody (diluted 1:250 in PBS-T) was applied to the sensor surface for 20 minutes at room temperature to bind the available trastuzumab. Unbound peroxidase conjugated anti-human IgG antibody was rinsed from the surface with PBS-T and the sensor surface dried with N_2. The reaction chamber was sealed with a glass cover slide and mineral oil to provide a vapor tight seal that allowed the reaction droplet to persist for up to an hour, although most reactions were completed in less than 5 minutes. 1 nl of PBS was dispensed onto the center of the sensor. After thermal equilibrium was reached, 100 pl of hydrogen peroxide (50 mM - acting as an electron acceptor) and o-phenylenediamine dihydrochloride (OPD) (100 mM - acting as an electron donor) in PBS was injected into the drop to generate a thermal signal. The resulting thermal output from the reaction of H_2O_2 with the bound peroxidase was recorded in LabView until temperature equilibrium was achieved and the time constant was then calculated in MATLAB. Previous data shows that repeated injections of water into the base drop resulted in a signal baseline drop that scaled with the change in surface area of the drop. Therefore the baseline shift after injection was due to predictable changes in the evaporation rate post-injection and can be removed by fitting the raw signal to an exponential equation (Fig. 3a). The heat integral and time constant (τ) of the temperature decay were then computed from the corrected time trace (Fig. 3b). Since the energy released was constant with regards to H_2O_2 concentration, the time needed to consume the substrate was predicted to be dependent upon the concentration and enzyme-kinetics of the peroxidase indirectly coupled to trastuzumab captured on

the calorimeter sensor surface. A calibration curve was constructed to allow the calculation of trastuzumab concentration based on the thermal time constant.

Results and Discussion

Calorimeter Characterization

Heat flow and electrical modeling in COMSOL Multiphysics showed the optimal configuration to be a 28-junction Bi/Ti thermopile with a 525 µm wide Su-8 polymer membrane and a 200 µm wide hot-junction sensing area (Fig. 4a). The core technology of the TELISA system is a microfabricated polymer membrane based microcalorimeter. Standard microfabrication techniques were used to construct the thin film calorimeters on Si substrates with a high device yield of >85%. Devices showed no degradation in performance over time (6 months) with repeated use, provided the membrane was not ruptured. With a 1 nl sample volume, acid-base and laser calibration (Fig. 5) of the calorimeters showed a minimum detectable power of 375 pW/Hz$^{1/2}$, a power sensitivity of 45 V/W, and a time constant of 95 ms, all in line with the model predictions (Fig. 4b). This allows for the detection of as little as 4 femtomoles of hydrogen peroxide, or the energy output of 6 attomoles of typical HRP.

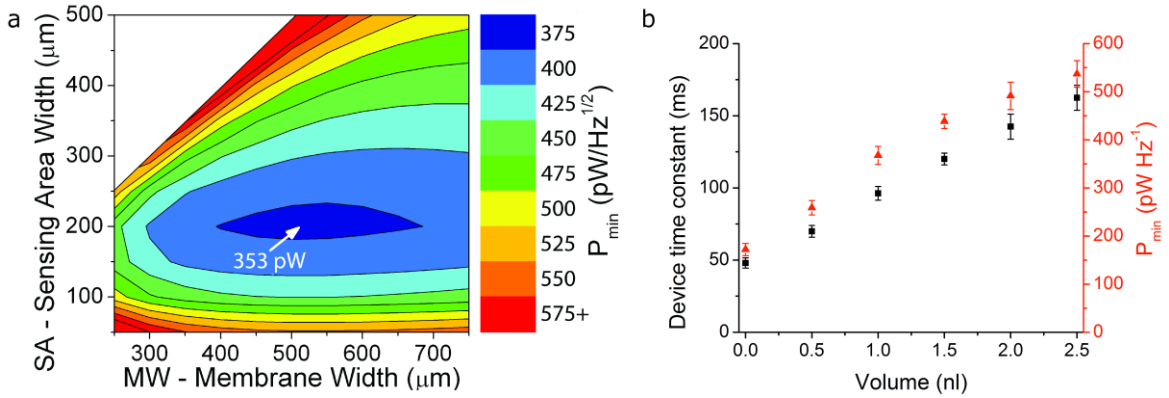

Fig 4. (a) Calorimeter optimization. Heat flow and electrical modeling in COMSOL and MATLAB were used to determine the optimal dimensions of the calorimeter during the design phase. By balancing thermopile track length, thickness, and membrane size a P_{min} of 353 pW/Hz$^{1/2}$ was predicted. Actual measurements on the constructed calorimeters showed a P_{min} of 375 pW/Hz$^{1/2}$. (b) The microcalorimeter devices have enhances performance at smaller sample volumes. 1nl was chosen as the optimal volume to balance performance and droplet evaporation. The combination of sub-100 ms time constant and minimum detectable power (P_{min}) of 375 nW/√Hz at 1 nl, allows for high resolution measurement of TELISA heat signatures.

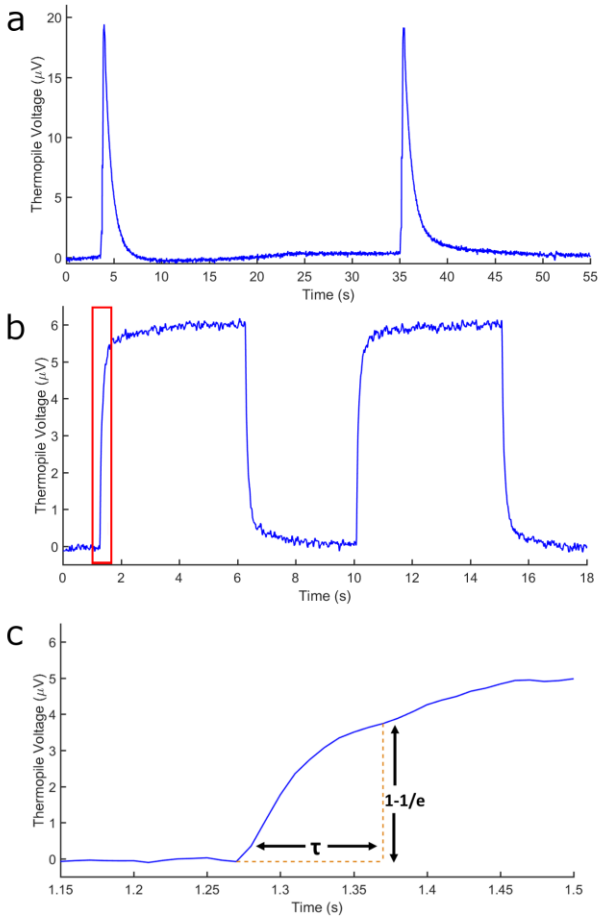

Fig 5. Calorimeter characterization (a) Calorimeter sensitivity calculation. 100 pl of 50 mM HCl was injected into a 1 nl drop of 50 mM NaOH. After baseline drift was corrected and heat of injection removed, the area under the curve was divided by the heat of reaction for each injection (280 nJ) to find device sensitivity. (b) The microcalorimeter time constant was measured using a 650 nm laser focused on a 1 nl water drop centered on the sensing area. The laser was pulsed at 0.2 Hz. (c) Zoomed view of calorimeter response (red box in b). The 1-1/e rise time of the signal was used to determine the sensor time constant.

Quantification of Trastuzumab

In the trastuzumab TELISA, it was found that the peroxide reaction time constant (τ) could be varied by changing H_2O_2 concentration, with a shorter τ being obtained at lower concentrations. However, this resulted in a reduced assay signal and an increase in assay background noise. It was determined that a 10 mM concentration of H_2O_2 provided a balance between assay time and signal strength for use in the present application. Trastuzumab concentration and τ correlated well (R^2=0.954) and that τ could be used to accurately determine trastuzumab concentration in serum to 50 µg/ml (Fig. 6). The limit of detection above baseline noise for the TELISA was 10 µg/ml trastuzumab in human serum. Therapeutic serum concentrations of trastuzumab are between 50 to 100 µg/ml, meaning our assay achieves detection and approaches quantification at clinically-relevant levels [24].

Normal human serum contains a high concentration (~9-12 mg/ml serum) of IgG1 antibodies. Normal human serum IgG1 and the negative control humanized therapeutic antibody bevacizumab did not bind to Ch-19M in the TELISA (Fig. 6). Additionally, trastuzumab in diluted human serum did not bind

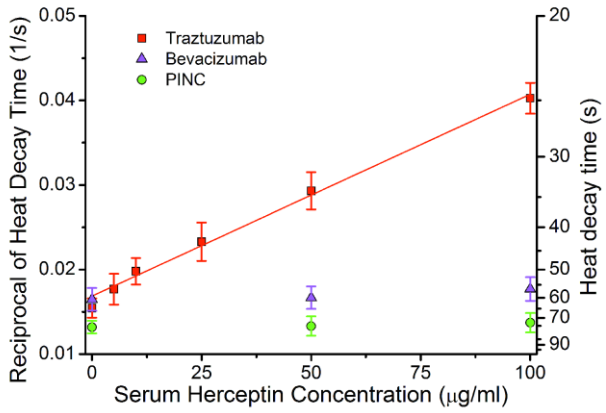

Fig 6. Trastuzumab dose response. As trastuzumab concentration increases, peroxide is consumed faster; leading to a shorter heat decay time. Negative controls with bevacizumab and PINC show no sensitivity to trastuzumab. The therapeutic dosage of trastuzumab (10-100 μg/ml serum concentration) is well covered by TELISA quantification and is highly correlated to τ (R^2=0.954). Means ± s.d. are shown (n = 4 per point).

to the negative control PINC peptide when used in lieu of Ch-19M. The PINC peptide is another HER2 mimotope, however trastuzumab is known not to bind to it. These results suggest that trastuzumab could be specifically detected in 1 nl of diluted human serum, and that the assay exhibited high sensitivity.

Components (e.g. proteins, lipids, etc.) present in human serum can interfere with antigen (e.g. Ch-19M) and antibody (e.g. trastuzumab) interactions. These interferences are referred to as serum matrix effects and lead to nonspecific binding. Some serum matrix effects were seen with the TELISA, as signal amplitude was reduced with trastuzumab diluted in human serum rather than PBS buffer (Fig. 7). However, the sensitivity remains constant as demonstrated by the dose response curve (Fig. 6). It will be important to carry out future studies to identify the origin of these serum matrix effects to improve sensitivity.

Conclusions

TELISA does not rely on specific reagents and can be widely adapted to a broad spectrum of immunoassays using existing reagents. The thermal signature is quantified using micromachined microcalorimeters with

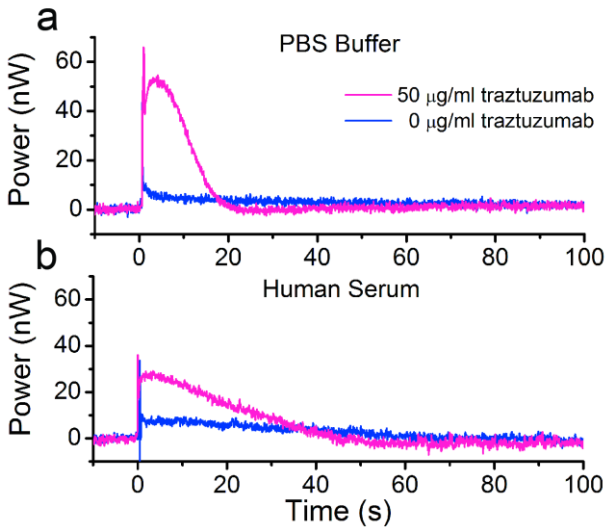

Fig 7. TELISA signal in PBS and serum (a) A strong signal is produced during the detection of 50 μg/ml trastuzumab in PBS. (b) Trastuzumab suspended in human serum shows a lower binding efficiency and a slightly higher background signal - presumably due to serum matrix effects.

nanoliter sized reaction volumes, sub-nanojoule sensitives, and sub-second time constants. The technology lends itself to a point-of-care device for high throughput multiplexed assay based on a finger prick. We are currently working on label free point-of-care systems based on the thermal detection of direct binding events and analyte reactions.

Acknowledgements

This work was supported by funding from Vanderbilt University.

References

[1] C. Piggee, "In vivo molecular imaging by LAESI MS," Analytical Chemistry, vol. 80, no. 13, p. 4783, 2008.

[2] E. V. Dolgova, E. A. Alyamkina, Y. R. Efremov, V. P. Nikolin, N. A. Popova, T. V. Tyrinova, A. V. Kozel, A. M. Minkevich, O. M. Andrushkevich, E. L. Zavyalov, A. V. Romaschenko, S. I. Bayborodin, O. S. Taranov, V. V. Omigov, E. Y. Shevela, V. V. Stupak, S. V. Mishinov, V. A. Rogachev, A. S. Proskurina, V. I. Mayorov, M. A. Shurdov, A. A. Ostanin, E. R. Chernykh and S. S. Bogachev, "Identification of cancer stem cells and a strategy for their elimination," Cancer Biology and Therapy, vol. 15, no. 10, pp. 1378-1394, 2014.

[3] F. J. Esteva, V. Valero, D. Booser, L. T. Guerra, J. L. Murray, L. Pusztai, M. Cristofanilli, B. Arun, B. Esmaeli, H. A. Fritsche, N. Sneige, T. L. Smith and G. N. Hortobagyi, "Phase II Study of Weekly Docetaxel and Trastuzumab for Patients With HER-2–Overexpressing Metastatic Breast Cancer," Journal of Clinical Oncology, vol. 20, no. 7, pp. 1800-1808, 2002.

[4] P. R. Pohlmann, I. A. Mayer and R. Mernaugh, "Resistance to Trastuzumab in Breast Cancer," Clinical Cancer Research, vol. 15, no. 24, pp. 7479-7491, 2009.

[5] P. J. Delves and I. M. Roitt, Roitt's Essential Immunology, 12th ed., Hoboeken: Wiley-Blackwell, 2011.

[6] A. Morell, F. Skvaril, E. van Loghem and M. Kleemola, "Human IgG Subclasses in Maternal and Fetal Serum," Vox Sanguinis, vol. 21, no. 6, pp. 481-492, 1971.

[7] B. Jiang, W. Liu, H. Qu, L. Meng, S. Song, T. Ouyand and C. Shou, "A Novel Peptide Isolated from a Phage Display Peptide Library with Trastuzumab Can Mimic Antigen Epitope of HER-2," Journal of Biological Chemistry, vol. 280, no. 6, pp. 4656-4662, 2005.

[8] Y. Shang, R. Mernaugh and X. Zeng, "Characterization of the Native and Denatured Herceptin by Enzyme Linked Immunosorbent Assay and Quartz Crystal Microbalance Using a High-Affinity Single

Chain Fragment Variable Recombinant Antibody," Analytical Chemistry, vol. 84, no. 19, pp. 8164-8170, 2012.

[9] S. Premjeet, G. Deepika, B. Sudeep, J. Sonam, K. Sahil, R. Devashish and K. Sunil, "Enzyme-Linked Immuno-Sorbent Assay (ELISA), basics and it's application: A comprehensive review," Journal of Pharmacy Research, vol. 4, no. 12, pp. 4581-4583, 2011.

[10] A. . H. C. Ng, U. Uddayasankar and A. R. Wheeler, "Immunoassays in microfluidic systems," Analytical and Bioanalytical Chemistry, vol. 397, no. 3, pp. 991-1007, 2010.

[11] B. Mattiasson, C. Borrebaeck, B. Sanfrindson and K. Mosbach, "Thermometric enzyme linked immunosorbent assay: TELISA," Biochimica et Biophysica Acta (BBA)-Enzymology, vol. 483, no. 2, pp. 221-227, 1977.

[12] F. Lammers and T. Scheper, "Thermal Biosensors in Biotechnology," in Thermal Biosensors, Bioactivity, Bioaffinitty, Berlin Heidelberg, Springer, 1999, pp. 35-67.

[13] B. Lubbers and F. Baudenbacher, "Isothermal Titration Calorimetry in Nanoliter Droplets with Subsecond Time Constants," Analytical Chemistry, vol. 83, no. 20, pp. 7955-7961, 2011.

[14] S. Wang, S. Yu, M. Siedler, P. M. Ihnat, D. I. Filoti, M. Lu, and L. Zuo, "A power compensated differential scanning calorimeter for protein stability characterization," Sensors and Actuators B: Chemical, vol. 256, pp. 946-952, 2018.

[15] V. H. Carreto-Vazquez, Y.-S. Liu, D. B. Bukur and M. S. Mannan, "Chip-scale calorimeters: Potential uses in chemical engineering," Journal of Loss Prevention in the Process Industries, vol. 24, no. 1, pp. 34-42, 2011.

[16] X. Feng, Y. Jia, H. Jiang, Q. Lin, "Microfabrication-based isothermal titration calorimetry using a combined in-mixing and post-mixing titration approach," Analytical Methods, vol. 10, no. 38, pp. 4665-4670, 2018.

[17] E. A. Johannessen, J. M. R. Weaver, P. H. Cobbold and J. M. Cooper, "A suspended membrane nanocalorimeter for ultralow volume bioanalysis," IEEE transactions on nanobioscience, vol. 99, no. 1, pp. 29-36, 2002.

[18] K. Verhaegen, K. Baert, J. Simaels and W. Van Driessche, "A high-throughput silicon microphysiometer," Sensors and Actuators A: Physical, vol. 82, no. 1, pp. 186-190, 2000.

[19] W. Lee, W. Fon, B. W. Axelrod and M. L. Roukes, "High-sensitivity microfluidic calorimeters for biological and chemical applications," Proceedings of the National Academy of Sciences, vol. 106, no. 36, pp. 15225-15230, 2009.

[20] Y. Kudo, M. Nishiwaki, Y. Inoue, N. Seino, T. Nakagama and K. Uchiyama, "Rapid ELISA in Droplet on PDMS Dimple with Nanoliter Reagents Dispensed by Ink-jet Microchip," Chemistry Letters, vol. 37, no. 5, pp. 536-537, 2008.

[21] A. Boyer and E. Cissé, "Properties of thin film thermoelectric materials: application to sensors using the Seebeck effect," Materials Science and Engineering: B, vol. 13, no. 2, pp. 103-111, 1992.

[22] B. Lubbers, Nano-Calorimetry for Point of Care Diagnostics, Nashville, TN: PhD Thesis, Vanderbilt University, 2015.

[23] R. C. Ebersole, J. A. Miller, J. R. Moran and M. D. Ward, "Spontaneously formed functionally active avidin monolayers on metal surfaces: a strategy for immobilizing biological reagents and design of piezoelectric biosensors," Journal of the American Chemical Society, vol. 112, no. 8, pp. 3239-3241, 1990.

[24] J. Baselga, X. Carbonell, N.-J. Castañeda-Soto, M. Clemens, M. Green, V. Harvey, S. Morales, C. Barton and P. Ghahramani, "Phase II Study of Efficacy, Safety, and Pharmacokinetics of Trastuzumab Monotherapy Administered on a 3-Weekly Schedule," Journal of Clinical Oncology, vol. 23, no. 10, pp. 2162-2171, 2005.

Chapter III: Nano-Calorimetry based point of care biosensor for metabolic disease management[2]

By

Evan Kazura, Brad Lubbers, Elliott Dawson, John Phillips III, and Franz Baudenbacher

In Chapter III, a new calorimeter platform is described using on-chip fluid handling powered by capillary forces, an enclosed microfluidic reaction channel, and a differential thermopile calorimeter that eliminates noise from evaporation. The drop calorimeter platform was one of the most sensitive chip calorimeters but drop evaporation limited the time in which assays could be performed. Operation of the drop calorimeter also required precise micropipette placement and picoliter sample handling under a microscope. While the drop calorimeter was extremely sensitive, the low volume of the reaction droplet required to achieve that sensitivity meant the total amount of analyte being detected was very small. We developed the capillary calorimeter platform for point-of-care assays, sacrificing performance for simplified fluid handling. Enclosing the reaction fluid in a microfluidic channel increased the total thermal conductance, which reduced performance, but simplified fluid handling to require neither vacuum insulation nor external pumps for fluid delivery. The capillary platform reduced the device performance by a factor of 3 from the drop platform, but still exceeded the next best microfluidic calorimeter. Both the sensing and reference junctions of the thermopile were located within the microfluidic channel, eliminating errors associated with sample evaporation and heat of dilution. A phenylalanine assay for phenylketonuria (PKU) monitoring was developed around the enzyme

[2] Reproduced with permission from Kazura, E., Lubbers, B. R., Dawson, E., Phillips, J. A., & Baudenbacher, F. (2017). Nano-Calorimetry based point of care biosensor for metabolic disease management. Biomedical Microdevices, 19(3), 50.

phenylalanine ammonia-lyase (PAL). Assays on the platform were limited by the small surface area above the sensing junctions, and reagents were still delivered using micropipettes.

Abstract

Point-of-care (POC) diagnostics represents one of the fastest growing health care technology segments. Developments in microfabrication have led to the development of highly-sensitive nanocalorimeters ideal for directly measuring heat generated in POC biosensors. Here we present a novel nano-calorimeter-based biosensor design with differential sensing to eliminate common mode noise and capillary microfluidic channels for sample delivery to the thermoelectric sensor. The calorimeter has a resolution of 1.4±0.2 nJ/(Hz)$^{1/2}$ utilizing a 27 junction bismuth/titanium thermopile, with a total Seebeck coefficient of 2160 μV/K. Sample is wicked to the calorimeter through a capillary channel making it suitable for monitoring blood obtained through a finger prick (<1 μL sample required). We demonstrate device performance in a model assay using catalase, achieving a threshold for hydrogen peroxide quantification of 50 μM. The potential for our device as a POC blood test for metabolic diseases is shown through the quantification of phenylalanine (Phe) in serum, an unmet necessary service in the management of Phenylketonuria (PKU). Pegylated phenylalanine ammonia-lyase (PEG-PAL) was utilized to react with Phe, but reliable detection was limited to < 5mM due to low enzymatic activity. The POC biosensor concept can be multiplexed and adapted to a large number of metabolic diseases utilizing different immobilized enzymes.

Introduction

The expansion of point-of-care (POC) diagnostics over the past decade has allowed for near instantaneous results for many common blood tests that previously required expensive laboratory equipment and personnel time. With a worldwide market value of over $15.5 billion in 2013, POC diagnostics represents one of the fastest growing health care technology segments [1]. The largest POC

segment, blood glucose monitoring, allows patients themselves to monitor blood glucose levels anywhere [2] [3]. The information provided by the testing is essential for diabetic patients to regulate their glucose levels through medication and diet.

Biosensors are the basis for most POC diagnostic technologies. An enzymatic reaction with the analyte of interest produces a quantifiable signal transduced by one of several different methods; amperometric, optical, calorimetric, or acoustic to name a few [4] [5]. Calorimetry is an attractive detection method as most enzymatic reactions produce heat on the order of 20-100 kJ/mole substrate and are measured directly, not requiring the use of secondary or labeling reactions for transduction as most optical methods do [6]. Calorimetry is based on a temperature measurement and senses heat changes from chemical or physical processes present at the sensor, necessitating the elimination of noise from side reactions and temperature fluctuations [7]. Calorimetric biosensors of the past relied on flow-through columns with enzymes immobilized on a support matrix and thermistors for temperature sensing [4]. These required large sample volumes (>0.5 ml), temperature controls, complex pumping systems, and were only suited to the laboratory setting [8]. Many were successful in measuring sub-milimolar concentrations of common blood analytes like cholesterol, urea, lactate, glucose, and ethanol [7] [9]. The current trend is towards miniaturization, microfluidic sample handing, and on-chip thermoelectric based sensing [10]. In this way sample volume requirements are reduced to the microliter range and minimum detectable energies approaching 1 nJ are possible [11] [12]. A few calorimetric biosensors suited to POC have been developed pertaining to the measurement of blood glucose or urine urea due to the large enthalpy changes associated with these reactions (-80 and -61 kJ/mol) [13] [14]. In the case of Davaji and Lee, a thin film resistive temperature detector is employed, with a minimum detectable temperature change of 26 mK and noise limited minimum glucose concentration of 1.51 mM. A paper strip held the glucose oxidase enzyme in close proximity to the sensing surface, however enzyme was added to the flow strip at the beginning of each measurement,

and evaporative effects caused a large drift in the calorimeter signal. Lai and Tadigadapa's device relied on a Y-cut quartz resonator for temperature sensing, giving higher temperature sensitivity. However, the entire device had to be placed in a 37 ˚C oven during measurements, microfluidic pumping systems were required, and the uncertainty in their urea detection results were too high for reliable use. In order to create a user-friendly calorimeter based POC device, common mode temperature signals must be eliminated, temperature sensitivity increased, sample volume reduced, liquid handing automated, and be insensitive to user error.

Phenylketonuria (PKU) represents another disease where at-home monitoring is needed to help effectively manage the disease. Affecting 1 in 15,000 people worldwide, PKU prevents the metabolism of the essential amino acid phenylalanine (Phe), leading to high blood concentrations that can cause mental retardation if not treated through diet and/or enzyme replacement therapy [15]. Though much faster and more accurate than the bacterial inhibition assays of the 1960's, tandem mass spectrometry (MS/MS) testing of blood Phe levels is still limited to larger scale clinical laboratories [16]. At home Phe monitoring to dictate dosing and diet would save patients from constant visit to clinics and greatly improve their quality of life. With new enzyme replacement therapies for PKU undergoing human clinical trials, the need for Phe monitoring with immediate results to dictate dosing and diet is even greater. Towards the goal of POC Phe testing, we have developed a novel calorimetric biosensor with the ability to measure Phe levels in 1 µL of sample.

Here we present a novel nano-calorimeter-based biosensor design with differential sensing to eliminate common mode noise and capillary microfluidic channels for sample delivery to the thermoelectric sensor. Utilizing capillary forces for fluid movement is reliable and does not require external power or actuators [17]. High sensitivity and ruggedness was achieved by the use of a suspended polymer membrane and bismuth/titanium thin film thermopiles. Catalase (CAT) and phenylalanine ammonia-lyase (PAL) are used in the detection of their respective substrates. Many

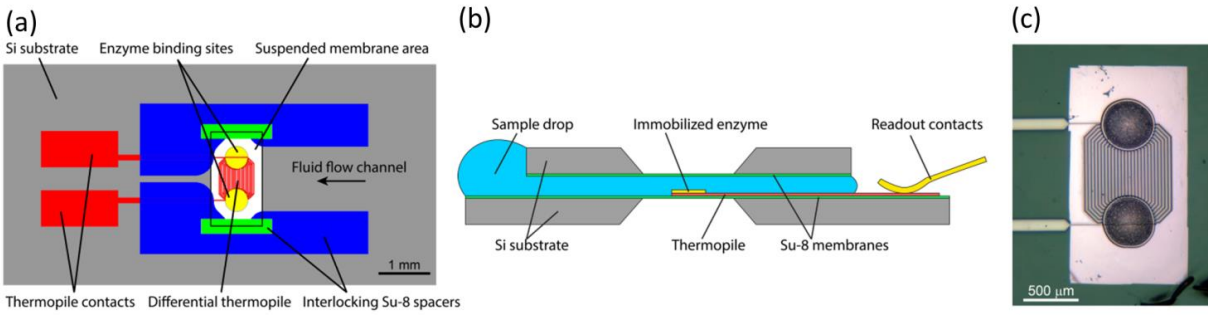

Fig. 1. Differential nanocalorimeter layout. (a) Active and control enzymes are bound to the two reaction zones read out by the 27 junction thermopile. The thermopile junctions are patterned on a suspended Su-8 membrane and line the edges of the enzyme spots to maximize sensitivity. The differential sensing arrangement eliminates errors associated with sample evaporation and heat of dilution. Interlocking Su-8 spaces on the top and bottom substrates allow for accurate alignment of the layers. (b) Device with immobilized enzymes on bottom substrate and capillary channel to deliver sample fluid. The suspended Su-8 membrane over the thermopile allows for very low thermal leakage, thereby maintain high sensitivity. When a sample drop (~1 µL) is placed at the device opening, capillary forces draw the sample into the reaction chamber in less than 1 second. (c) Image of the device with immobilized enzymes on the reaction zones.

common blood analytes (i.e. cholesterol, carbohydrates, and amino acids) have corresponding oxidases which release H_2O_2 during the oxidation of their substrate. The large enthalpy associated with H_2O_2 decomposition (-98 kJ/mol), can be exploited by co-immobilizing these enzymes with CAT, leading to enzymatic amplification of the signal [7]. Most oxidases require O_2 to react and this can be a limiting factor in closed systems since the O_2 saturation of water is only 0.25 mM. Alternative electron acceptors are used, but must be immobilized with the enzymes, increasing complexity and raising stability concerns. In the interest of reducing the number of immobilized components, we focused on systems not requiring external cofactors or enzyme cascades. PAL is one such enzyme, which catalyzes the conversion of l-phenylalanine to trans-cinnamic acid and ammonia with an enthalpy of +24.8 kJ/mol of Phe [18]. Here we present device design and characterization of the capillary calorimeter as well as preliminary data showing milimolar detection of Phe utilizing PAL with the potential of creating a robust at home test for the management of phenylketonuria.

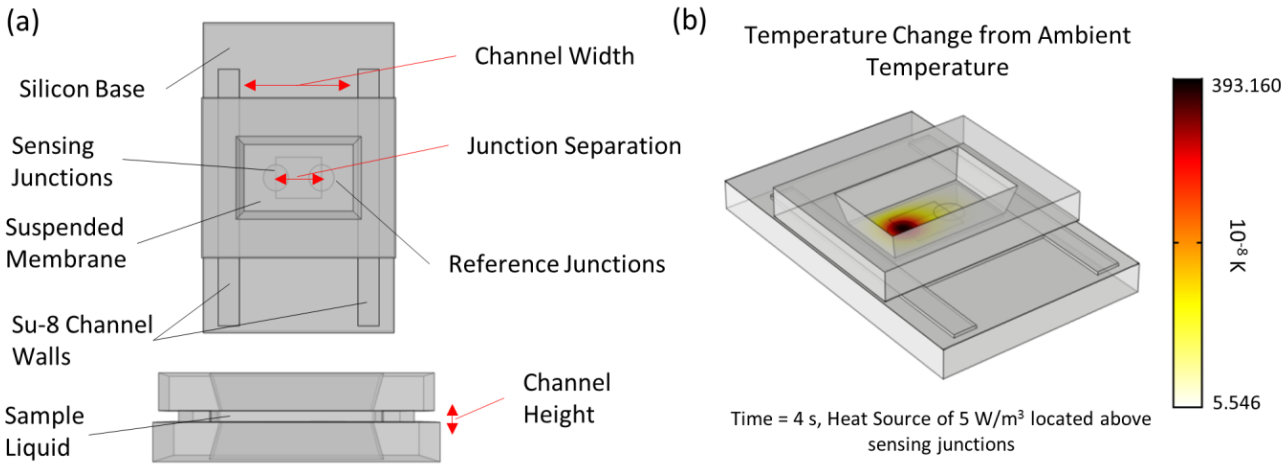

Fig 2. 3D model configuration for optimizing device sensitivity. (a) The COMSOL model consists of a 500 µm thick silicon base with a 1.5 µm thick Su-8 polymer layer on the top surface. A window in the base creates a free-standing membrane, on which are areas designated as the sensing junctions, reference junctions, and the thermopile tracks. Two Su-8 walls runs along the base, and a silicon lid with a matching thin membrane rest on top, forming a microfluidic channel. Parameters that were explored with regard to calorimeter sensitivity were the distance between the two channel walls (channel width), the height of the channel walls (channel height), and the distance between the sensing and reference junctions (junction separation). (b) Calorimeter sensitivity was predicted by running a heat transfer study and determining the temperature difference between the sensing junctions and reference junctions over time. A heat source of 5 W/m^3 was placed in a cylinder of radius 250 µm and height of 5 µm for 5 seconds to represent a reaction of the target analyte catalyzed by immobilized enzyme on the sensing area.

Materials and methods

Reagents and materials

All micromachining was performed in the VIIBRE and VINSE cleanrooms at Vanderbilt University. 75 mm diameter silicon wafers, <100> orientation, double side polished, with 500 nm low stress silicon nitride (SiN) coated on both sides were obtained from WRS Materials (San Jose, CA). Chrome on soda-lime photomasks were fabricated by Front Range Photomask (Palmer Lake, CO). Photoresist and developer were purchased from MicroChem Corp. (Westborough, MA). PEG-PAL was donated by BioMarin (San Rafael, CA). Catalase (CAT) (#C100) and all other chemical are commercially available from Sigma-Aldrich (St. Louis, MO). All reactions were performed at room temperature.

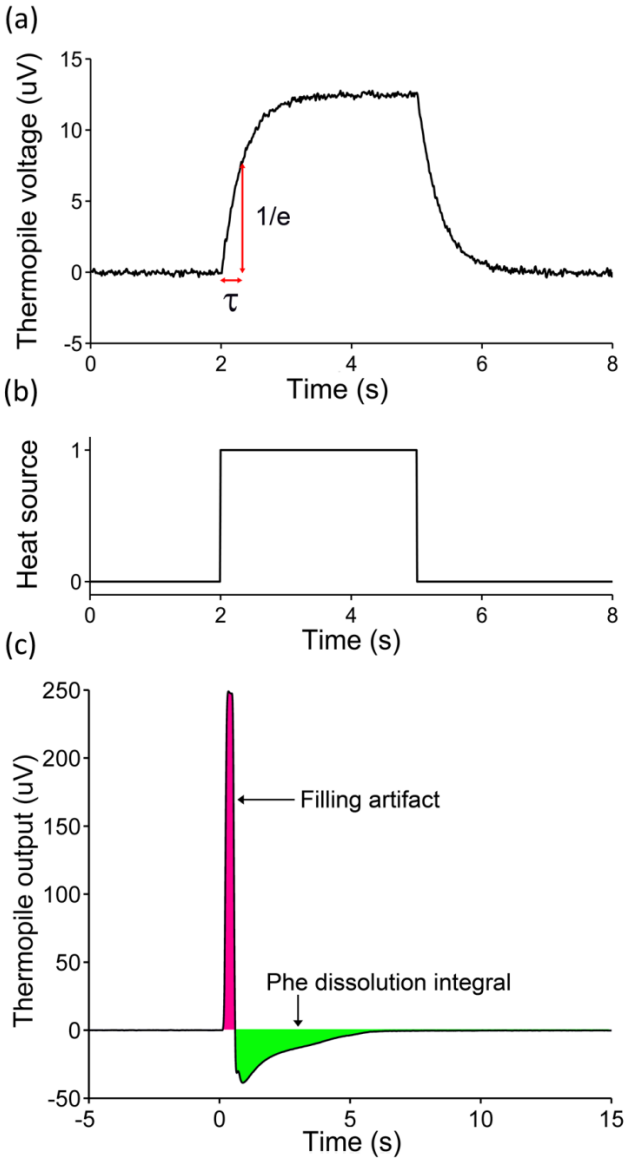

Fig. 3. Device characterization. (a) Device time constant was measured by pulsing a focused laser on the enzyme binding site while the device was filled with dH_2O. The time from pulse start to reciprocal of the natural exponent of the steady state voltage is the time constant. The typical τ for the filled device was 305 ± 5 ms (mean ± s.d., n=10). (b) Laser pulse step function. (c) Sensitivity determination by Phe dissolution. The first 500-1000 ms of the signal is obscured until the device fills with water and the flow stops. The integral of Phe dissolution (green area) is used to calculate the power sensitivity of 7.2 ± 0.4 V/W (mean ± s.d., n=8).

Device modeling

Fig. 1 shows the layout of the device including the differential sensing thermopile and capillary flow channel. As Fig. 1B shows, a low conductance suspended Su-8 membrane forms the top and bottom of the capillary channel around the immobilized enzyme, reducing heat flux to the silicon substrate. The thickness of the capillary channel needed to be low enough to ensure fast wicking of the sample while minimizing the thermal conductance through the sample fluid itself.

A model of the calorimeter was built using COMSOL, and data output was analyzed in MATLAB. Unlike previous iterations [12], the new design loses the radial symmetry of the freestanding drop calorimeter, which allowed for a simplified 2D model. Therefore, a full 3D model was constructed (Fig. 2A). In order to simplify the mesh construction of the thin freestanding membrane where the calorimeter sensing areas are located, the thermal properties of the thermopile metals and polymer membrane were combined and modeled together. A heat source representing the

enzymatic reaction was placed as a cylinder within the sample liquid above the sensing junctions, and calorimeter sensitivity was determined by measuring the difference in temperature between the sensing and reference junctions. Temperatures at the two sensing areas were compared for 30 seconds, when both had returned to the baseline. The temperature difference was then integrated, converted to an expected voltage by multiplying by the total Seebeck coefficient of our thermopiles, then divided by the total energy produced by the heat source to return a sensitivity measurement in V/W (Fig. 3). Channel height, channel width, and sensing junction separation were varied individually and heat flow was modeled to maximize calorimeter sensitivity. Diffusion modeling within the sample liquid was employed to study the movement of substrate into the enzymatic reaction zone and determine if the reactions were diffusion or enzymatic rate limited.

Device fabrication

Fabrication of nanocalorimeters was performed using normal microfabrication techniques. Processing began by etching rectangular windows in the backside SiN layer by reactive ion etching, then anisotropically etching through the silicon in a potassium hydroxide bath, freeing SiN membranes on the frontside of the wafer. A uniform 0.5 μm thick Su-8 layer was deposited over the surface of the wafer, and hard baked until stable to serve as the base membrane for the nanocalorimeters. 200 nm of titanium was deposited by e-beam thermal deposition and patterned by a chemical wet etch of 30:1:1 parts water: hydrogen peroxide: hydrofluoric acid. We found an oxide layer formed on the titanium once exposed to the air, which greatly increased thermocouple resistance within the devices. A clean interface between the two metals of our thermopiles was integral in reducing thermopile resistance, and therefore the Johnson-Nyquist noise associated with it. This was accomplished by ion milling the surface of the titanium, then immediately depositing 400 nm of bismuth without breaking the chamber vacuum. E-beam thermal deposition was used to lay down the bismuth layer, and further ion milling was the method of patterning. In order to electrically insulate the thermopile circuits and protect the metal

surfaces, a second 0.5 µm thick Su-8 layer was deposited as before on top of the devices. Reactive ion etching removed the remaining SiN from the backside of the Su-8, freeing the freestanding membranes and thermally isolating the nanocalorimeters from the wafer. An additional 50 µm thick Su-8 layer was patterned on the device surface to create interlocking spacers for the capillary channel (Fig. 1A). This ensured the top and bottom of the devices were always properly aligned. Device yield was good with less than 10% of devices rejected due to defective traces or broken membranes. Electrical contacts to the thermopile on the chip were built into a spring-loaded holder that also held down the sample lid during measurements. A custom-built low noise amplifier provided signal amplification (gain = 10,000) of the thermopile output voltage and data was recorded in LabVIEW. A 500 µm diameter, 50 nm thick gold spot was deposited through a shadow mask on each side of the thermopile to define a hydrophilic droplet wetting spot amid the hydrophobic Su-8 membrane.

Device characterization

The calorimeter time constant was measured by focusing a light beam onto one side of the differential thermopile and measuring the 1/e time to reach a steady state output voltage (Fig. 3A,B). This was measured while the device was filled with ~1 µL of distilled water. The actual volume of the capillary channel was ~275 nl, but the excess liquid ensured that the channel filled completely without bubbles and compensated for any evaporation of sample. Device sensitivity was measured using the enthalpy of dilution of Phe (+8.20 ±0.05 kJ/mol at 298 K) [19]. Drops of 100 mM Phe in dH_2O at measured volumes between 5-20 nl were spotted onto one thermopile junction and evaporated. The calorimeter lid was reassembled and the device filled with dH_2O while measuring the thermopile output. Sensitivity was calculated by dividing the integral of the signal by the respective amount of Phe on the sensor. Phe has a negligible enthalpy change due to dilution below 100 mM, precluding the need to take into account the integral solution enthalpy. It also dissolves over a period of a few seconds, allowing the device to equilibrate after filling before the Phe has dissolved completely. The uncertainty in the

sensitivity measurements (Table 1) are due to filling noise obscuring the first 500-1000 ms of the Phe dissolution (Fig. 3C).

Enzymatic measurements

The activity of CAT (EC 1.11.1.6) was measure by spectrographically monitoring the consumption of H_2O_2 at 240 nm in 50 mM phosphate buffered saline ph 7.4 (PBS). The activity of PEG-PAL (EC 4.3.1.24) was measure by spectrographically monitoring the production of trans-cinnamic acid at 270 nm in 50 mM Tris-HCl pH 8.5 buffer. The reaction of CAT with hydrogen peroxide was used to demonstrate proof of concept of our differential calorimetric biosensor. CAT suspended in 50 mM phosphate buffered saline pH 7.4 (PBS) at 1,000 units/ml was spotted onto the gold binding zone on one side of a sensor. PBS with 0.1 mg/ml bovine serum albumin (BSA) was spotted onto the other side of the differential sensor. Calibrated glass micropipettes were used to dispense 10 nl of solution for each spot. 1% PVA was added to the CAT/BSA suspension in most cases to aid in confining the enzyme after resuspension in the sample fluid. After assembling the lid onto the sensor and mounting in the device holder, 1 µL aliquots of PBS with H_2O_2 at concentrations between 0-2000 µmol were applied to an individual sensor channel. At higher concentrations of H_2O_2, O_2 generated by the reaction formed bubbles and resulted in inconsistent readings. After H_2O_2 application, the output signal was integrated over a period of 30 s and divided by the device sensitivity determined experimentally to obtain the total energy.

The quantification of Phe was accomplished using calorimetric detection with the enzyme PEG-PAL. Unmodified PAL has poor tolerance to desiccation, losing 50% activity upon exposure to moist air after drying [20]. Pegylated PAL was developed to decrease clearance rates when used for PKU therapy; however, the PEG group also increases tolerance to desiccation. We performed an activity assay utilizing PEG-PAL desiccated in the presence of 1% PVA and showed 86% activity retained. Due to the low activity of PAL (~ 2 units/mg), high concentration loading on the sensor surface is needed. PEG-PAL was supplied

at 20 mg/ml in 150 mM NaCl, 10 mM tris-HCl pH 7.5. PVA was added to a final concentration of 1% w/v and 10 nl of the enzyme mix spotted onto one enzyme binding spot on the differential calorimeter. Control enzyme was created by heating PEG-PAL suspension to 60 ˚C for 60 minutes before spotting 15 nl onto the control binding site. Assays showed no activity after heat treatment. Phe at 0-10 mM in 50 mM tris-HCl pH 8.3 was introduced into the assembled capillary calorimeter and monitored for up to 1 min. If more PEG-PAL was loaded onto the sensor surface, variance should decrease due to shorter integration times, so a second set of tests were run with PEG-PAL that was spin concentrated using Amicon Ultracel 30K MWCO filters. However, the samples were too viscous to reliably pipette onto the sensor surface and dissolved inconsistently, leading to excessive errors.

Results and discussion

Modeling Design Results

The results from the modeling guided the calorimeter design along the explored parameters. The configuration of the fluid sample was changed from a freestanding drop in previous calorimeter models to an enclosed channel. The membrane window was maximized with respect to stability to isolate the thermopiles from the high thermal conductance of the silicon wafer base. The calorimeter sensitivity was found to be inversely proportional with channel height (Fig. 4A). Similarly, a narrower channel also increased sensitivity of the device (Fig. 4B). As the volume of the liquid within the channel increased, so did its total heat capacity. This, combined with the higher thermal conductivity of the liquid relative to the Su-8 forming the membrane and walls of the channel (0.6 W/(m*K) and 0.2 W/(m*K), respectively), led to more heat being drawn away from the sensing elements embedded in the membrane, reducing sensitivity. These results guided the design process to balance reducing the channel cross section, in order to isolate the sample within from the wafer base, while still allowing for use without precise liquid measurement and placement. A height of 50 µm and width of 2355 µm were chosen as the smallest height and width while still allowing for easy sample loading by capillary forces.

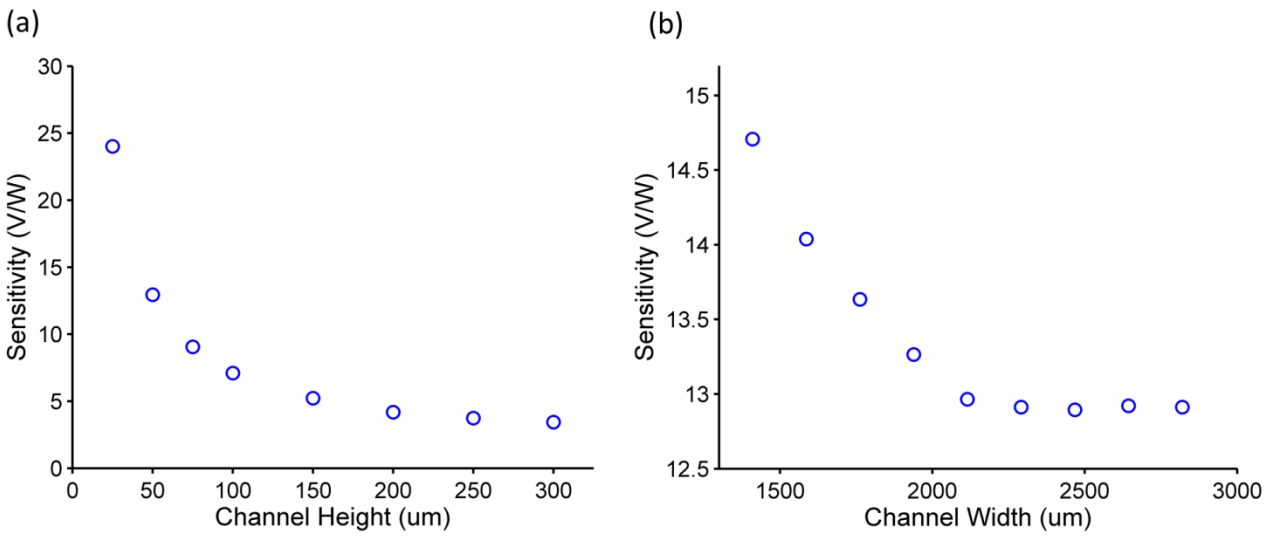

Fig. 4. Model Predictions of Sensitivity by Channel Dimensions. (a) The height of the channel walls was varied from 25 to 300 µm and resulting sensitivity was found. Decreasing the height reduces the total device heat capacity. 50 µm was chosen as the shortest height for the channel without complicating loading of the sample with clogging. (b) Holding the height at 50 µm, the spacing between the channel walls was simulated between 1410 and 2820 µm. Calorimeter sensitivity remained roughly constant until the walls were placed over the thin membrane, further isolating the liquid sample from the silicon base of the device

The second major design change from previous iterations was moving the reference thermopile junctions of the calorimeter from over the silicon base to a differential mode onto the membrane within the sample channel. Previous designs had reference junctions radiating away from the thin membrane and located above the silicon wafer base, anchoring the reference temperature to room temperature with the comparably immense thermal conductivity of 149 W/(m*K). Calorimeter sensitivity was optimized by shortening thermopile length to reduce Johnson noise while ensuring the membrane was large enough to isolate the reaction [12]. The new

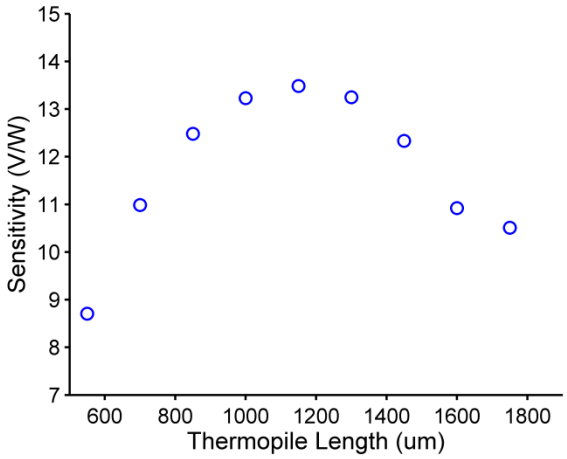

Fig. 5. Junction Separation Modeling. With the channel height and width held at 50 µm and 2355 µm, respectively, the effect of the distance between the sensing and reference junctions was simulated. A range of 550 µm to 1750 µm was explored. A maximum sensitivity of 13.5 V/W was found at 1200 µm between the junctions. However, the lengthening the thermopile tracks also increases Johnson noise from the resistance, so a junction separation of 910 µm was chosen.

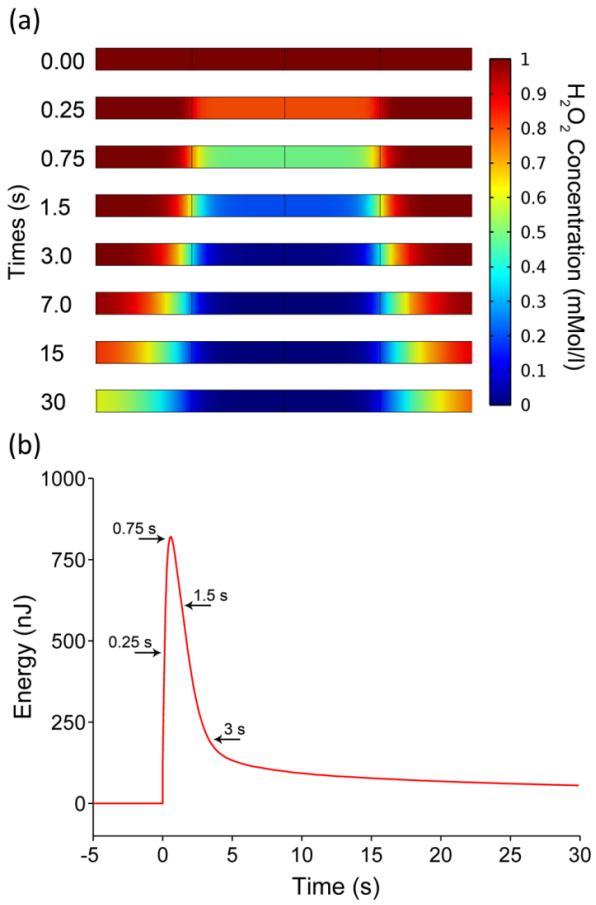

Fig. 6. Hydrogen peroxide diffusion modeling. (a) Side view of peroxide concentration from COMSOL modeling showed peroxide was quickly consumed by catalase at the local enzyme binding site. After 3 s peroxide consumption became diffusion-limited as the local concentration went to 0 mM. The left side is the dead end of the device, the right is the filling channel open to the reservoir. (b) The modeled thermal output from peroxide consumption shows a quasi-steady-state after local depletion. The steady state output is diffusion limited and the integrated signal is independent on the enzyme activity.

design moves the reference junction to within in the microfluidic channel, allowing for a differential setup. By modeling a range of spacings between the sensing and reference junctions, calorimeter sensitivity was maximized (Fig. 5). If the two areas were too close together, heat from the reaction zone above the sensing junction reached the reference junctions and decreased the overall temperature difference. If the junctions were close to the edge of the membrane, heat was lost at a greater rate through the silicon base. Combining this data with the increase in resistance from lengthening the metal thermopile tracks led to the optimal spacing of 910 µm. The model with this configuration of the microfluidic channel and thermopile calorimeter predicts a sensitivity of 12.9 V/W.

Peroxide diffusion modeling was then done to determine if a catalase-based reaction would be a proper assay to develop on our device. The time course of the reaction is largely determined by the diffusion of peroxide into the enzymatic reaction zone (Fig. 6). Diffusion modeling showed peroxide directly above the immobilized CAT is consumed in the first 3 s after sample addition. After local consumption, the reaction becomes diffusion limited, reducing the energy flux to a quasi-steady-state that persists for many second afterwards (Fig. 6B). Therefore, the energy integral is not significant affected by moderate changes in enzyme activity.

Device performance

As predicted by our COMSOL model, the addition of a fluid filled capillary channel reduced our device performance by a factor of 3 as compared to our previous nanocalorimeter in terms of power sensitivity, time constant, and minimum detectable power (Table 1). However, this still exceeds the minimum detectable energy of the next best microfluidic based calorimeter by a factor of 3 (i.e. 1.4 vs. 4.2 $nW/Hz^{1/2}$ for the Lee et al. device [11]). Our device requires neither the vacuum insulation of the device by Lee et al., nor the use of pump and sacrificial channel fillers during fabrication. By utilizing a wide, 50 µm high channel, our device does not suffer from the clogging commonly associated with other microfluidic systems when flowing particle laded fluids like blood [17]. The hydrophobic nature of the Su-8 making up the surface of the channel caused failures or incomplete filling, but was rectified by exposing the calorimeters to 30 seconds of oxygen plasma.

Table 1. Device properties. Means ± s.d. are shown (n=6-18 per value).

Parameter	**Symbol**	**Unit**	**Value**
Thermal time constant	τ	ms	305 ± 5
Power sensitivity	P_{sens}	V/W	7.2 ± 0.4
Minimum detectable power	P_{min}	$nJ/(Hz)^{1/2}$	1.4 ± 0.2
Total thermal conductance	G_{tot}	µW/K	300 ± 24
Total Seebeck coefficient	S_{tot}	µV/K	2160
Effective thermal mass	C_{tot}	µJ/K	91.5
Thermopile resistance	R	kohms	11.5 ± 2.1

Since our device utilizes a closed configuration in conjunction with a differential sensing thermopile, evaporation effects are eliminated as shown by the steady baseline before and after filling (Fig. 3C). Originally, the filling noise created some error in the sensitivity determination, since the first 500 - 1000 ms of signal is lost and integration began after the final zero crossing. Signal variability was reduced by gating out the first 1000 ms of signal, regardless of the final zero crossing time.

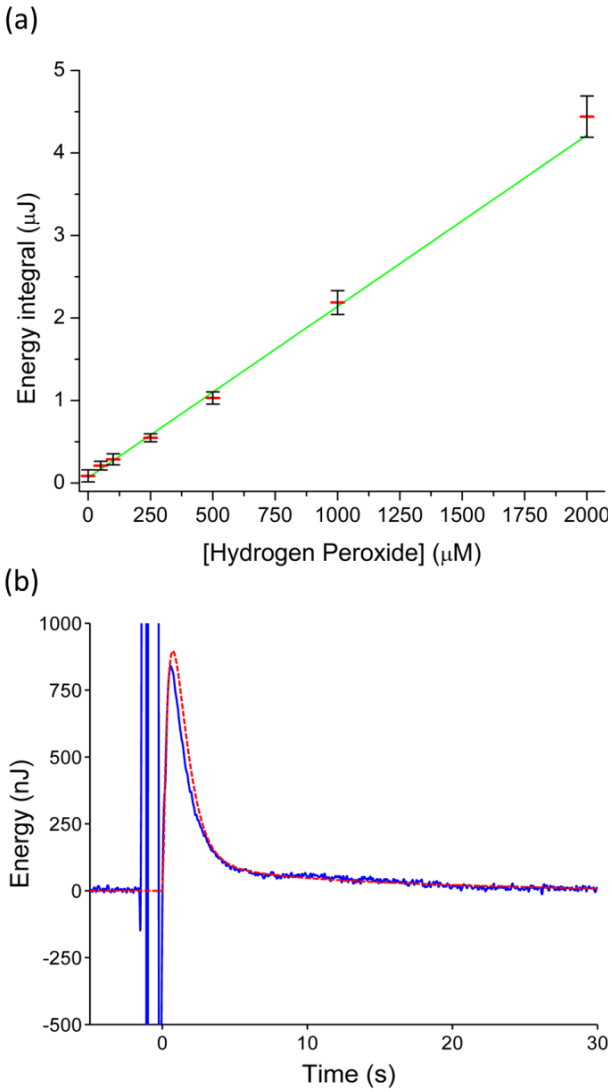

Fig. 7. Catalase assay. (a) Hydrogen peroxide concentration response when reacted with immobilized catalase on the capillary calorimeter. With a linear fit of R^2 = 99.24 and uncertainty of ±75μM, a detection limit of 100 μm H_2O_2 can be achieved. Means ± s.d. are shown (n=4 per point). (b) Representative output from 1000 μM H_2O_2 reacting with CAT overlaid with diffusion modeling results (red line). The instability of the signal before 0 s is due to the filling of the device and causes uncertainty in the energy integral since it partly obscures the signal.

Hydrogen peroxide assay

The differential sensing capillary calorimeter provides a new approach to POC testing of many blood analytes. We used the detection of H_2O_2 as a model system to demonstrate device performance and validate our model in terms of diffusion, enzyme kinetics and heat flow. Fig. 7B shows that our measured data correspond well to the model predictions which could be used for correcting the signal during the filling of the device. This could aid in reducing error and extending our minimum detectable concentration. The energy integral correlates well with H_2O_2 concentration with a concentration uncertainty of ~75 μM below 500 μM (Fig. 7A). Measurements at 50 μM were significantly different from those at 0 mM (P=0.035). When the amount of CAT bound to the sensor was reduced by one-half, the integral only decreased by 6% at the 1000 μM level. Though currently not sensitive enough to measure normal H_2O_2 levels in the blood (~2.5 μm), H_2O_2 levels in urine levels are greater (up to 100 μM) and high levels are indicative of oxidative stress [21]. Therefore our current device could be a useful tool for urinalysis and with further improvement could be

applicable to blood peroxide determination. By measuring a signal integral over a finite time, rather than a rate as in most blood glucose POC sensors, our device is less sensitive to changes in enzyme activity. This is essential since CAT is not permanently immobilized to the sensor surface, but rather dried onto it. If an excess of sample (i.e. > 1 µL) is added to the device, more enzyme is lost as it is swept away by the initial flow. Once flow ceases, the remaining enzyme stays localized due to the small diffusion coefficient of CAT compared to H_2O_2 (4.1 x 10^{-7} vs. 1.3 x 10^{-5} cm^2/s) [22]. Other sources of error are related to the heat of dilution of the enzyme spots. If both spots are not of equal size and well centered on the thermopiles, unintended baseline shifts can occur. The gold spots currently used do not always limit the spread of liquid enzyme droplets before drying and devices with poorly matched spots were rejected. Future research, into techniques such as screen printing enzyme pastes are needed to improve sensitivity and robustness.

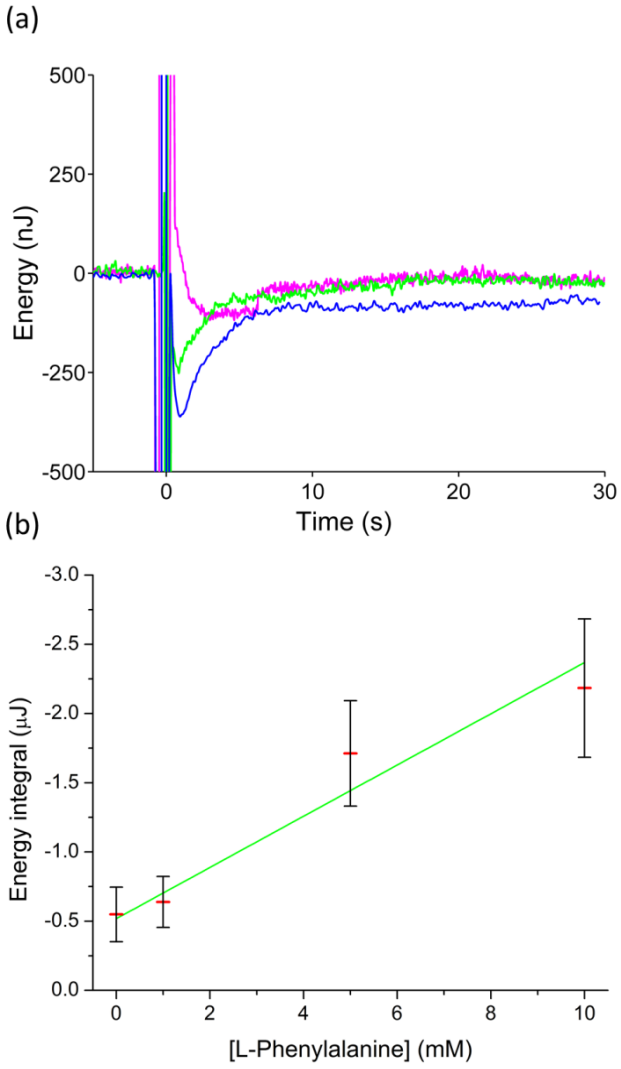

Fig. 8. Phenylalanine assay (a) Representative signals from 10 mM (blue), 5 mM (green), and 0 mM (magenta) Phe reacting on the capillary calorimeter. The low activity of PEG-PAL leads to a longer integration time and greater error associated with baseline drift. (b) Phe concentration response when reacted with immobilized PEG-PAL on the capillary calorimeter. Phe concentration confidence is lower with an $R^2 = 0.9295$ and uncertainty of ± 3 mM. This is due to the lower activity of PEG-PAL compared to CAT, smaller reaction enthalpy, and greater error associated with rehydration of the dried PEG-PAL. Means ± s.d. are shown (n=4 per point).

Phenylalanine assay

The calorimetric quantification of Phe by reaction with PEG-PAL showed that simple enzymatic reactions could be used to measure common blood analytes without the need for expensive optical or MS/MS systems. The energy integral correlated well with Phe concentration (R^2=0.9295), however noise at low concentrations limit the minimum detectable concentration to around 5 mM (Fig. 8B). As Fig. 8A shows, we can differentiate clearly between 5 and 10 mM but baseline drift prevents us from reliably detecting concentration of less than 5mM. At 1 mM the detection was inconsistent compared to the CAT reactions with 1 mM H_2O_2 (i.e. ± 40% vs 6% error). Measurements at 1 mM were not significantly different from 0 mM readings (P=0.57), but were at 5 mM and 10 mM (P=0.0039) (Fig. 8B). Though this limit is well above the recommended Phe range for PKU patients (120-900 μM) [23], slight improvements would enable the device to be used for high level threshold detection. This would allow patients to detect abnormally high Phe levels at home, and report to their doctor for more thorough testing. We found that the pegylation of PAL helped preserve activity upon drying and helped to localize the enzyme to the thermopile upon rehydration with the sample fluid. As with the H_2O_2 assay, a main source of error was due to uneven dissolution of the enzyme spots, but was compounded by the lower reaction enthalpy and activity of PAL. With our diffusion model, we estimated 0.0078 units of CAT were present after sample addition, but only 0.0006 units of PEG-PAL remained. If another Phe reacting enzyme (i.e. phenylalanine 2-monooxygenase, EC 1.13.12.9) were used, which has potentially 50 times higher activity [24], sub-milimolar Phe detection would be possible. However, phenylalanine 2-monooxygenase does not have the commercial availability of PAL.

Conclusions

Compared to previous experiments performed on our standing drop nano-calorimeters [12], error due to evaporation and heat of dilution upon sample injection is greatly reduced with our current design. Utilizing a differential sensing approach eliminates theses errors and in combination with the

capillary liquid handling eliminates the need for nanoliter scale sample handling making this approach ideally suited for a POC device. Even though sensitivity is reduced by a factor of 3, these devices still have the ability to measure milimolar concentrations of blood analytes. Since the space required for each thermopile is small (~1 mm^2), it would be possible to include several sensors in one capillary channel. These could provide control reactions, averaging to reduce noise, or monitor several analytes at once.

Acknowledgements

This work was supported by a grant from BioVentures, Inc. We thank Raymond Mernaugh for assistance with enzyme binding and reactions.

References

[1] M. Elder, "Point of Care Diagnostics," BCC Research, Wellesley, MA, 2014.
[2] L. Ben Mohammadi, T. Klotzbuecher, S. Sigloch, K. Welzel, M. Goeddel, T. R. Pieber and L. Schaupp, "Clinical performance of a low cost near infrared sensor for continuous glucose monitoring applied with subcutaneous microdialysis," Biomedical Microdevices, vol. 17, no. 73, 2015.
[3] A. Soni and S. K. Jha, "A paper strip based non-invasive glucose biosensor for salivary analysis," Biosensors and Bioelectronics, vol. 67, pp. 763-768, 2015.
[4] B. Danielsson, "The enzyme thermistor," Applied Biochemistry and Biotechnology, vol. 7, pp. 127-134, 1982.
[5] J. I. R. De Corcuera and R. P. Cavalieri, Encyclopedia of agricultural, food, and biological engineering, Taylor and Francis, 2007.
[6] B. Danielsson, "Calorimetric biosensors," Journal of Biotechnology, vol. 15, no. 3, pp. 187-200, 1990.
[7] F. Lammers and T. Scheper, "Thermal Biosensors in Biotechnology," in Thermal Biosensors Bioactivity Bioaffinity, Berlin, Springer-Verlag Berlin Heidelberg, 1999, pp. 35-67.
[8] F. Lammers and T. Scheper, "On-line monitoring of enzyme-catalyzed biotransformations with biosensors," Enzyme and Microbial Technology, vol. 20, no. 6, pp. 432-436, 1997.
[9] B. Xie, K. Ramanathan and B. Danielsson, "Principles of Enzyme Thermistor Systems: Applications to Biomedical and Other Measurements," in Thermal Biosensors, Bioactivity, Bioaffinity, Springer-Verlag Berlin Heidelberg, Berlin, 1999, pp. 1-33.
[10] K. Verhaegen, J. Simaels, W. Van Driessche, K. Baert, W. Sansen, B. Puers, L. Hermans and R. Mertens, "A Biomedical Microphysiometer," Biomedical Microdevices, vol. 2, pp. 93-98, 1999.
[11] W. Lee, W. Fon, B. W. Axelrod and M. L. Roukes, "High-sensitivity microfluidic calorimeters for biological and chemical applications," PNAS, vol. 106, no. 36, pp. 15225-15230, 2009.
[12] B. Lubbers and F. Baudenbacher, "Isothermal Titration Calorimetry in Nanoliter Droplets with Subsecond Time Constants," Analytical Chemistry, vol. 83, no. 20, pp. 7955-7961, 2011.

[13] B. Davaji and C. H. Lee, "A paper-based calorimetric microfluidics platform for bio-chemical sensing," Biosensors and Bioelectronics, vol. 59, pp. 120-126, 2014.
[14] S. V. H. Lai and S. Tadigadapa, "Calorimetric sensing system for real-time urea and creatinine measurements," in Sensors, 2012 IEEE, Taipei, 2012.
[15] A. Gámez, L. Wang, M. Straub, M. G. Patch and R. C. Stevens, "Toward PKU Enzyme Replacement Therapy: PEGylation with Activity Retention for Three Forms of Recombinant Phenylalanine Hydroxylase," Molecular Therapy, vol. 9, no. 1, pp. 124-129, 2004.
[16] S. A. Banta-Wright and R. D. Steiner, "Tandem Mass Spectrometry in Newborn Screening: A Primer for Neonatal and Perinatal Nurses," Journal of Perinatal & Neonatal Nursing, vol. 18, no. 1, pp. 41-60, 2004.
[17] C. D. Chin, S. Y. Chin, T. Laksanasopin and S. K. Sia, "Low-Cost Microdevices for Point-of-Care," in Point-of-Care Diagnostics on a Chip, Berlin Heidelberg, Springer-Verlag, 2013, pp. 3-21.
[18] Y. B. Tewari, E. Cajewski and R. N. Goldberg, "An Equilibrium Study of the Conversion of L-Phenylalanine to trans-Cinnamic Acid and," Journal of Physical Chemistry, vol. 91, no. 4, pp. 904-909, 1987.
[19] A. V. Kustov and V. P. Korolev, "The thermodynamic parameters of solution of L-phenylalanine in water," Russian Journal of Physical Chemistry A, vol. 81, no. 2, pp. 193-195, 2007.
[20] D. G. Rees, D. H. Jones, “Stability of l-phenylalanine ammonia-lyase in aqueous solution and as the solid state in air and organic solvents,” Enzyme and Microbial Technology, vol. 19, no. 4, pp. 282-288, 1996.
[21] B. Halliwell, M. V. Clement and L. H. Long, "Hydrogen peroxide in the human body," FEBS Letters, vol. 486, no. 1, pp. 10-13, 2000.
[22] M. T. Tyn and T. W. Gusek, "Prediction of diffusion coefficients of proteins," Biotechnology and Bioengineering, vol. 35, no. 4, pp. 327-338, 1990.
[23] N. Longo, C. O. Harding, B. K. Burton, D. K. Grange, J. Vockley, M. Wasserstein, G. M. Rice, A. Dorenbaum, J. K. Neuenburg, D. G. Musson, Z. Gu and S. Sile, "Single-dose, subcutaneous recombinant phenylalanine ammonia lyase conjugated with polyethylene glycol in adult patients with phenylketonuria: an open-label, multicentre, phase 1 dose-escalation trial," The Lancet, vol. 384, no. 9937, pp. 37-44, 2014.
[24] H. Koyama, "Purification and Characterization of a Novel L-Phenylalanine Oxidase (Deaminating and Decarboxylating) from Pseudomonas sp. P-501," The Journal of Biochemistry, vol. 92, no. 4, pp. 1235-1240, 1982.

Chapter IV: A Capillary Perfused Nanocalorimeter Platform for Thermometric Enzyme-linked Immunosorbent Assay with Attomole Sensitivity[3]

By

Evan Kazura, Ray Mernaugh, and Franz Baudenbacher

Chapter IV ties the time course of the full enzyme reaction to the enzyme amount, creating a novel method of assaying target analytes labeled with enzyme. This method improved the quantitative nature of the enzyme-based assays run on our platform and their robustness to changing conditions. 2D and 3D modeling was used in chapters II and III to optimize the design of our calorimeter platforms but had limited it to the platform response to a simple heat source. Using finite element numerical modeling, we simulated an enzyme-catalyzed reaction within the microfluidic channel of the capillary calorimeter platform, then converted the result to a heat profile, assigned it to the reaction zone within the microfluidic channel, and calculated a calorimeter signal based on the resulting temperature changes. This single comprehensive model interrogated the Michaelis-Menten governed enzyme kinetic reaction to determine the entire time course of the assay for the first time to extract the enzyme amount. Previously, results from the enzyme-based assays relied on phenomenological measurements to determine the results and were susceptible to error from changing enzyme kinetics. The comprehensive model was used to calibrate for enzyme kinetics, and then simulate the entire time course of the reaction. The labeling enzyme amount was determined by minimizing the error to the experiment signal. Using the model-assisted method of determining enzyme amount, the limit of detection (LOD) of the catalase-H_2O_2 thermometric enzyme-linked immunosorbent assay (TELISA) was found to be 260 attomoles of enzyme. This was a considerable improvement over the 25 femtomole

[3] Under revision for publication

acid-base neutralization LOD in chapter II. The improvement was due to the model assisted interpretation of a reaction occurring over time and enzyme calibration instead of phenomenological determination of either the signal peak or decay time constant.

Abstract

Enzyme-catalyzed chemical reactions produce heat. We developed an enclosed capillary perfused nanocalorimeter platform for thermometric enzyme-linked immunosorbent assay (TELISA). We used catalase as enzymes to model the thermal characteristics of the micromachined calorimeter. Model-assisted signal analysis was used to calibrate the nanocalorimeter and to determine reagent diffusion, enzyme kinetics and enzyme concentration. The model-simulated signal closely followed the experimental signal after selecting for the enzyme turnover rate (kcat) and the inactivation factor (InF) using a known label enzyme amount (Ea). Over four discrete runs (n=4), minimized model root mean square error (RMSE) returned 1.80±0.54 fmol for the 1.5 fmol experiments and 1.04±0.37 fmol for the 1 fmol experiments. The experimental limit of detection for the catalase-based TELISA using 10 mM of substrate was calculated to be 260 attomoles. Determination of enzyme parameters through calibration is a necessary step to track changing enzyme kinetic characteristics and improves on previous methods to determine label enzyme amounts on the calorimeter platform. The results obtained using model-system signal analysis for calibration lead to significantly improved nanocalorimeter platform performance.

Introduction

Enzyme linked immunosorbent assays (ELISAs) are the gold standard for detecting and quantifying biological markers in samples, including antigens, antibodies, proteins, and cancer biomarkers [1] [2]. Most commercially-available ELISA kits utilize enzyme conjugated reagents (e.g. antibodies) specific for a target analyte to produce a colorimetric, chemiluminescent, or fluorescent

signal that can be quantified using a microtiter plate reader. One of the most common enzymes used in optical ELISAs is horseradish peroxidase (HRP, EC 1.11.1.7), which catalytically reduces hydrogen peroxide (H2O2) with electrons donated from a second substrate that subsequently undergoes a colorimetric change to produce a quantifiable optical signal for the ELISA. Mattiason, et al. first developed an ELISA with a calorimetric readout, and called it a Thermometric ELISA (TELISA) [3]. TELISA produces a direct readout from the heat produced by the enzymatic reaction. The original TELISA calorimetric biosensor used flow-through columns with immobilized enzymes, requiring large sample volumes greater than a finger prick, ambient temperature controls, and external pumps for liquid handling. Although the design of the TELISA successfully demonstrated a proof-of-principle, the design was not suited for use in point-of-care (POC) applications [4]. Advances in micromanufacturing have made possible the development of microfluidic calorimeters that can be used as platforms to carry out TELISA. Nanocalorimeter-based TELISAs can rapidly detect small temperature changes in enzyme-based immunoassays to produce fast, quantifiable electronic readouts [5] [6]. As such, microfabricated devices used to carry out TELISAs can be competitive with traditional ELISAs. Nestorova, et al. showed the feasibility of TELISA without complex temperature control in determining the 8-hydroxy-2-deoxyguansoine (8OHdG) levels in urine [7]. Xu, et al. utilized flow-injection analysis TELISA to detect Diazepam in beverages, achieving a limit of detection (LOD) of 43.8 picomoles with minimal sample pretreatment [8]. Both systems take advantage of TELISA for rapid results without expensive imaging equipment. However, both require external pumps for liquid sample handling, limiting the approach to a lab setting.

ELISAs can be used to quantify a wide range of molecules using well-characterized enzymatic reactions to correlate the amount of enzyme present in an assay to the amount of target (e.g. an antigen) in a sample. Enzyme-linked antibodies are commonly used in traditional ELISAs as reporter molecules to directly or indirectly detect a target analyte. Since enzymes used in ELISAs produce heat as

a byproduct of an enzyme catalyzed reaction, a calorimeter becomes an easily adaptable and customizable platform to detect enzymes, as indicators of antigen presence, in TELISAs. Hydrogen peroxide is a commonly used substrate in ELISAs. It is ideal due to its high reaction enthalpy (-98 kJ/mol) and large catalog of reactive enzymes (e.g. catalase, or HRP, etc.). Catalase (CAT, EC 1.11.1.6) catalyzes the decomposition of H2O2 into water and oxygen, a well characterized reaction. While HRP requires an enzyme donor in addition to H2O2, the single substrate reaction of CAT simplifies the reaction chemistry involved, aiding in nanocalorimeter assay design, electronic signal acquisition and data interpretation. CAT also features faster turnover rates than HRP, so small amounts of the enzyme can turn over more substrate quickly. This has the potential to improve sensitivity when labeling small amounts of target analyte with an enzyme. CAT becomes inactivated after catalyzing 107 hydrogen peroxide molecules, adding a complication to the assay when using high substrate concentrations over a long duration [9].

We have successfully developed highly sensitive nanocalorimeter TELISA platforms to detect herceptin and phenylalanine in serum [10] [11]. The devices featured a small profile, required nanoliter volumes of sample, and were mass produced by standard batch microfabrication techniques. Previous work showed a calorimeter thermal time constant of 325 ms and an energy sensitivity of 1.4 $nJ/Hz^{1/2}$. For comparison purposes, this translaties to a LOD of 25 femtomoles (fmol) for an acid-base neutralization reaction [10]. Nanocalorimeter fluid handling was driven by capillary forces, and assay readouts were obtained via direct voltages. Although the nanocalorimeter platform's performance has been explored and is well understood, determining the enzyme amount is challenging. Previously, enzyme-based calorimeter assays were simplified using a phenomenological approach by solely measuring the total amount of substrate consumed or the decay time for the first several seconds of a heat/voltage generating reaction to determine results. This added potential sources of error did not exploit the full time course and required assays based on reactions with high enthalpies and fast kinetics. In our previous studies, modeling using radial 2D simulation guided our nanocalorimeter

platform design. However, that approach did not apply to the nanocalorimeter's microfluidic channel geometry and did not include the kinetics of chemical reactions.

In the present study, we incorporate finite element numerical modeling simulating both the enzyme reaction, substrate diffusion, and the physical characteristics of a capillary-driven POC calorimeter platform. We use a single comprehensive model to interrogate the Michaelis-Menten governed enzyme kinetic reaction to determine the entire time course of the assay for the first time to extract the enzyme amount. We demonstrate the use of model-assisted signal analysis to calibrate enzyme kinetics for experimental sets and determine enzyme amounts correlated to a target substance in a TELISA operation. This complete analytical approach allowed us to reduce the LOD to attomole levels on our nanocalorimeter platform.

Experimental Section

Nanocalorimeter Platform Layout

Figure 1A shows a top-down representation of the nanocalorimeter platform base. The platform consists of a thermally isolated reaction zone with a differential thermopile to measure reaction enthalpies. The reaction zone is integrated in a microfluidic channel which consists of two thin membranes separated by two strips of thick photoresist forming the channel walls. The two membranes are supported by a silicon wafer. Anisotropic etching of the silicon above and below the calorimeter location forms a suspended membrane, and the bismuth (Bi) and titanium (Ti) thermopile is deposited to form the calorimeter. A second thin layer of Su-8 encapsulates the thermopile, ensuring the nanocalorimeter is isolated electrically and protected from chemical reactions occurring on the platform. Walls complete a Su-8 polymer-lined microfluidic channel for substrate delivery to the reaction zone above the calorimeter (Figure 1B). The nanocalorimeter senses temperature differences using a 27 junction Bi/Ti thermopile (Figure 1C). Sensing and reference junctions are arranged in 500 µm

diameter semicircles. The low thermal conductance and thin profile of the membrane minimizes heat flux away from the sensing elements into the silicon base, thermally isolating the reaction zone on the nanocalorimeter to ensure high sensitivity. Both junction sets are located in the microfluidic channel, which allows for compensation for unwanted reaction enthalpies in differential calorimetry. We used this to subtract the heat of dissolution by exposing the reference junctions with denatured enzyme [10].

The thermopile self-generates a voltage difference proportional to a difference in temperature between the sensing and reference junctions. The output voltage is amplified by a 10,000x custom-built low noise amplifier, and recorded using a custom National Instruments LabVIEW software module. In order to verify our results from modeling and determine the LOD for TELISA on the nanocalorimeter

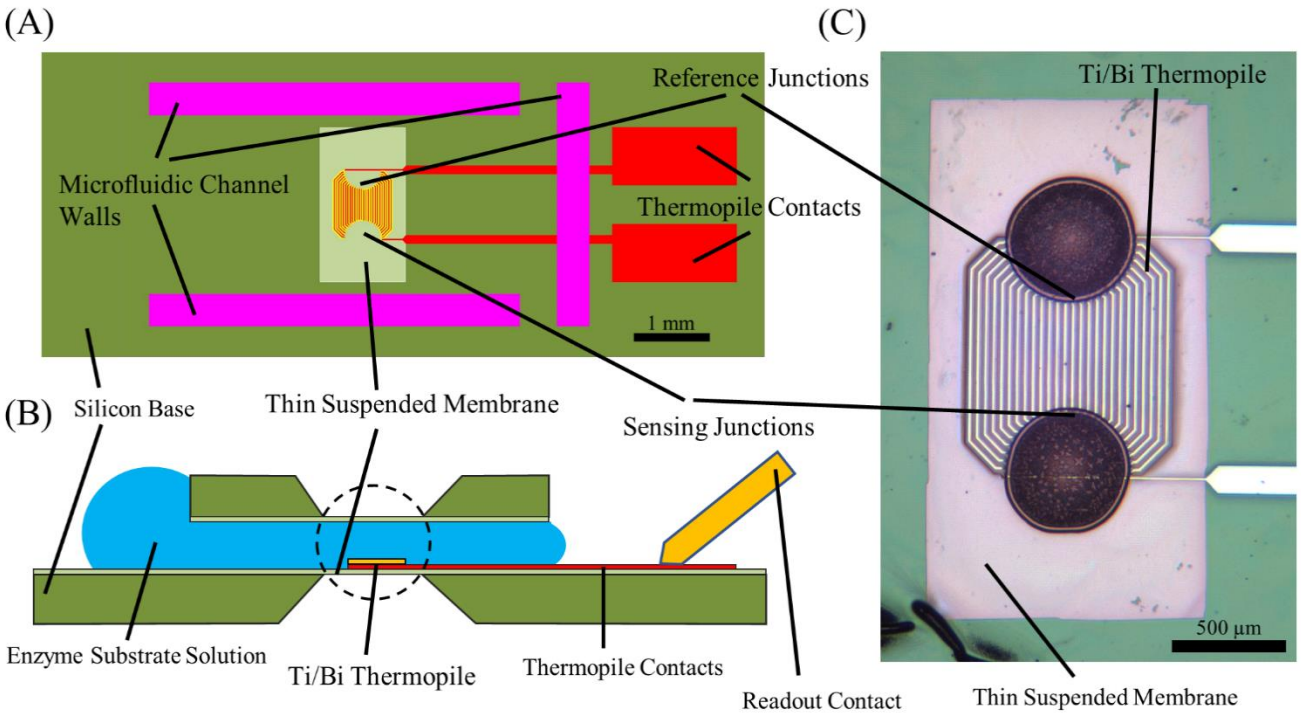

Figure 1. (A) Nanocalorimeter platform consisting of an Su-8 polymer thin membrane on a silicon base, Su-8 walls, and a thermopile calorimeter. (B) A second Su-8 membrane on silicon seated on the walls form a microfluidic channel around the calorimeter. The thin membrane thermally isolates the reaction zone and calorimeter sensing and reference junctions from the environment. Liquid placed at entrance to the microfluidic channel is drawn in by capillary forces, filling the channel without external pumps. (C) The calorimeter consists of a 27 junction Bi/Ti thermopile in differential format. Sensing junctions and reference junctions are each arranged in a semicircle on the freestanding thin membrane. The temperature difference between the sensing junctions and reference junctions generates a proportional voltage differential between the thermopile contacts.

platform, simplified experiments measuring amounts of enzyme were performed using CAT and hydrogen peroxide. Experiments were performed on the platform by first depositing a 10 nl volume of enzyme on to the area directly above the nanocalorimeter sensing junctions. Once the small volume was dried, the lid was added to form the microfluidic channel and the platform was connected to the electrical amplifier. 650 nl of substrate was placed at the entrance to the microfluidic channel and drawn in by capillary force, filling the entire channel. This filling created a large signal artifact lasting approximately 100 milliseconds, obscuring any signal during that time. The reaction began when the

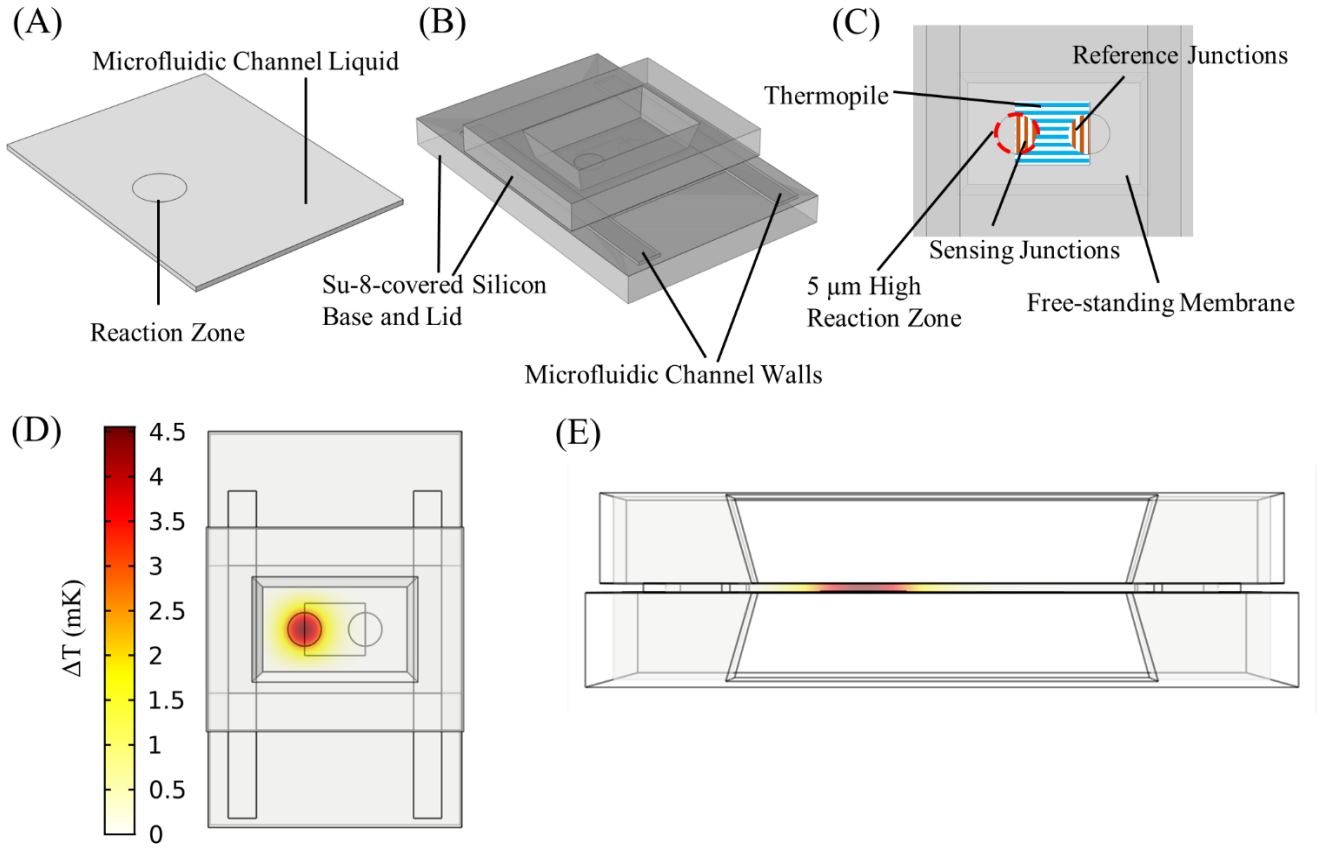

Figure 2. 3D calorimeter platform model constructed in COMSOL Multiphysics. (A) The microfluidic channel liquid is represented in the model by a block designated as water for physical and thermal properties and assigned an initial homogeneous substrate concentration. (B) The nanocalorimeter platform, consisting of the base, lid, walls, and membrane containing the calorimeter thermopiles, was added to the microfluidic channel liquid. (C) The sensing and reference junctions are simplified to uniform half circles that average the temperature differences between them. The Bi/Ti thermopile tracks between the junctions are modeled in the volume between the two half-circles. Top-down (D) and cross-section (E) spatial distribution of heat at 0.43 seconds, at which temperature difference between the reference and sensing junctions was the greatest.

substrate reconstitutes the dried enzyme, producing heat in the reaction volume above the sensing junctions.

Model Construction

To model TELISA performed on the platform, a 3D model was constructed in COMSOL Multiphysics. Figure 2A shows the model representation of the sample liquid within the microfluidic channel consisting of a block 2355 μm wide by 3000 μm long by 50 μm tall. A cylindrical volume of diameter 500 μm and height 5 μm in the channel liquid is designated as the reaction zone, where the enzymatic reaction governed by Michaelis-Menten kinetics occurs. The microfluidic channel liquid and reaction zone was defined as water to properly simulate the diffusion of substrate and enzyme, as well as heat capacity and thermal conductivity to compute temperature profiles. The 3D model was then extended to include the calorimeter platform (Figure 2B) and assigned material-related thermal conductivities G_i, taken from our previous modeling effort, to simulate the calorimeter platform's thermal response to the heat input from the enzymatic reaction [10]. The liquid channel was confined by the two thin Su-8 membranes and the two Su-8 channel walls with thermal conductance G_{mem}, and the sensing thermocouple junctions were embedded within the membrane. The sensing and reference junction areas were simplified as cylinders within the membrane with effective thermal conductance G_{junct}, and the thermopile tracks as a rectangular block between them with effective thermal conductance G_{therm}, as seen in Figure 2C. This can be done because the thermocouples within the differential thermopile calorimeter add temperature differences, but in a manner that makes a temperature difference at one pair of thermocouples indistinguishable from another in the generated signal. Due to the thermocouples' close proximities to each other and the high thermal conductivity of the aqueous environment above them, the sensing and reference junctions can each be simplified to uniform regions that average the temperature differences between them in an amplified voltage signal. The effective conductance G_{junct} and G_{therm} were determined by the proportional volumes of the

membrane, Bi, and Ti within the respective regions. The lid and base were designated as silicon and the membrane as Su-8 polymer for the material properties required to simulate heat flow through the platform. The portions of the membrane embedded with the nanocalorimeter were assigned their specific heat and thermal conductivity values for the respective ratios of Su-8, bismuth, and titanium within each volume.

Model Operation and Data Processing

Thermal ELISA reactions were simulated using the COMSOL Transport of a Diluted Species physics suite, which models the concentration field of a dilute solute in a solvent. The microfluidic channel liquid was assigned a homogeneous initial concentration of a substrate. A chemical reaction was assigned within the reaction volume, which reduced the substrate concentration over time as defined by the Michaelis-Menten kinetics of the enzyme to be simulated. CAT was explored. The simulation was run for 30 seconds, with the reaction beginning at t = 0.05 s to offset for the filling noise. In order to find the amount of substrate consumed by the reaction, the substrate was integrated across the microfluidic channel liquid and subtracted from the integral of the previous time point. This change in substrate per Δt was multiplied by the enthalpy of the decomposition of hydrogen peroxide to find the heat produced by the reaction and assigned as an energy source located within the reaction zone. Using the COMSOL Heat Transfer in Solids suite, the heat transfer through conduction, convection, and radiation was simulated, shown in Figure 2D. The differential temperature between the sensing and reference junctions was multiplied by the total calorimeter Seebeck coefficient to yield a predicted electrical output signal. The cross section in Figure 2E demonstrates that the 50 µm high microfluidic channel generates a large heat gradient from the reaction zone across the width of the channel, creating the temperature difference measured between the sensing and reference junctions. Thus, the refence junctions can be located within the same channel for differential calorimetry, instead of being thermally anchored to the silicon substrate. For a TELISA at a given substrate level, the model can be varied over

inputs of enzyme amount (Ea), enzyme turnover rate (kcat), and the inactivation factor (InF). The inactivation factor models the inactivation of catalase after $(InFx10^{7})^{-1}$ number of turnover events. The modeled signal y' was compared to experimental TELISA signal y by root mean square error (RMSE).

$$g(Ea, kcat, InF) = y'(n)$$

$$t = n * \Delta t$$

$$RMSE = \sqrt{\frac{\sum_1^n (y - y')^2}{n}}$$

Catalase Experiment

Bovine liver catalase was obtained from Fisher Scientific (2190015MU). All solutions were made using 1x PBS Buffer (Thermo Scientific 28348). Suspended CAT was allowed to dry over the sensing thermocouple junctions of the calorimeter, and the capillary channel was assembled. The channel was then filled with dilute H_2O_2 by placing a drop at the entrance of the channel and allowing capillary forces to draw the liquid in. The voltage of the thermopile was recorded over time. After a voltage peak the signal then formed a baseline dependent on the diffusion of substrate into the reaction zone, the reaction rate of the enzyme, and the active enzyme amount remaining after inactivation from past turnover events.

Results and Discussion

Enzyme-Based Model Operation

Diffusion modeling shown in Figure 3A shows the progression of substrate concentration within the microfluidic channel over the time course of the simulation. Beginning with a homogeneous concentration (a), the H_2O_2 within the reaction zone was consumed within the first second (b-f). The reaction then sharply slowed as substrate diffused into the reaction zone (g-k). The change in H_2O_2

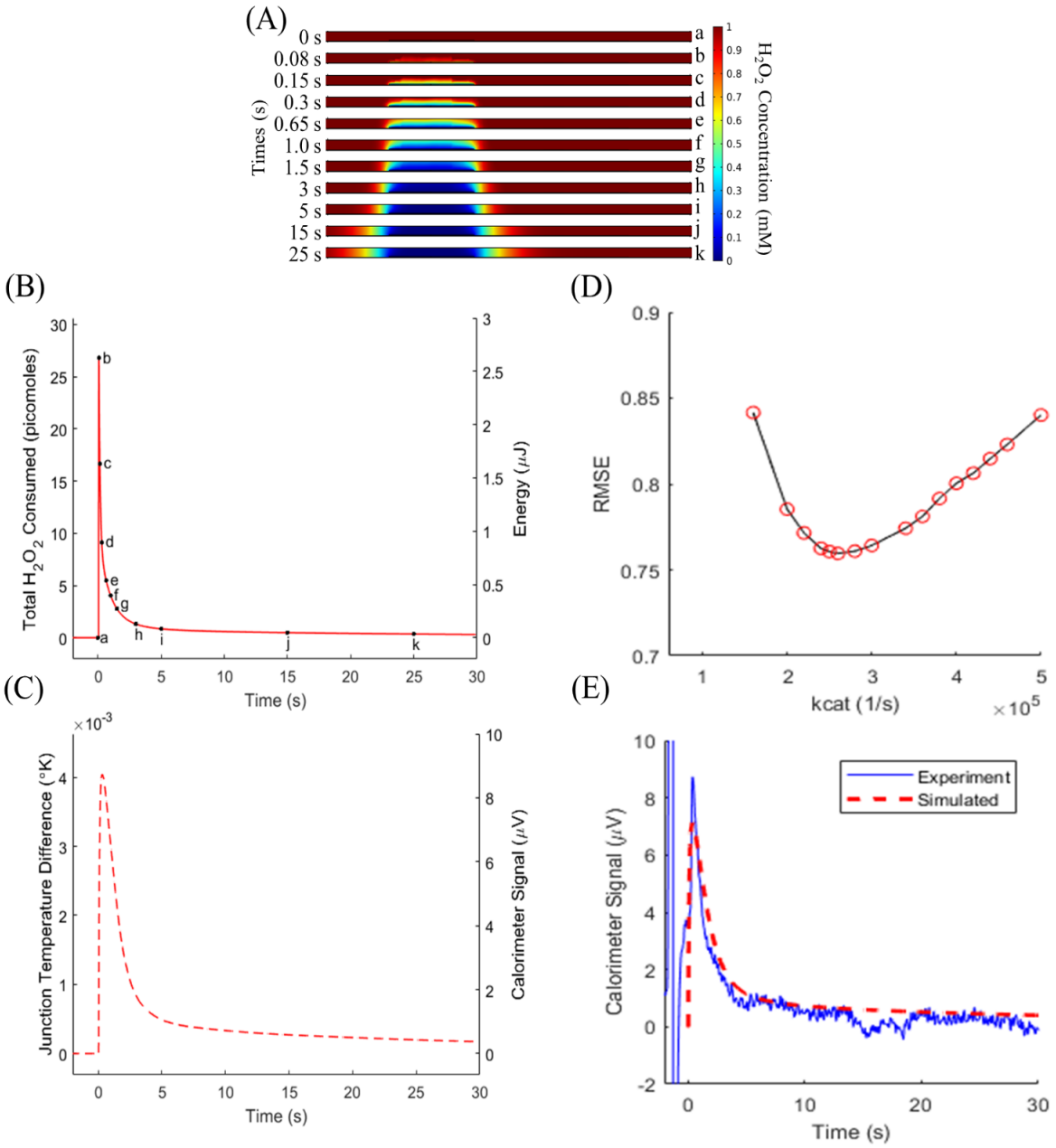

Figure 3. (A) Cross sections across the width of the microfluidic channel show the H_2O_2 depletion over time. (B) Total substrate consumed over time (left axis) was converted to the energy released within the reaction zone (right axis). A quick spike of heat was released (a-b), then quickly decreased as all initial substrate within the reaction zone was consumed (c-h). Substrate slowly diffused into the reaction zone and was quickly consumed, approaching a steady state (i-k). (C) Temperature difference between sensing and reference junctions (left axis) and predicted voltage generated by the thermopile during the reaction (right axis). (D) RMSE minimization found the best fit over the full 30 seconds of simulation, allowing for the enzyme parameter kcat determination. (E) Model and experiment comparison for 1 mM initial H_2O_2 and 10 femtomoles catalase. Results from the calorimeter response model (red dashed) closely match experimental (blue) data.

concentration was converted to the total substrate consumed (Figure 3B, left axis), and multiplied by the reaction enthalpy to find the energy produced by the reaction over time (Figure 3B, right axis). A

quick spike of heat was released (a-b), then quickly decreased as all initial substrate within the reaction zone was consumed (c-h). Substrate slowly diffused into the reaction zone and was quickly consumed, approaching a steady state (i-k). The energy curve was assigned as a heat source within the reaction volume, where it produced a change in temperature set by the specific heat of the liquid, which was treated as water due to the dilute nature of the H_2O_2 substrate. Heat diffusion through the connected membrane and surrounding liquid was simulated, governed by the assigned thermal conductivities. Figure 3C shows the temperature difference between the sensing and reference regions of the membrane (left axis), which was converted to a predicted calorimeter signal by multiplying by the Seebeck coefficient of the thermopile. With the inputs of substrate concentration, enzyme amount, and kcat, the model predicts the full time course of the reaction as measured by the nanocalorimeter platform.

Validation of Numerical Model

The model was first evaluated at a substrate concentration of 1 mM H_2O_2 to avoid enzyme inactivation effects. The enzyme amount of 10 fmol CAT quickly consumed the local substrate within the enzyme volume, then was limited by diffusion. In order to minimize the error between predicted and the experimentally-measured signals, the kcat value governing the rate of the CAT reaction was iterated over a range of values (Figure 3D). RMSE was minimized at a kcat value of 260,000 1/s. The temperature difference between sensing and reference junctions produced a simulated signal that closely followed the experimental signal (Figure 3E). This confirms the model has improved from previous iteration [10] to include enzyme kinetics, extending its utility from calorimeter sensitivity modeling to include enzyme-base assay design and model-assisted determination of assay results.

Model Adaptation at High Substrate Concentration

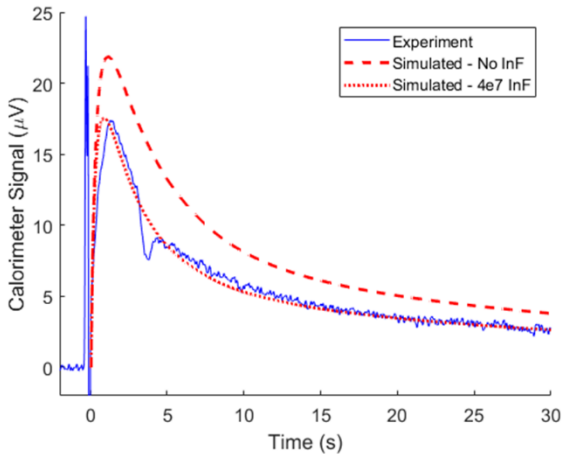

Figure 4. Time course of calorimeter output (blue) at substrate concentration of 10 mM H_2O_2 and simulated signals with (red dashed) and without (red dotted) enzyme deactivation.

Increased H_2O_2 increased the maximum rate of turnover, which produced a greater magnitude signal. This would increase the sensitivity of a TELISA performed on the nanocalorimeter platform. The effect lessens as the substrate concentration approaches the enzyme K_m constant, when the enzyme is saturated with substrate. This sets an upper limit of the K_m value of 93 mM H_2O_2 [12]. At substrate concentrations greater than 10 mM, the oxygen gas produced by the reaction formed bubbles within the reaction zone. These bubbles reduce and move the reaction zone away from the sensing junctions of the calorimeter and were impossible to model, so initial substrate concentrations were limited to 10 mM. CAT deactivates in the presence of high concentrations of H_2O_2 [13] and after approximately 10^7 turnover events [9]. By adding a component that reduced the amount of active enzyme proportionally to the change in substrate concentration (inactivation factor InF), model results improved in matching experiments using high H_2O_2 concentrations. As seen in Figure 4, TELISA with 10 mM H_2O_2 model and experimental results agreed with enzyme parameters of Km of 93 mM, kcat of $100x10^3$ 1/s, and deactivation after $4x10^7$ turnover events. We have observed loss of activity in CAT over time, and enzyme degradation is accelerated by a number of factors, so the change in kcat from previous runs was expected [14] [15].

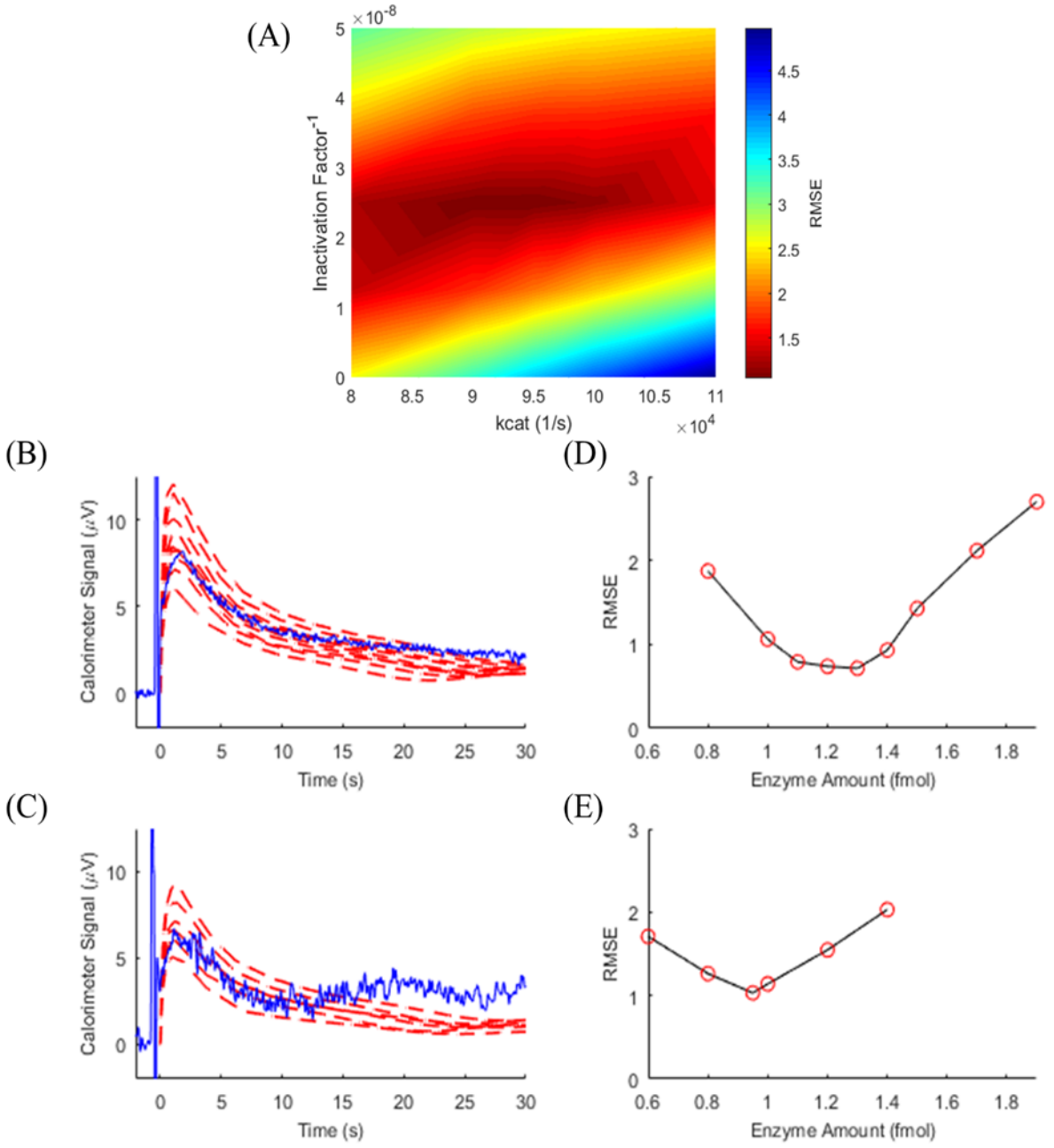

Figure 5. (A) RMSE surface for enzyme parameter calibration for TELISA. With 2.5 fmol of CAT and 10 mM H_2O_2 held constant, enzyme parameters kcat and InF were varied in model and compared to 30 seconds of the experimental signal to determine best fits for the conditions. These parameter values were then used for subsequent modelling to determine unknown enzyme amounts. Calorimeter output (blue) for TELISA with 10 mM H2O2 at 1.5 fmol (B) and 1.0 fmol (C) of CAT. Modeled signals (red dashed) were generated using kcat and InF values from the calibration step and enzyme amounts shown as a red circle in the corresponding figures (D) and (E). RMSE minimization from the simulated signals allow for the determination of the enzyme amount.

Model-Assisted TELISA

TELISA relies on knowing the reaction kinetics of the enzyme generating the heat-producing change. These characteristics can be determined by calibrating the reaction with a known enzyme

amount. CAT-based TELISA experiments were performed at 10 mM H_2O_2 substrate levels on multiple devices and days. In order to calibrate for differences in enzyme and platform performance, TELISA experimental results with the known amount of 2.5 fmol CAT were compared to model results iterated over ranges of kcat and InF values. RMSE was minimized, as seen in Figure 5A, and model-determined best fit kcat and InF values were then used to determine unknown Ea values for the subsequent TELISA experiments run on the same device and day. Over four discrete runs (n=4), minimized model RMSE (Figure 5B-E) returned 1.80±0.54 fmol for the 1.5 fmol experiments and 1.04±0.37 fmol for the 1 fmol experiments. We estimate the primary source in error to be related to experimental factors. The TELISA protocol required repeated deposition of exact volumes of enzyme, and pipette calibration showed an average error of 6.5%. This, combined with inaccuracies in weighing reagents and differences in placement location of the enzyme in relation to the calorimeter sensing junctions, all contributed to the error seen in the TELISA results.

Determining TELISA Limit of Detection

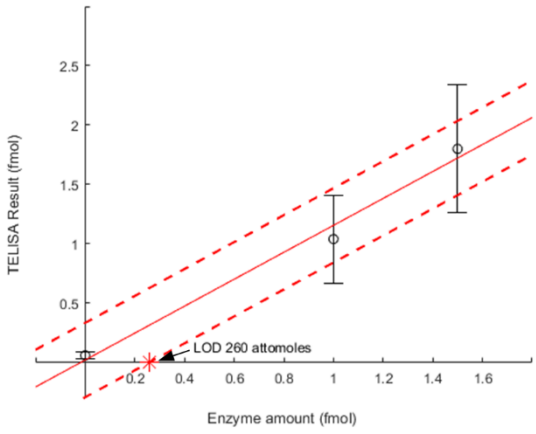

Figure 6. LOD for CAT-based TELISA on a nanocalorimeter platform. Experimental error determined using fixed substrate concentrations of 10 mM H_2O_2 and multiple experiments. The LOD of 260 attomoles of CAT was found where the average standard deviation (red dashed) of the model-assisted determination of the enzyme amount intersected with the x axis.

The LOD of the CAT-based TELISA at 10 mM substrate was calculated as the enzyme amount where the average standard deviation (Figure 6, dashed red line) of the model-assisted determination of the enzyme amount intersected with the x axis. At the intersection, the signal generated by the enzyme is dominated by background noise. The experimental LOD was found to be 260 attomoles. This is a considerable improvement over the 25 fmol acid-base neutralization LOD reported earlier [10]. Furthermore, this represents a significant

improvement on the 43.8 picomole LOD of the flow-through TELISA assay [8]**.** The improvement is due to the model assisted interpretation of a reaction occurring over time and enzyme calibration instead of phenomenological determination of either the signal peak or decay time constant [10] [11]. The calibration step accounted for changes in the enzyme activity at the times of the experiments. The majority of this error is experimental in nature, and unrelated to the device-based model calibration and determination. These mainly include volume and location inconsistencies when depositing the enzyme onto the nanocalorimeter platform. Enzyme diffusion out of the reaction zone was not considered by the model, which would reduce the calorimeter signal over time. Catalase diffuses much slower than H_2O_2 due to the relative molecular sizes, but this could have introduced error between the experimental and simulated signals since we are considering a longer reaction time course. Enzyme diffusion simulation can be added to the model, but future work plans to include enzyme immobilization to the sensing region surface to retain activity within the reaction zone and eliminate signal falloff [16]. The 10 mM substrate assay can be used from the LOD to a maximum of 3 femtomoles, when the reaction forms oxygen bubbles at the reaction site, affecting the heat signal. The range of the assay can be extended by reducing the substrate concentration, allowing for higher enzyme amounts to be probed. By using the model to investigate 30 seconds of data for enzyme amount determination, assay design was no longer limited to enzyme:substrate ratios that produce a large initial spike of signal. TELISA results were also adjusted for changing enzyme kinetics and platform conditions by determining enzyme kinetics as model inputs with a calibration experiment of a known amount of enzyme.

Conclusion

A finite element numerical model was constructed to compute the calorimeter response to an enzyme reaction. The simulated calorimeter signal closely follows experimental results for CAT. Determination of enzyme parameters through calibration is a necessary step to improve the robustness of the modeling and track changing enzyme kinetic characteristics. Model-assisted TELISA improves on

previous methods to determine label enzyme amounts on the calorimeter platform. Our high resolution nanocalorimeter platform, combined with modeling, demonstrates a limit of detection of 260 attomoles of CAT for a TELISA. Future work will focus on point-of-care applications for this adaptable TELISA platform, based on CAT or HRP as a reporter.

Acknowledgements

This work was supported by funding from Vanderbilt University. The authors would like to thank the Jansen Lab for lending computing resources, and Jeremy Ford and Wilson Adams for troubleshooting help.

References

[1] S. Premjeet, G. Deepika, B. Sudeep, J. Sonam, K. Sahil, R. Devashish and K. Sunil, "Enzyme-Linked Immuno-Sorbent Assay (ELISA), basics and it's application: a comprehensive review," Journal of Pharmacy Research, vol. 4, no. 12, pp. 4581-4583, 2011.

[2] A. Thiha and F. Ibrahim, "A Colorimetric Enzyme-Linked Immunosorbent Assay (ELISA) Detection Platform for a Point-of-Care Dengue Detection System on a Lab-on-Compact-Disc," Sensors, vol. 15, no. 5, pp. 11431-11441, 2015.

[3] B. Mattiasson, C. Borrebaeck, B. Sanfrindson and K. Mosbach, "Thermometric enzyme linked immunosorbent assay: TELISA," Biochimica et Biophysica Acta (BBA)-Enzymology, vol. 483, no. 2, pp. 221-227, 1977.

[4] B. Danielsson, "The enzyme thermistor," Applied Biochemistry and Biotechnology, vol. 7, no. 1, pp. 127-134, 1982.

[5] S. M. Tangutoo, V. L. Kopparthy, G. G. Nestorova and E. J. Guilbeau, "Dynamic thermoelectric glucose sensing with layer-by-layer glucose oxidase immobilization," Sensors and Actuators B: Chemical, Vols. 166-167, pp. 637-641, 2012.

[6] B. Lubbers and F. Baudenbacher, "Isothermal Titration Calorimetry in Nanoliter Droplets with Sub-Second Time Constants," Analytical Chemistry, vol. 83, no. 20, p. 7955, 2011.

[7] G. G. Nestorova, V. L. Kopparthy, N. D. Crews and E. J. Guilbeau, "Thermoelectric lab-on-a-chip ELISA," Analytical Methods, vol. 7, no. 5, pp. 2055-2063, 2015.

[8] N. Xu, J. Bai, Y. Peng, Z. Qie, Z. Liu, H. Tang, C. Liu, Z. Gao and B. Ning, "Pretreatment-free detection of diazepam in beverages based on a thermometric biosensor," Sensors and Actuators B: Chemical, vol. 241, pp. 504-512, 2017.

[9] M. Ghadermarzi and A. A. Moosavi-Movahedi, "Determination of the Kinetic Parameters for the “Suicide Substrate” Inactivation of Bovine Liver Catalase by Hydrogen Peroxide," Journal of Enzyme Inhibition, vol. 10, no. 3, pp. 167-175, 1996.

[10] E. Kazura, B. R. Lubbers, E. Dawson, J. A. Phillips and F. Baudenbacher, "Nano-Calorimetry based point of care biosensor for metabolic disease management," Biomedical Microdevices, vol. 19, no. 3, p. 50, 2017.

[11] B. Lubbers, E. Kazura, E. Dawson, R. Mernaugh and F. Baudenbacher, "Microfabricated calorimeters for thermometric enzyme linked immunosorbent assay in one-Nanoliter droplets," Biomedical Microdevices, vol. 21, no. 4, p. 85, 2019.

[12] J. Switala and P. C. Loewen, "Diversity of properties among catalases," Archives of Biochemistry and Biophysics, vol. 401, no. 2, pp. 145-154, 2002.

[13] H. Aebi, "Catalase in vitro," Methods in Enzymology, vol. 105, pp. 121-126, 1984.

[14] B. Hertwig, P. Streb and J. Feierabend, "Light Dependence of Catalase Synthesis and Degradation in Leaves and the Influence of Interfering Stress Conditions," Plant Physiology, vol. 100, no. 3, pp. 1547-1553, 1992.

[15] P. A. Prakash, U. Yogeswaran and S.-M. Chen, "A Review on Direct Electrochemistry of Catalase for Electrochemical Sensors," Sensors, vol. 9, no. 3, pp. 1821-1844, 2009.

[16] A. G. Grigoras, "Catalase immobilization—A review," Biochemical Engineering Journal, vol. 117, no. B, pp. 1-20, 2017.

Chapter V: Nanocalorimeter-Based Adaptable Point of Care Biosensor Platform[4]

By:

Evan Kazura, Ray Mernaugh, and Franz Baudenbacher

Chapter V bridges the gap between the nanocalorimeter platform described in Chapters II-IV and implementing a point-of-care biosensor. Even with the perfusion of the microfluidic channel powered by capillary forces, the capillary calorimeter platform fell short of point-of-care operation. Volume control requirements were reduced to nanoliters from picoliters, but volumetric and spatial precision when depositing enzyme remained essential to experimental results. Filling the channel produced a large filling artifact, large positive and negative signal swings that obscured the first 500 ms of experimental signal. Finally, the reaction was still limited by small volume of deposition or capture of the reactive enzymes. In order to simplify fluid handling during the operation of the capillary calorimeter, we developed a new method for delivering the sample liquid to the reaction zone within the microfluidic channel. By wicking liquid out of the microfluidic channel by paper capillary forces, new sample could be brought to the calorimeter sensing area after the channel had been filled. This allows for multistep assays to be performed on the platform with continuous temperature monitoring. Because the channel defines the volume of liquid, water and substrate volumes can be pipetted by hand instead of being dispensed using a high-precision instrument, such as a Picospritzer II. The filling artifact was reduced in magnitude, but it was not determined exactly what causes it. In order to advance the POC adaptation and increase the sensitivity of the assay, we developed a method of localizing the labelling enzyme to the sensing junction during setup and operation using magnetic beads to bind to the target

[4] In preparation.

analyte in larger sample volumes, which are then captured on the bottom surface of the microfluidic channel with a stationary conical rare earth neodymium magnet.

Abstract

Point-of-care diagnostics is an important field of biomedical research, delivering rapid results in nonlaboratory settings. Common tests are made faster to run and without trained technicians and expensive, large, or rare equipment. Our previous work has advanced towards a calorimeter-based biosensor platform adaptable for biomedical applications in a POC format. Detailed here is adaptation of the capillary-powered calorimeter platform for operation as a configurable POC biosensor. We developed a technique to perform multi-reagent assays powered solely by capillary forces by wicking reagents into a microfluidic channel using paper. The wicking technique also opens up the possibility for design of multi-step assays, including capture of target analytes on functionalized surfaces and wash steps, all with an assembled platform and the ability to monitor the calorimeter signal throughout. Advancing the POC operation of the platform, superparamagnetic beads were successfully captured on the surface of the microfluidic channel. Magnetic bead delivery of the enzyme catalyzing the signal-producing reaction eliminated prohibitively precise liquid volume and placement controls. Successful delivery of a target, such as a reporter enzyme, to the calorimeter using micron sized beads is a significant leap in the application of the platform as a POC tool. The result is a highly adaptable nanocalorimeter based platform for POC biomedical assays.

Introduction

Point-of-care (POC) diagnostics, an important field of biomedical research, deliver rapid results in nonlaboratory settings. Common tests are made faster to run and without trained technicians and expensive, large, or rare equipment [1]. POC diagnostics represented a worldwide market of over $15.5 billion in 2013, and improved connectivity has only increased its potential [2] [3]. The largest segment is

blood glucose monitoring, which allows patients to monitor and regulate blood glucose levels anywhere [4] [5]. User-friendly, portable, efficient, and inexpensive devices are needed for rapid diagnostic applications in a range of fields, including rapid disease diagnosis, chronic condition monitoring, environmental monitoring, and food safety [1] [6].

Biosensors are the basis for most POC diagnostic technologies. Biosensors are devices that incorporate biological systems to detect and quantify chemicals. The most commonly used biological systems are antibodies or enzymes, which are used to interact with the target analytes. An enzymatic reaction with the analyte of interest produces a quantifiable signal transduced by one of several different methods, including electrochemical, optical, or calorimetric [7] [8] [9]. Calorimeters directly measure the heat produced by the enzymatic reaction, eliminating the need for secondary or labeling transductions as most optical methods do [10]. The most commonly used enzymes produce heat of reactions in the range of 20-300 kJ/mol substrate, making for easy adaptation for sensing by calorimeters [11]. Calorimetric biosensors of the past measured clinically-relevant levels of cholesterol, urea, lactate, and glucose in blood samples, but relied on flow-through columns and required large sample volumes (>0.5 ml), temperature controls, complex pumping systems, and were only suited to the laboratory setting [12] [13] [7] [14]. Advances in chip calorimetry miniaturize the calorimetry process, reducing sample consumption and device time constants and pushing minimum detectable energies to the nJ range [15] [16] [17]. A few calorimetric biosensors suited to POC have been developed, but either fall short of easy nonlaboratory operation through requiring off-chip fluid handling, power sources, or ambient temperature controls, or have assay sensitivities below clinically relevant levels of the target analyte [18] [19] [20].

Our previous work has advanced towards a calorimeter-based biosensor platform adaptable for biomedical applications in a POC format. A differential thermopile calorimeter on a thin membrane was

designed with an open free-standing drop for nanoliter reaction volumes [21]. The therapeutic antibody trastuzumab was quantified in human serum by a highly sensitive sandwich thermometric enzyme-linked immunosorbent assay (TELISA) with a limit of detection better than physiological levels. However, picoliter-precise volume control of the reagents was required, and the reaction chamber needed to be sealed in order to stabilize the sample drop long enough to perform the reaction. Assay sensitivity was limited by the small area available above the calorimeter sensor junctions for surface functionalization, capping the amount of capturable target. Reagent injection also increased drop volume and evaporation slowly decreased it over time, causing a signal baseline shift which required signal post-processing adjustment for removal. A redesigned platform replaced the free-standing drop with a microfluidic channel, sacrificing increased heat flux away from the sensing area for elimination of noise from evaporation [22]. The calorimeter reference junctions were also moved to within the channel, allowing for the elimination of common mode noise and unwanted sources of heat, such as from dissolution. The liquid substrate was drawn into microfluidic channel by capillary forces, reducing volume control requirements from picoliters to nanoliters. However, volumetric and spatial precision when depositing enzyme remained essential to experimental results. Additionally, filling the channel produced a large filling artifact, large positive and negative signal swings that obscured the first 500 ms of experimental signal, and the reaction was still limited by the small volume of deposition for the reactive enzyme.

Detailed here is adaptation of the capillary-powered channel calorimeter platform for operation as an adaptable POC biosensor. A filter paper wick creates capillary-powered fluidics with no external pumps that can deliver different substrates to the calorimeter in series. We also demonstrate magnetic bead capture at the calorimeter sensing junctions, eliminating strict volume controls for reagent delivery and allowing for hand pipetting of all liquids. For the first time, a POC highly sensitive TELISA is possible through delivery of the target analyte by functionalized magnetic beads, fluid handling powered entirely by capillary forces, and intuitive operation by hand pipetting of reagents.

Methods

The nanocalorimeter platform was constructed as described in Kazura, et al. using standard microfabrication techniques [22]. Phosphate buffered saline, 20x (PBS, cat. #28348) were ordered from Thermo Fisher Scientific and diluted down to 1x concentration. Streptavidin-coupled Dynabeads (2.8 µm diameter, cat. #65306) were obtained from Thermo Fisher Scientific. Rare earth magnets obtained from supermagnetman.com. The magnet was positioned with a micromanipulator but remained stationary during experiments.

Results and Discussion

Wicking Fluid Handling

We developed a technique to perform multi-reagent assays powered solely by capillary forces generated by a microfluidic channel and paper wicks. The nanocalorimeter was constructed on a thin Su-8 membrane and enveloped with another thin layer of Su-8. 50 µm-high Su-8 rectangular strips form walls, and a flat lid encloses the calorimeter sensing and reference areas in a microfluidic channel [22]. A small strip of filter paper was placed at one end of the channel, ensuring some part of the paper resided within the channel volume (figure 1A). A drop of liquid placed in contact with the other end of the microfluidic channel was drawn in by capillary forces (figure 1B), and the simple geometry produced consistent filling with no bubble formation. When the forward edge of the channel liquid reached the paper, it was immediately wicked out of the channel (figure 1C). The remaining volume of the drop was drawn in, until the surface tension forces at the entrance of the channel counteracted the wicking action, leaving the channel fully filled (figure 1D). Placing another liquid drop at the channel entrance broke the balance of the forces and resumed the wicking of the channel liquid out through the paper wick (figure 1E-F). This drew in the newly introduced liquid sample, replacing the channel volume (figure

1G). Two lids were used in the course of the wicking technique experiments. A glass lid allowed for visual monitoring of channel, but the slightly hydrophobic surface of the lid coupled with the very

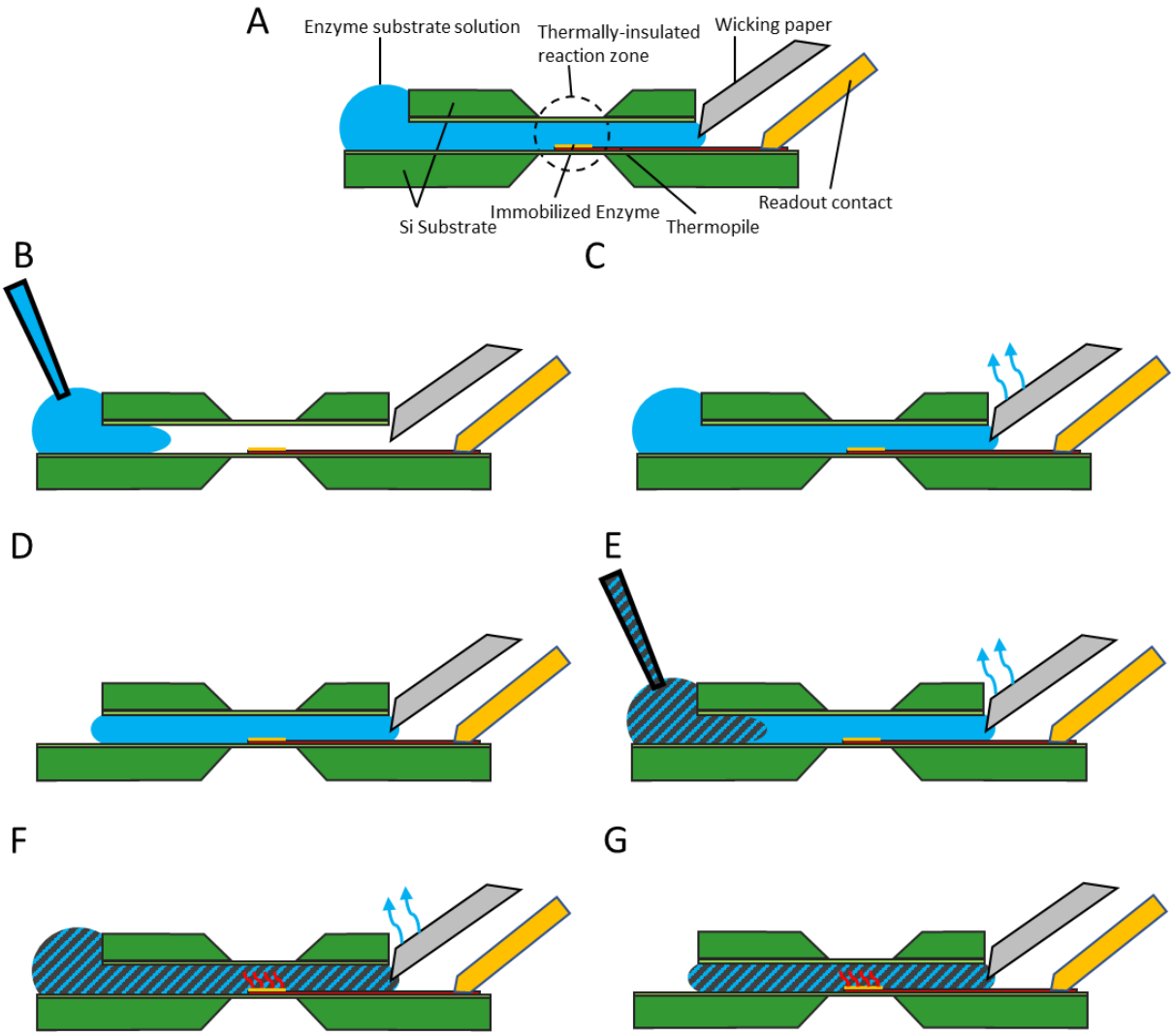

Figure 1. Diagram of paper wicking for multistep calorimetric assay. (A) Overview of the nanocalorimeter platform with perfused microfluidic channel. (B) A drop of liquid placed at the entrance to the microfluidic channel is quickly pulled in by capillary forces. (C) When the liquid reaches the paper wick, capillary forces pull liquid from the channel up the wick and drawing the remaining volume into the channel. (D) The surface tension forces at the entrance of the channel counteract the wicking action, leaving the channel fully filled. (E) A drop of reactive substrate is placed at the entrance of the channel, breaking the surface tension forces and restarting the wicking action. (F) The channel is completely perfused with the reactive substrate, beginning the heat-producing reaction at the surface of the nanocalorimeter. (G) Once the excess liquid is pulled into the channel, surface tension forces again halt the wicking, and the reaction continues in a stable fluidic environment.

hydrophobic rest of the Su-8-covered channel drew liquid in to fully fill the channel, but the liquid then retreated from the wick. Moving the edge of the liquid closer or over the sensing or reference areas affected the signal. The issue appeared to be solved by switching to the Su-8-coated silicon lids used

previously [22]. Oxygen plasma treatment of the Su-8 produced a hydrophilic surface at the top of the channel.

Previous experiments were limited in design to a single perfusion of the channel, as there was no way of exchanging the liquid within the microfluidic channel once it was filled without disassembling the platform. Under this mode of operation, the enzyme catalyzing the reaction needed to be present in the channel before perfusion, and therefore needed to be stable in a dry environment. Molecules of similar size but inert with regards to the reaction also needed to be placed at the reference area to mitigate the heat of dissolution from affecting the early reaction signal. With the wicking technique, the channel can be filled initially with a nonreactive liquid, such as PBS or water, to dissolve or wash the enzyme before the reaction begins. The wicking technique also opens up the possibility for design of multi-step assays, including capture of target analytes on functionalized surfaces and wash steps, all with an assembled platform and the ability to monitor the calorimeter signal throughout.

Introduction of liquid to the microfluidic channel caused a large, unpredictable swing in the calorimeter signal. This filling artifact masked any signal from the enzyme-based reaction for the first 500 ms after filling, preventing quick reactions from being quantified and reducing assay sensitivity. Wicking PBS into an already-filled channel produced a small but longer filling artifact (figure 2A). Heated (figure 2B) and cooled (figure 2C) PBS resulted in similar filling artifacts, ruling out temperature

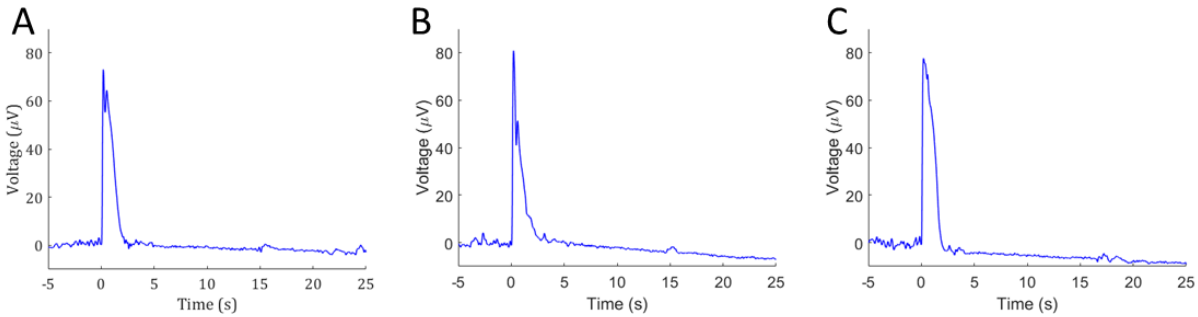

Figure 2. Filling artifact nanocalorimeter signals for drawing in of (A) PBS at room temperature of 25.4 °C, (B) PBS heated to 46.9 °C, and (C) PBS cooled to 17.9 °C.

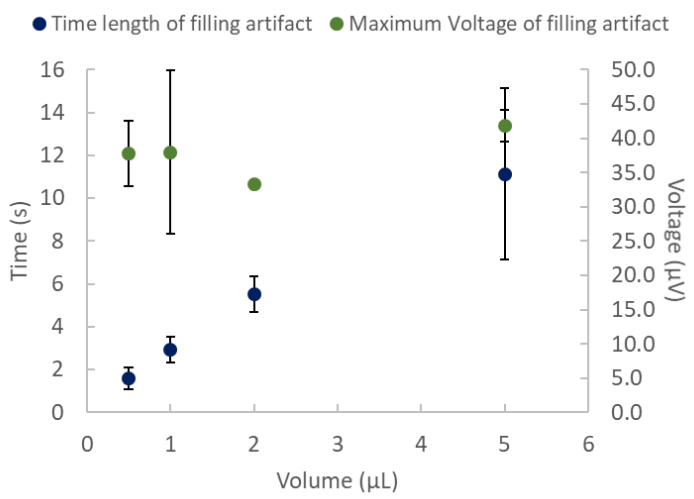

Figure 3. As the volume of the liquid drawn into the channel increases, the filling artifact occurs over a longer time (blue), while the amplitude of the signal remains unchanged (green).

differences between the liquid in the channel and the volume wicked in as the cause of the filling artifact signal. However, this also confirmed the robustness of the calorimeter to eliminate common mode noise. Wicking in a range of volumes (n = 3) once again showed similar maximum signal voltages for the filling artifacts, but extended time courses as the volumes increased (figure 3). This indicates the flowing of the ionic solution may lead to a voltage in the thermopile, but more testing is needed to confirm.

Magnetic bead delivery

Advancing the POC operation of the platform, magnetic bead delivery of the enzyme catalyzing the signal-producing reaction eliminated prohibitively precise liquid volume and placement controls. It was first determined whether magnetic beads could be captured using a stationary magnet positioned below the thin membrane of the platform. This would enable a sandwich TELISA to be

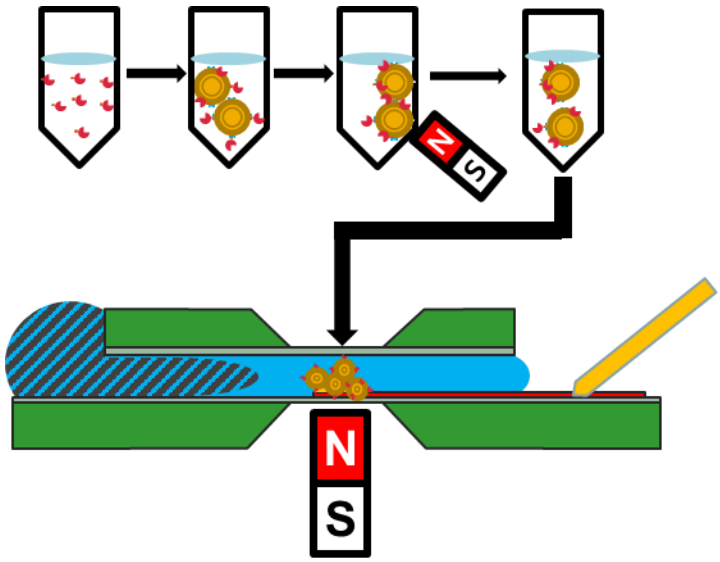

Figure 4. Diagram of POC enzyme-based assay with off-chip binding of enzyme label to magnetic beads, then capture to the calorimeter surface by a stationary magnet positioned below the thin membrane.

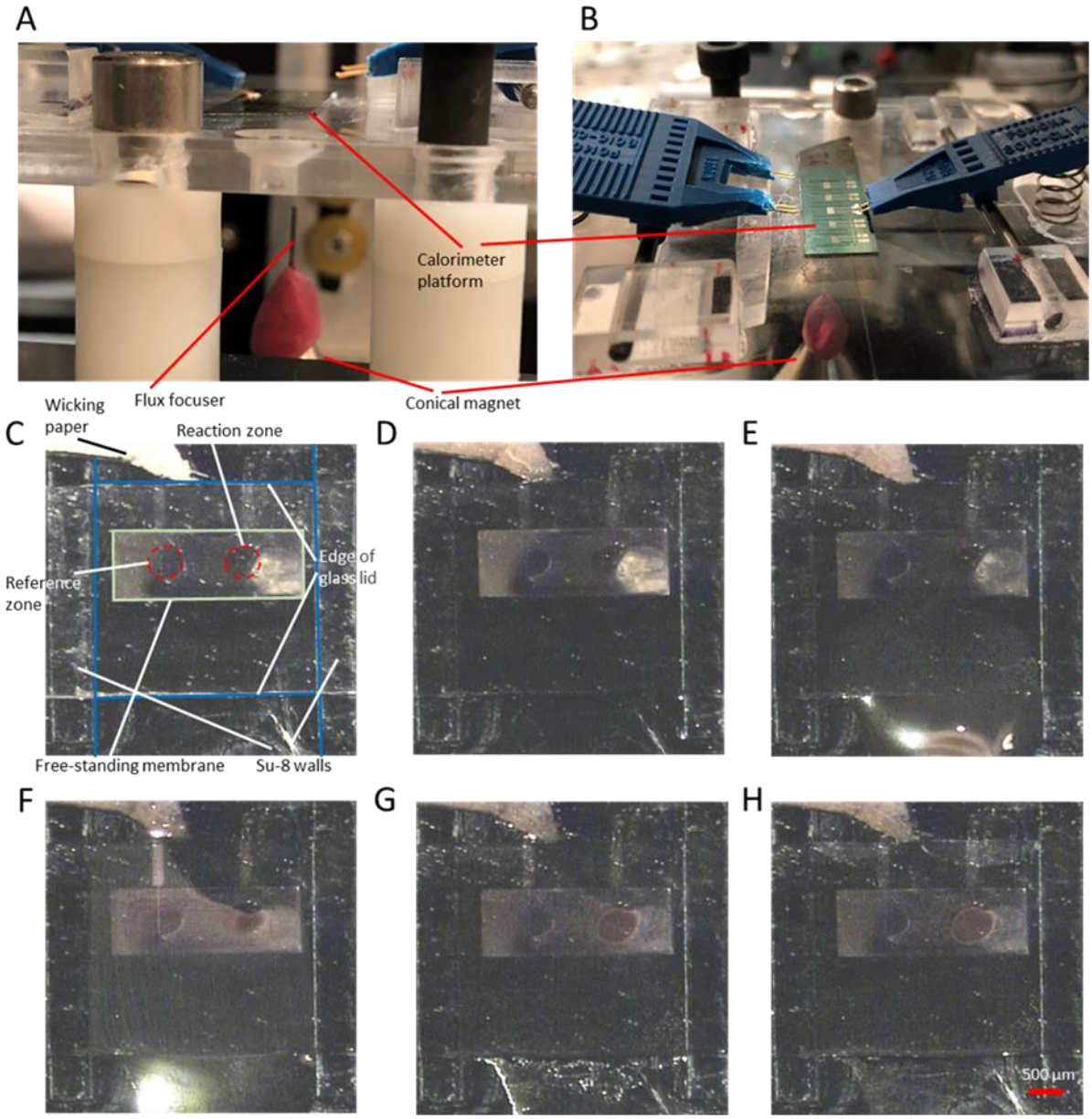

Figure 5. Capture of magnetic beads on channel perfusion. (A) Side and (B) top down of experimental setup. (C) Unfilled nanocalorimeter platform with glass lid and paper wick. (D) Microfluidic channel filled with PBS. (E) Drop with suspended magnetic beads placed at entrance of channel was pulled in by capillary forces. (F) Magnetic beads began collecting on channel floor above the flux focuser of the stationary magnet. (G) More beads collect, forming a reaction zone at the sensing junctions of the nanocalorimeter. (H) In a stable fluidic environment, the beads collect in a 600 µm diameter area.

performed on the platform (figure 4). The target analyte would be labelled by a functionalized enzyme, such as horseradish peroxidase, and captured by functionalized magnetic beads. The enzyme-target-bead complexes would be washed and condensed down, then delivered to the microfluidic channel to be captured above the calorimeter sensing junctions. A reactive substrate would be drawn into the

channel, producing a heat signal dependent on the amount of enzyme labeling the target analyte. The best results were achieved using a 25 mm diameter conical magnet with a 10 mm length of 46 SWG steel wire as a flux focuser positioned 100 µm below the bottom of the Su-8 membrane (figure 5A-B). Superparamagnetic beads were successfully captured on the surface of the microfluidic channel. In figure 5C, the beads suspended in solution can be seen entering the microfluidic channel as capillary forces draw the drop in. Figure

5D-G shows the beads begin collecting above flux focuser and condensing into a 600 µm diameter reaction zone above the sensing junction of the calorimeter. The stabilized channel (figure 5H) showed the bead capture was very effective in percentage collected and spatial aiming within the channel.

Successful delivery of a target, such as a reporter enzyme, to the calorimeter by bead is a significant leap in the application of the platform as a POC tool. The stationary magnet required no moving components once positioned, and positional aiming was just as accurate as placing enzyme by a picospritzer-powered micropipette spatially controlled by a micromanipulator. All reagents were hand-pipetted, moving assay operation away from requiring skilled technicians in specific laboratory setups. One of the primary limiting factors for the sensitivity of enzyme-based assays run on our platform has been the nanoliter volume restriction in the sample being investigated [22] [21]. While our calorimeter is one of the most sensitive, such small sample volumes translates to very small total amounts of target analytes being detected. By using the wicking method to flow through a bead-containing drop larger than the volume of the microfluidic channel, the total volume of target analyte was increased from nanoliters to a microliter. The bead-containing liquid exceeded the total volume of the channel but was captured to a much smaller area in the reaction zone by the magnetic forces. Further assay sensitivity increases are expected by expanding the interrogated sample volume by capturing target analytes off chip using functionalized beads in milliliter volumes, then concentrating down to a microliter for introduction to the microfluidic channel on the calorimeter platform.

Conclusion

Point-of-care diagnostics is an important field of biomedical research, delivering rapid results in nonlaboratory settings. In order to advance the POC adaptation and increase the sensitivity of our nanocalorimeter platform, we developed a method of localizing the labelling enzyme to the sensing junction using magnetic beads captured on the bottom surface of the microfluidic channel. A paper wick allowed for multiple perfusions of the microfluidic channel using capillary forces, opening up the possibility for design of multi-step assays. Future work will apply the highly adaptable nanocalorimeter-based biosensor towards a POC biomedical assay.

References

[1] M. Zarei, "Portable biosensing devices for point-of-care diagnostics: recent developments and applications," TrAC Trends in Analytical Chemistry, vol. 91, pp. 26-41, 2017.

[2] M. Elder, "Point of Care Diagnostics," BCC Research, 2014.

[3] S. Nayak, N. R. Blumenfeld, T. Laksanasopin and S. K. Sia, "Point-of-Care Diagnostics: Recent Developments in a Connected Age," Analytical Chemistry, vol. 89, no. 1, pp. 102-123, 2017.

[4] L. Ben Mohammadi, T. Klotzbuecher, S. Sigloch, K. Welzel, M. Goeddel, T. R. Pieber and L. Schaupp, "Clinical performance of a low cost near infrared sensor for continuous glucose monitoring applied with subcutaneous microdialysis," Biomedical Microdevices, vol. 17, no. 4, 2015.

[5] A. Soni and S. K. Jha, "A paper strip based non-invasive glucose biosensor for salivary analysis," Biosensors and Bioelectronics, vol. 67, pp. 763-768, 2015.

[6] A. K. Yetisen, M. S. Akram and C. R. Lowe, "Paper-based microfluidic point-of-care diagnostic devices," Lab on a Chip, vol. 13, pp. 2210-2251, 2013.

[7] B. Danielsson, "The enzyme thermistor," Applied Biochemistry and Biotechnology, vol. 7, no. 1, pp. 127-134, 1982.

[8] M. Yakovleva, S. Bhand and B. Danielsson, "The enzyme thermistor—A realistic biosensor concept. A critical review," AnalyticaChimica Acta, vol. 766, pp. 1-12, 2013.

[9] K. Reder-Christ and G. Bendas, "Biosensor Applications in the Field of Antibiotic Research - A Review of Recent Developments," Sensors, vol. 11, no. 10, pp. 9450-9466, 2011.

[10] B. Danielsson, "Calorimetric biosensors," Journal of Biotechnology, vol. 15, no. 3, pp. 187-200, 1990.

[11] B. Lubbers, Nano-Calorimetry for Point of Care Diagnostics, Nashville, TN: PhD Thesis, Vanderbilt University, 2015.

[12] F. Lammers and T. Scheper, "Thermal Biosensors in Biotechnology," in Thermal Biosensors, Bioactivity, Bioaffinitty, Berlin Heidelberg, Springer, 1999, p. 35.

[13] B. Xie, K. Ramanathan and B. Danielsson, "Principles of Enzyme Thermistor Systems: Applications to Biomedical and Other Measurements," in Thermal Biosensors, Bioactivity, Bioaffinitty, Berlin Heidelberg, Springer, 1999, p. 1.

[14] F. Lammers and T. Scheper, "On-line monitoring of enzyme-catalyzed biotransformations with biosensors," Enzyme and Microbial Technology, vol. 20, no. 6, pp. 432-436, 1997.

[15] K. Verhaegen, J. Simaels, W. Van Driessche, K. Baert, W. Sansen, B. Puers, L. Hermans and R. Mertens, "A Biomedical Microphysiometer," Biomedical Microdevices, vol. 2, no. 2, pp. 93-98, 1999.
[16] W. Lee, W. Fon, B. W. Axelrod and M. L. Roukes, "High-sensitivity microfluidic calorimeters for biological and chemical applications," PNAS USA, vol. 106, no. 36, pp. 15225-15230, 2009.
[17] B. Lubbers and F. Baudenbacher, "Isothermal Titration Calorimetry in Nanoliter Droplets with Sub-Second Time Constants," Analytical Chemistry, vol. 83, no. 20, p. 7955, 2011.
[18] B. Davaji and C. H. Lee, "A paper-based calorimetric microfluidics platform for bio-chemical sensing," Biosensors and Bioelectronics, vol. 59, pp. 120-126, 2014.
[19] S. V. H. Lai and S. Tadigadapa, "Calorimetric sensing system for real-time urea and creatinine measurements," in Sensors, 2012 IEEE, Taipei, 2012.
[20] N. Inomata, L. Pan, Z. Wang, M. Kimura and T. Ono, "Vanadium oxide thermal microsensor integrated in a microfluidic chip for detecting cholesterol and glucose concentrations," Microsystem Technologies, vol. 23, pp. 2873-2879, 2017.
[21] B. Lubbers, E. Kazura, E. Dawson, R. Mernaugh and F. Baudenbacher, "Microfabricated calorimeters for thermometric enzyme linked immunosorbent assay in one-Nanoliter droplets," Biomedical Microdevices, vol. 21, no. 4, p. 85, 2019.
[22] E. Kazura, B. R. Lubbers, E. Dawson, J. A. Phillips and F. Baudenbacher, "Nano-Calorimetry based point of care biosensor for metabolic disease management," Biomedical Microdevices, vol. 19, no. 3, p. 50, 2017.

Chapter VI: Conclusions and Future Research

Summary of Findings

The goal of this dissertation has been the development of a nanocalorimeter platform and adaptation of techniques for point-of-care biomedical applications. We have shown that it is possible to achieve a minimum detectable power in the picowatt range and a time constant less than 100 ms for a differential thermopile calorimeter constructed on a thin polymer membrane with an open drop liquid sample configuration. Integration of a closed fluidic channel reduced performance by a factor of 3 but made it possible for platform adaptation for POC biomedical applications. Finite element numerical modeling helped optimize the design of the calorimeter platform and produced a novel way to quantify target analytes in a TELISA. By combining the capillary fluidics with magnetic bead capture to deliver the analyte to the reaction volume, the platform was adapted for POC use. The result is a calorimeter-based biosensor that requires no external power sources, ambient temperature controls, or fluidic pumps, and is adaptable for biomedical applications.

Towards Aim 1, we developed nanocalorimeter platform with capillary-driven fluid delivery. Chapter II described the design and production of highly sensitive differential thermopile calorimeters on a thin polymer membrane. Our optimized micromachined calorimeters had nL reaction volumes and a minimum detectable power of 375 $pW/Hz^{1/2}$. We demonstrated rapid quantification in a model system of trastuzumab, a humanized monoclonal antibody used in the treatment of HER2 overexpressing breast cancers, in human serum using a HER2 peptide mimetic. Trastuzumab concentration and the reaction time constant correlated well and were used to determine trastuzumab concentrations. The limit of detection for the TELISA was in µg/ml range of trastuzumab in human serum. TELISA allowed for a simple readout, reduction in assay time, sample and reagent volumes but suffered from still using glass

micropipettes and micromanipulators to perform the experiments. This impediment to ease-of-use meant these devices would be limited to only the research lab without significant improvements. In Chapter III, a new calorimeter platform was described using on-chip fluid handling powered by capillary forces, an enclosed microfluidic reaction channel, and a differential thermopile calorimeter that eliminates noise from evaporation. The capillary platform reduced the device performance by a factor of 3 from the drop platform, but still exceeded the next best microfluidic calorimeter. Both the sensing and reference junctions of the thermopile were located within the microfluidic channel, eliminating errors associated with sample evaporation and heat of dilution. We demonstrated device performance in a model assay using catalase, achieving a threshold for hydrogen peroxide quantification of 50 μM. The potential for our device as a POC blood test for metabolic diseases was shown through the quantification of phenylalanine (Phe) in serum, an unmet necessary service in the management of Phenylketonuria (PKU). Pegylated phenylalanine ammonia-lyase (PEG-PAL) was utilized to react with Phe, but reliable detection was limited to < 5mM due to low enzymatic activity.

Towards Aim 2, we determined sensitivity on the calorimeter platform through finite element numerical modeling. Chapter IV tied the time course of the full enzyme reaction to the enzyme amount, creating a novel method of assaying target analytes labeled with enzyme. This method improved the quantitative nature of the enzyme-based assays run on our platform and their robustness to changing conditions. Using finite element numerical modeling, we simulated an enzyme-catalyzed reaction within the microfluidic channel of the capillary calorimeter platform, then converted the result to a heat profile, assigned it to the reaction zone within the microfluidic channel, and calculated a calorimeter signal based on the resulting temperature changes. This single comprehensive model interrogated the Michaelis-Menten governed enzyme kinetic reaction to determine the entire time course of the assay for the first time to extract the enzyme amount. Previously, results from the enzyme-based assays relied on phenomenological measurements to determine the results and were susceptible to error from

changing enzyme kinetics. The comprehensive model was used to calibrate for enzyme kinetics, and then simulate the entire time course of the reaction. The model-simulated signal closely followed the experimental signal after selecting for the enzyme turnover rate (kcat) and the inactivation factor (InF) using a known label enzyme amount (Ea). The experimental limit of detection for the catalase-based TELISA using 10 mM of substrate was calculated to be 260 attomoles. Determination of enzyme parameters through calibration is a necessary step to track changing enzyme kinetic characteristics and improves on previous methods to determine label enzyme amounts on the calorimeter platform. The results obtained using model-system signal analysis for calibration lead to significantly improved nanocalorimeter platform performance.

Towards Aim 3, we adapted the extraction of sample analyte and delivery to calorimeter for point-of-care biosensor operation. The work presented in Chapter V simplified reagent delivery to optimize the nanocalorimeter platform for point-of-care operation. Even with the perfusion of the microfluidic channel powered by capillary forces, the capillary calorimeter platform fell short of point-of-care operation. A paper wick at one entrance to the microfluidic channel drew excess liquid at the other end into the channel until counteracted by the surface tension forces present within the channel. Pulling fluid through the microfluidic channel using wicking paper reduced noise from the filling of the chamber and allowed for multistep assays to be developed. Volume control requirements were reduced to nanoliters from picoliters, but volumetric and spatial precision when depositing enzyme remained essential to experimental results. In order to advance the POC adaptation and increase the sensitivity of the assay, we developed a method of localizing the labelling enzyme to the sensing junction during setup and operation using magnetic beads to bind to the target analyte, which were then captured on the bottom surface of the microfluidic channel with a stationary conical rare earth neodymium magnet. Because the channel defined the volume of liquid, water and substrate volumes were pipetted by hand instead of being dispensed using a high-precision instrument, such as a Picospritzer II. While our

calorimeter is one of the most sensitive, such small sample volumes translated to very small total amounts of target analytes being detected. By using the wicking method to flow through a bead-containing drop larger than the volume of the microfluidic channel, the total volume of target analyte was increased from nanoliters to a microliter. The bead-containing liquid exceeded the total volume of the channel but was captured to a much smaller area in the reaction zone by the magnetic forces. Further assay sensitivity increases are expected by expanding the interrogated sample volume by capturing target analytes off chip using functionalized beads in milliliter volumes, then concentrating down to a microliter for introduction to the microfluidic channel on the calorimeter platform. For the first time, a POC highly sensitive TELISA is possible through delivery of the target analyte by functionalized magnetic beads, fluid handling powered entirely by capillary forces, and intuitive operation by hand pipetting of reagents.

Future Research

The next step in development of the platform is adapting a TELISA towards a biomedical application that would benefit from a POC assay. We used HRP in a sandwich TELISA in Chapter II, and will use that trastuzumab assay to test the effects of the model-assisted enzyme determination, the magnetic bead capture, and wicking microfluidics on the assay sensitivity and LOD. Now that the modeling and proof of concept experiments have given us a full understanding of the TELISA signal, we will seek out an established clinical assay to compare our POC approach to. One potential option arises from our work with trastuzumab, which can increase risk of a myocardial infarction (MI) during treatment for breast cancer. Elevated serum levels of the protein cardiac troponin I (cTnI) is an indicator of myocardial necrosis that occurs during an MI, and its specificity makes it a key diagnostic biomarker. Faster, more sensitive testing would aid doctors in diagnosing MI and directing treatment as quickly as possible, before traditional ECG-based symptoms showed. A sandwich TELISA with HRP-label has great

potential for detection of cTnI in serum, and we believe would be competitive with the gold standard tests available today.

Appendix A: COMSOL-generated MATLAB Code for Finite Element Numerical Model

```
function out = model
%
% CapCal_Combined_MATLABcode_compact.m
%
% Model exported on Mar 16 2020, 10:59 by COMSOL 5.4.0.388.

import com.comsol.model.*
import com.comsol.model.util.*

model = ModelUtil.create('Model');

model.modelPath('E:\Evan');

model.label('CapCal_Combined_MATLABcode.mph');

model.param.set('chanvol', '((2355*10^-6)*(3000*10^-6)*(50*10^-6))[m^3]');
model.param.set('reactvol', 'pi*(5*10^-6)*(250*10^-6)^2[m^3]');
model.param.set('ReactEnth', '98000 [J/mol]');
model.param.set('c0', '1[mM]');
model.param.set('Ea', '2.5465e-6[mol/l]');
model.param.set('Km', '93[mmol/l]');
model.param.set('kcat', '212000[1/s]');
model.param.set('degredation_factor', '0.25');

model.component.create('comp1', false);

model.component('comp1').geom.create('geom1', 3);

model.component('comp1').mesh.create('mesh1');

model.component('comp1').geom('geom1').lengthUnit([native2unicode(hex2dec({'00'
'b5'}), 'unicode') 'm']);
model.component('comp1').geom('geom1').create('blk3', 'Block');
model.component('comp1').geom('geom1').feature('blk3').label('Base Membrane');
model.component('comp1').geom('geom1').feature('blk3').set('pos', [-1900 -950 -1.5]);
model.component('comp1').geom('geom1').feature('blk3').set('size', [3800 1900 1.5]);
model.component('comp1').geom('geom1').create('blk10', 'Block');
model.component('comp1').geom('geom1').feature('blk10').label('Base Membrane 1');
model.component('comp1').geom('geom1').feature('blk10').set('pos', [-1900 -2950 -
1.5]);
model.component('comp1').geom('geom1').feature('blk10').set('size', [3800 2000 1.5]);
model.component('comp1').geom('geom1').create('blk11', 'Block');
model.component('comp1').geom('geom1').feature('blk11').label('Base Membrane 2');
model.component('comp1').geom('geom1').feature('blk11').set('pos', [-1900 950 -1.5]);
model.component('comp1').geom('geom1').feature('blk11').set('size', [3800 2000 1.5]);
model.component('comp1').geom('geom1').create('blk4', 'Block');
model.component('comp1').geom('geom1').feature('blk4').label('Membrane/Thermopiles
cutout');
model.component('comp1').geom('geom1').feature('blk4').set('pos', [-455 -390 -1.5]);
model.component('comp1').geom('geom1').feature('blk4').set('size', [910 780 1.5]);
model.component('comp1').geom('geom1').create('dif2', 'Difference');
model.component('comp1').geom('geom1').feature('dif2').label('Membrane');
model.component('comp1').geom('geom1').feature('dif2').selection('input').set({'blk3'}
);
```

```
model.component('comp1').geom('geom1').feature('dif2').selection('input2').set({'blk4'
});
model.component('comp1').geom('geom1').create('blk2', 'Block');
model.component('comp1').geom('geom1').feature('blk2').label('Membrane/Thermopiles');
model.component('comp1').geom('geom1').feature('blk2').set('pos', [-455 -390 -1.5]);
model.component('comp1').geom('geom1').feature('blk2').set('size', [910 780 1.5]);
model.component('comp1').geom('geom1').create('blk5', 'Block');
model.component('comp1').geom('geom1').feature('blk5').label('Left Channel Wall');
model.component('comp1').geom('geom1').feature('blk5').set('pos', [-1597.5 -2810 0]);
model.component('comp1').geom('geom1').feature('blk5').set('size', [420 4870 50]);
model.component('comp1').geom('geom1').create('blk6', 'Block');
model.component('comp1').geom('geom1').feature('blk6').label('Right Channel Wall');
model.component('comp1').geom('geom1').feature('blk6').set('pos', [1177.5 -2810 0]);
model.component('comp1').geom('geom1').feature('blk6').set('size', [420 4870 50]);
model.component('comp1').geom('geom1').create('blk7', 'Block');
model.component('comp1').geom('geom1').feature('blk7').label('Lid membrane');
model.component('comp1').geom('geom1').feature('blk7').set('pos', [-1900 -1500 50]);
model.component('comp1').geom('geom1').feature('blk7').set('size', [3800 3000 1.5]);
model.component('comp1').geom('geom1').create('blk8', 'Block');
model.component('comp1').geom('geom1').feature('blk8').label('Silicon Base');
model.component('comp1').geom('geom1').feature('blk8').set('pos', [-1900 -2950 -
501.5]);
model.component('comp1').geom('geom1').feature('blk8').set('size', [3800 5900 500]);
model.component('comp1').geom('geom1').create('hex1', 'Hexahedron');
model.component('comp1').geom('geom1').feature('hex1').label('Base Window');
model.component('comp1').geom('geom1').feature('hex1').set('p', [-1225 1225 1225 -1225
-1082.4 1082.4 1082.4 -1082.4; 775 775 -775 -775 632.4 632.4 -632.4 -632.4; -501.5 -
501.5 -501.5 -501.5 -1.5 -1.5 -1.5 -1.5]);
model.component('comp1').geom('geom1').create('dif3', 'Difference');
model.component('comp1').geom('geom1').feature('dif3').label('Base');
model.component('comp1').geom('geom1').feature('dif3').selection('input').set({'blk8'}
);
model.component('comp1').geom('geom1').feature('dif3').selection('input2').set({'hex1'
});
model.component('comp1').geom('geom1').create('hex2', 'Hexahedron');
model.component('comp1').geom('geom1').feature('hex2').label('Lid Window');
model.component('comp1').geom('geom1').feature('hex2').set('p', [-1225 1225 1225 -1225
-1082.4 1082.4 1082.4 -1082.4; 775 775 -775 -775 632.4 632.4 -632.4 -632.4; -501.5 -
501.5 -501.5 -501.5 -1.5 -1.5 -1.5 -1.5]);
model.component('comp1').geom('geom1').create('mir1', 'Mirror');
model.component('comp1').geom('geom1').feature('mir1').selection('input').set({'hex2'}
);
model.component('comp1').geom('geom1').create('mov1', 'Move');
model.component('comp1').geom('geom1').feature('mov1').set('displz', 50);
model.component('comp1').geom('geom1').feature('mov1').selection('input').set({'mir1'}
);
model.component('comp1').geom('geom1').create('blk9', 'Block');
model.component('comp1').geom('geom1').feature('blk9').label('Silicon Lid');
model.component('comp1').geom('geom1').feature('blk9').set('pos', [-1900 -1500 50]);
model.component('comp1').geom('geom1').feature('blk9').set('size', [3800 3000 500]);
model.component('comp1').geom('geom1').create('dif4', 'Difference');
model.component('comp1').geom('geom1').feature('dif4').label('Lid');
model.component('comp1').geom('geom1').feature('dif4').selection('input').set({'blk9'}
);
model.component('comp1').geom('geom1').feature('dif4').selection('input2').set({'mov1'
});
model.component('comp1').geom('geom1').create('blk1', 'Block');
model.component('comp1').geom('geom1').feature('blk1').label('Channel Liquid');
model.component('comp1').geom('geom1').feature('blk1').set('pos', {'-2355/2' '-1500'
'0'});
model.component('comp1').geom('geom1').feature('blk1').set('size', [2355 3000 50]);
model.component('comp1').geom('geom1').create('cyl1', 'Cylinder');
model.component('comp1').geom('geom1').feature('cyl1').label('Hot zone cutout');
```

```
model.component('comp1').geom('geom1').feature('cyl1').set('pos', [-455 0 0]);
model.component('comp1').geom('geom1').feature('cyl1').set('r', 250);
model.component('comp1').geom('geom1').feature('cyl1').set('h', 5);
model.component('comp1').geom('geom1').create('dif1', 'Difference');
model.component('comp1').geom('geom1').feature('dif1').selection('input').set({'blk1'}
);
model.component('comp1').geom('geom1').feature('dif1').selection('input2').set({'cyl1'
});
model.component('comp1').geom('geom1').create('cyl2', 'Cylinder');
model.component('comp1').geom('geom1').feature('cyl2').label('Hot zone');
model.component('comp1').geom('geom1').feature('cyl2').set('pos', [-455 0 0]);
model.component('comp1').geom('geom1').feature('cyl2').set('r', 250);
model.component('comp1').geom('geom1').feature('cyl2').set('h', 5);
model.component('comp1').geom('geom1').create('cyl3', 'Cylinder');
model.component('comp1').geom('geom1').feature('cyl3').label('Thermopile Hot
Junctions');
model.component('comp1').geom('geom1').feature('cyl3').set('pos', [-455 0 -1.5]);
model.component('comp1').geom('geom1').feature('cyl3').set('r', 250);
model.component('comp1').geom('geom1').feature('cyl3').set('h', 1.5);
model.component('comp1').geom('geom1').create('cyl4', 'Cylinder');
model.component('comp1').geom('geom1').feature('cyl4').label('Thermopile Cold
Junctions');
model.component('comp1').geom('geom1').feature('cyl4').set('pos', [455 0 -1.5]);
model.component('comp1').geom('geom1').feature('cyl4').set('r', 250);
model.component('comp1').geom('geom1').feature('cyl4').set('h', 1.5);
model.component('comp1').geom('geom1').run;
model.component('comp1').geom('geom1').run('fin');

model.component('comp1').variable.create('var1');
model.component('comp1').variable('var1').set('c_change', '((root.c0-
comp1.c)*root.chanvol)*(6.02e23[1/mol])');
model.component('comp1').variable('var1').set('Ea_new', 'Ea-
((c_change*root.degredation_factor*(10^-7)*6.02e-23)[mol]/reactvol)');
model.component('comp1').variable('var1').set('heatsource', '(-(d(comp1.c,
t))*chanvol*ReactEnth)*(t>0.05)');

model.component('comp1').material.create('mat2', 'Common');
model.component('comp1').material.create('mat3', 'Common');
model.component('comp1').material.create('mat4', 'Common');
model.component('comp1').material.create('mat5', 'Common');
model.component('comp1').material.create('mat6', 'Common');
model.component('comp1').material('mat2').selection.set([8 10]);
model.component('comp1').material('mat2').propertyGroup('def').func.create('eta',
'Piecewise');
model.component('comp1').material('mat2').propertyGroup('def').func.create('Cp',
'Piecewise');
model.component('comp1').material('mat2').propertyGroup('def').func.create('rho',
'Piecewise');
model.component('comp1').material('mat2').propertyGroup('def').func.create('k',
'Piecewise');
model.component('comp1').material('mat2').propertyGroup('def').func.create('cs',
'Interpolation');
model.component('comp1').material('mat3').selection.set([1 4]);
model.component('comp1').material('mat3').propertyGroup.create('Enu', 'Young''s
modulus and Poisson''s ratio');
model.component('comp1').material('mat3').propertyGroup.create('RefractiveIndex',
'Refractive index');
model.component('comp1').material('mat4').selection.set([2 3 5 6 7 9 14 15]);
model.component('comp1').material('mat5').selection.set([11]);
model.component('comp1').material('mat6').selection.set([12 13]);

model.component('comp1').common.create('amth_ht', 'AmbientThermalProperties');
```

```
model.component('comp1').physics.create('tds', 'DilutedSpecies', 'geom1');
model.component('comp1').physics('tds').create('init2', 'init', 3);
model.component('comp1').physics('tds').feature('init2').selection.set([8 10]);
model.component('comp1').physics('tds').create('reac1', 'Reactions', 3);
model.component('comp1').physics('tds').feature('reac1').selection.set([10]);
model.component('comp1').physics.create('ht', 'HeatTransfer', 'geom1');
model.component('comp1').physics('ht').create('fluid1', 'FluidHeatTransferModel', 3);
model.component('comp1').physics('ht').feature('fluid1').selection.set([8 10]);
model.component('comp1').physics('ht').create('hs1', 'HeatSource', 3);
model.component('comp1').physics('ht').feature('hs1').selection.set([10]);

model.component('comp1').mesh('mesh1').create('ftet2', 'FreeTet');
model.component('comp1').mesh('mesh1').create('ftet3', 'FreeTet');
model.component('comp1').mesh('mesh1').create('ftet4', 'FreeTet');
model.component('comp1').mesh('mesh1').create('ftet5', 'FreeTet');
model.component('comp1').mesh('mesh1').feature('ftet2').selection.geom('geom1', 3);
model.component('comp1').mesh('mesh1').feature('ftet2').selection.set([2 3 6]);
model.component('comp1').mesh('mesh1').feature('ftet2').create('size1', 'Size');
model.component('comp1').mesh('mesh1').feature('ftet3').selection.geom('geom1', 3);
model.component('comp1').mesh('mesh1').feature('ftet3').selection.set([9 10 11 12 13
14]);
model.component('comp1').mesh('mesh1').feature('ftet3').create('size1', 'Size');
model.component('comp1').mesh('mesh1').feature('ftet3').feature('size1').selection.set
([5 9 10 11 12 13 14]);
model.component('comp1').mesh('mesh1').feature('ftet4').selection.geom('geom1', 3);
model.component('comp1').mesh('mesh1').feature('ftet4').selection.set([1 4]);
model.component('comp1').mesh('mesh1').feature('ftet4').create('size1', 'Size');
model.component('comp1').mesh('mesh1').feature('ftet5').selection.geom('geom1', 3);
model.component('comp1').mesh('mesh1').feature('ftet5').selection.set([7 8 15]);
model.component('comp1').mesh('mesh1').feature('ftet5').create('size1', 'Size');

model.component('comp1').probe.create('dom1', 'Domain');
model.component('comp1').probe('dom1').selection.set([8 10]);

model.capeopen.label('Thermodynamics Package');

model.component('comp1').view('view1').set('renderwireframe', true);
model.component('comp1').view('view1').set('showgrid', false);
model.component('comp1').view('view1').set('transparency', true);

model.component('comp1').material('mat2').label('Water');
model.component('comp1').material('mat2').set('family', 'water');
model.component('comp1').material('mat2').propertyGroup('def').func('eta').set('arg',
'T');
model.component('comp1').material('mat2').propertyGroup('def').func('eta').set('pieces
', {'273.15' '413.15' '1.3799566804-0.021224019151*T^1+1.3604562827E-4*T^2-
4.6454090319E-7*T^3+8.9042735735E-10*T^4-9.0790692686E-13*T^5+3.8457331488E-16*T^6';
'413.15' '553.75' '0.00401235783-2.10746715E-5*T^1+3.85772275E-8*T^2-2.39730284E-
11*T^3'});
model.component('comp1').material('mat2').propertyGroup('def').func('Cp').set('arg',
'T');
model.component('comp1').material('mat2').propertyGroup('def').func('Cp').set('pieces'
, {'273.15' '553.75' '12010.1471-80.4072879*T^1+0.309866854*T^2-5.38186884E-
4*T^3+3.62536437E-7*T^4'});
model.component('comp1').material('mat2').propertyGroup('def').func('rho').set('arg',
'T');
model.component('comp1').material('mat2').propertyGroup('def').func('rho').set('pieces
', {'273.15' '553.75' '838.466135+1.40050603*T^1-0.0030112376*T^2+3.71822313E-
7*T^3'});
model.component('comp1').material('mat2').propertyGroup('def').func('k').set('arg',
'T');
```

```
model.component('comp1').material('mat2').propertyGroup('def').func('k').set('pieces',
{'273.15' '553.75' '-0.869083936+0.00894880345*T^1-1.58366345E-5*T^2+7.97543259E-
9*T^3'});
model.component('comp1').material('mat2').propertyGroup('def').func('cs').set('table',
{'273' '1403';  ...
'278' '1427';  ...
'283' '1447';  ...
'293' '1481';  ...
'303' '1507';  ...
'313' '1526';  ...
'323' '1541';  ...
'333' '1552';  ...
'343' '1555';  ...
'353' '1555';  ...
'363' '1550';  ...
'373' '1543'});
model.component('comp1').material('mat2').propertyGroup('def').func('cs').set('interp'
, 'piecewisecubic');
model.component('comp1').material('mat2').propertyGroup('def').set('dynamicviscosity',
'eta(T[1/K])[Pa*s]');
model.component('comp1').material('mat2').propertyGroup('def').set('ratioofspecificchea
t', '1.0');
model.component('comp1').material('mat2').propertyGroup('def').set('electricconductivi
ty', {'5.5e-6[S/m]' '0' '0' '0' '5.5e-6[S/m]' '0' '0' '0' '5.5e-6[S/m]'});
model.component('comp1').material('mat2').propertyGroup('def').set('heatcapacity',
'Cp(T[1/K])[J/(kg*K)]');
model.component('comp1').material('mat2').propertyGroup('def').set('density',
'rho(T[1/K])[kg/m^3]');
model.component('comp1').material('mat2').propertyGroup('def').set('thermalconductivit
y', {'k(T[1/K])[W/(m*K)]' '0' '0' '0' 'k(T[1/K])[W/(m*K)]' '0' '0' '0'
'k(T[1/K])[W/(m*K)]'});
model.component('comp1').material('mat2').propertyGroup('def').set('soundspeed',
'cs(T[1/K])[m/s]');
model.component('comp1').material('mat2').propertyGroup('def').addInput('temperature')
;
model.component('comp1').material('mat3').label('Silicon');
model.component('comp1').material('mat3').set('family', 'custom');
model.component('comp1').material('mat3').set('specular', 'custom');
model.component('comp1').material('mat3').set('customspecular', [0.7843137254901961 1
1]);
model.component('comp1').material('mat3').set('diffuse', 'custom');
model.component('comp1').material('mat3').set('customdiffuse', [0.6666666666666666
0.6666666666666666 0.7058823529411765]);
model.component('comp1').material('mat3').set('ambient', 'custom');
model.component('comp1').material('mat3').set('customambient', [0.6666666666666666
0.6666666666666666 0.7058823529411765]);
model.component('comp1').material('mat3').set('noise', true);
model.component('comp1').material('mat3').set('noisefreq', 1);
model.component('comp1').material('mat3').set('lighting', 'cooktorrance');
model.component('comp1').material('mat3').set('fresnel', 0.7);
model.component('comp1').material('mat3').set('roughness', 0.5);
model.component('comp1').material('mat3').propertyGroup('def').set('relpermeability',
{'1' '0' '0' '0' '1' '0' '0' '0' '1'});
model.component('comp1').material('mat3').propertyGroup('def').set('electricconductivi
ty', {'1e-12[S/m]' '0' '0' '0' '1e-12[S/m]' '0' '0' '0' '1e-12[S/m]'});
model.component('comp1').material('mat3').propertyGroup('def').set('thermalexpansionco
efficient', {'2.6e-6[1/K]' '0' '0' '0' '2.6e-6[1/K]' '0' '0' '0' '2.6e-6[1/K]'});
model.component('comp1').material('mat3').propertyGroup('def').set('heatcapacity',
'700[J/(kg*K)]');
model.component('comp1').material('mat3').propertyGroup('def').set('relpermittivity',
{'11.7' '0' '0' '0' '11.7' '0' '0' '0' '11.7'});
model.component('comp1').material('mat3').propertyGroup('def').set('density',
'2329[kg/m^3]');
```

```
model.component('comp1').material('mat3').propertyGroup('def').set('thermalconductivit
y', {'130[W/(m*K)]' '0' '0' '0' '130[W/(m*K)]' '0' '0' '0' '130[W/(m*K)]'});
model.component('comp1').material('mat3').propertyGroup('Enu').set('youngsmodulus',
'170e9[Pa]');
model.component('comp1').material('mat3').propertyGroup('Enu').set('poissonsratio',
'0.28');
model.component('comp1').material('mat3').propertyGroup('RefractiveIndex').set('n',
'');
model.component('comp1').material('mat3').propertyGroup('RefractiveIndex').set('ki',
'');
model.component('comp1').material('mat3').propertyGroup('RefractiveIndex').set('n',
{'3.48' '0' '0' '0' '3.48' '0' '0' '0' '3.48'});
model.component('comp1').material('mat3').propertyGroup('RefractiveIndex').set('ki',
{'0' '0' '0' '0' '0' '0' '0' '0' '0'});
model.component('comp1').material('mat4').label('Su8');
model.component('comp1').material('mat4').propertyGroup('def').set('thermalconductivit
y', {'0.2' '0' '0' '0' '0.2' '0' '0' '0' '0.2'});
model.component('comp1').material('mat4').propertyGroup('def').set('density', '1123');
model.component('comp1').material('mat4').propertyGroup('def').set('heatcapacity',
'1200');
model.component('comp1').material('mat5').label('Su8/Ti/Bi Tracks');
model.component('comp1').material('mat5').propertyGroup('def').set('thermalconductivit
y', {'2.406' '0' '0' '0' '2.406' '0' '0' '0' '2.406'});
model.component('comp1').material('mat5').propertyGroup('def').set('density', '2346');
model.component('comp1').material('mat5').propertyGroup('def').set('heatcapacity',
'1034');
model.component('comp1').material('mat6').label('Su8/Ti/Bi Sensing');
model.component('comp1').material('mat6').propertyGroup('def').set('thermalconductivit
y', {'0.4607' '0' '0' '0' '0.4607' '0' '0' '0' '0.4607'});
model.component('comp1').material('mat6').propertyGroup('def').set('density', '1268');
model.component('comp1').material('mat6').propertyGroup('def').set('heatcapacity',
'1180');

model.component('comp1').common('amth_ht').label('Ambient Thermal Properties (ht)');
model.common('cminpt').label('Common model inputs 1');

model.component('comp1').physics('tds').prop('MassConsistentStabilization').set('glim_
mass', '(0.1[mol/m^3])/tds.helem');
model.component('comp1').physics('tds').prop('AdvancedSettings').set('BackCompState',
0);
model.component('comp1').physics('tds').feature('cdm1').set('DiffusionMaterialList',
'mat2');
model.component('comp1').physics('tds').feature('init1').set('initc', 'c0');
model.component('comp1').physics('tds').feature('init2').set('initc', 'c0');
model.component('comp1').physics('tds').feature('reac1').set('R_c', '-
(kcat*Ea_new*c)/(Km+c)*(t>0.05)');
model.component('comp1').physics('ht').prop('PhysicalModelProperty').set('BackCompStat
eT', 0);
model.component('comp1').physics('ht').prop('ConsistentStabilization').set('glim',
'(0.01[K])/ht.helem');
model.component('comp1').physics('ht').prop('RadiationSettings').set('opaque',
'ht.dfltopaque');
model.component('comp1').physics('ht').feature('hs1').set('Q0',
'(heatsource)/reactvol');

model.component('comp1').mesh('mesh1').feature('size').set('hauto', 4);
model.component('comp1').mesh('mesh1').feature('ftet2').feature('size1').set('hauto',
4);
model.component('comp1').mesh('mesh1').feature('ftet3').feature('size1').set('hauto',
2);
model.component('comp1').mesh('mesh1').feature('ftet4').feature('size1').set('hauto',
8);
model.component('comp1').mesh('mesh1').run;
```

```
model.component('comp1').probe('dom1').set('window', 'window1');

model.component('comp1').physics('tds').feature('cdm1').set('minput_temperature_src',
'userdef');
model.component('comp1').physics('ht').feature('solid1').set('minput_strainreferencete
mperature_src', 'userdef');

model.study.create('std1');
model.study('std1').create('param', 'Parametric');
model.study('std1').create('time', 'Transient');
model.study('std1').feature('time').set('activate', {'tds' 'on' 'ht' 'on'});

model.sol.create('sol1');
model.sol('sol1').study('std1');
model.sol('sol1').attach('std1');
model.sol('sol1').create('st1', 'StudyStep');
model.sol('sol1').create('v1', 'Variables');
model.sol('sol1').create('t1', 'Time');
model.sol('sol1').feature('t1').create('se1', 'Segregated');
model.sol('sol1').feature('t1').create('i1', 'Iterative');
model.sol('sol1').feature('t1').create('i2', 'Iterative');
model.sol('sol1').feature('t1').feature('se1').create('ss2', 'SegregatedStep');
model.sol('sol1').feature('t1').feature('se1').create('ss1', 'SegregatedStep');
model.sol('sol1').feature('t1').feature('se1').create('ll1', 'LowerLimit');
model.sol('sol1').feature('t1').feature('se1').feature.remove('ssDef');
model.sol('sol1').feature('t1').feature('i1').create('mg1', 'Multigrid');
model.sol('sol1').feature('t1').feature('i1').feature('mg1').feature('pr').create('so1
', 'SOR');
model.sol('sol1').feature('t1').feature('i1').feature('mg1').feature('po').create('so1
', 'SOR');
model.sol('sol1').feature('t1').feature('i1').feature('mg1').feature('cs').create('d1'
, 'Direct');
model.sol('sol1').feature('t1').feature('i2').create('mg1', 'Multigrid');
model.sol('sol1').feature('t1').feature('i2').feature('mg1').feature('pr').create('sl1
', 'SORLine');
model.sol('sol1').feature('t1').feature('i2').feature('mg1').feature('po').create('sl1
', 'SORLine');
model.sol('sol1').feature('t1').feature('i2').feature('mg1').feature('cs').create('d1'
, 'Direct');
model.sol('sol1').feature('t1').feature.remove('fcDef');
model.sol.create('sol2');
model.sol('sol2').study('std1');
model.sol('sol2').label('Parametric Solutions 1');

model.batch.create('p1', 'Parametric');
model.batch('p1').create('so1', 'Solutionseq');
model.batch('p1').study('std1');

model.result.dataset.create('dset3', 'Solution');
model.result.dataset.create('avh1', 'Average');
model.result.dataset('dset3').set('probetag', 'dom1');
model.result.dataset('avh1').set('probetag', 'dom1');
model.result.dataset('avh1').set('data', 'dset3');
model.result.dataset('avh1').selection.geom('geom1', 3);
model.result.dataset('avh1').selection.set([8 10]);
model.result.numerical.create('pev1', 'EvalPoint');
model.result.numerical.create('av1', 'AvVolume');
model.result.numerical.create('av2', 'AvVolume');
model.result.numerical.create('av3', 'AvVolume');
model.result.numerical('pev1').set('probetag', 'dom1');
model.result.numerical('av1').set('data', 'dset2');
model.result.numerical('av1').selection.set([12]);
```

```
model.result.numerical('av1').set('probetag', 'none');
model.result.numerical('av2').set('data', 'dset2');
model.result.numerical('av2').selection.set([13]);
model.result.numerical('av2').set('probetag', 'none');
model.result.numerical('av3').set('data', 'dset2');
model.result.numerical('av3').selection.set([8 10]);
model.result.numerical('av3').set('probetag', 'none');
model.result.create('pg5', 'PlotGroup1D');
model.result('pg5').create('glob1', 'Global');

model.component('comp1').probe('dom1').genResult([]);

model.study('std1').feature('param').set('sweeptype', 'filled');
model.study('std1').feature('param').set('pname', {'kcat' 'degredation_factor' 'Ea'});
model.study('std1').feature('param').set('plistarr', {'380000' '0' '(10e-
15)[mol]/reactvol'});
model.study('std1').feature('param').set('punit', {'1/s' '' 'mol/m^3'});
model.study('std1').feature('time').set('tlist', 'range(0,0.01,5) range(5.1,0.1,30)');
model.study('std1').feature('time').set('discretization', {'tds' 'physics' 'ht'
'physics'});

model.sol('sol1').attach('std1');
model.sol('sol1').feature('v1').set('resscalemethod', 'auto');
model.sol('sol1').feature('v1').set('clist', {'range(0,0.01,5) range(5.1,0.1,30)'
'0.03[s]'});
model.sol('sol1').feature('t1').set('tlist', 'range(0,0.01,5) range(5.1,0.1,30)');
model.sol('sol1').feature('t1').set('rtol', 0.005);
model.sol('sol1').feature('t1').set('atolglobalvaluemethod', 'manual');
model.sol('sol1').feature('t1').set('atolvaluemethod', {'comp1_c' 'manual' 'comp1_T'
'manual'});
model.sol('sol1').feature('t1').set('tstepsbdf', 'strict');
model.sol('sol1').feature('t1').set('maxorder', 2);
model.sol('sol1').feature('t1').set('estrat', 'exclude');
model.sol('sol1').feature('t1').feature('dDef').set('ooc', false);
model.sol('sol1').feature('t1').feature('dDef').set('rhob', 400);
model.sol('sol1').feature('t1').feature('se1').feature('ss2').set('linsolver', 'i2');
model.sol('sol1').feature('t1').feature('se1').feature('ss2').set('subdamp', 0.7);
model.sol('sol1').feature('t1').feature('se1').feature('ss1').label('Temperature T');
model.sol('sol1').feature('t1').feature('se1').feature('ss1').set('linsolver', 'i1');
model.sol('sol1').feature('t1').feature('se1').feature('ss1').set('subdamp', 0.7);
model.sol('sol1').feature('t1').feature('se1').feature('ll1').set('lowerlimit',
'comp1.T 0');
model.sol('sol1').feature('t1').feature('i1').set('rhob', 20);
model.sol('sol1').feature('t1').feature('i1').feature('mg1').feature('cs').feature('dD
ef').set('ooc', false);
model.sol('sol1').feature('t1').feature('i1').feature('mg1').feature('cs').feature('d1
').set('linsolver', 'pardiso');
model.sol('sol1').feature('t1').feature('i1').feature('mg1').feature('cs').feature('d1
').set('ooc', false);
model.sol('sol1').feature('t1').feature('i1').feature('mg1').feature('cs').feature('d1
').set('pardreorder', 'ndmt');
model.sol('sol1').feature('t1').feature('i2').set('maxlinit', 400);
model.sol('sol1').feature('t1').feature('i2').set('rhob', 40);
model.sol('sol1').feature('t1').feature('i2').feature('mg1').feature('pr').feature('sl
1').set('linerelax', 0.2);
model.sol('sol1').feature('t1').feature('i2').feature('mg1').feature('pr').feature('sl
1').set('relax', 0.4);
model.sol('sol1').feature('t1').feature('i2').feature('mg1').feature('po').feature('sl
1').set('linerelax', 0.2);
model.sol('sol1').feature('t1').feature('i2').feature('mg1').feature('po').feature('sl
1').set('seconditer', 2);
model.sol('sol1').feature('t1').feature('i2').feature('mg1').feature('po').feature('sl
1').set('relax', 0.4);
```

```
model.sol('sol1').feature('t1').feature('i2').feature('mg1').feature('cs').feature('dD
ef').set('ooc', false);
model.sol('sol1').feature('t1').feature('i2').feature('mg1').feature('cs').feature('d1
').set('linsolver', 'pardiso');
model.sol('sol1').feature('t1').feature('i2').feature('mg1').feature('cs').feature('d1
').set('ooc', false);
model.sol('sol1').feature('t1').feature('i2').feature('mg1').feature('cs').feature('d1
').set('pardreorder', 'ndmt');
model.sol('sol1').runAll;

model.batch('p1').set('control', 'param');
model.batch('p1').set('sweeptype', 'filled');
model.batch('p1').set('pname', {'kcat' 'degredation_factor' 'Ea'});
model.batch('p1').set('plistarr', {'380000' '0' '(10e-15)[mol]/reactvol'});
model.batch('p1').set('punit', {'1/s' '' 'mol/m^3'});
model.batch('p1').set('err', true);
model.batch('p1').feature('sol1').set('seq', 'sol1');
model.batch('p1').feature('sol1').set('psol', 'sol2');
model.batch('p1').feature('sol1').set('param',
{'"kcat","380000","degredation_factor","0","Ea","0.0101859163578813"'});
model.batch('p1').attach('std1');
model.batch('p1').run;

model.result.dataset('dset3').label('Probe Solution 3');
model.result.numerical('pev1').set('table', 'new');
model.result.numerical('av1').label('Hot Junctions');
model.result.numerical('av2').label('Cold Junctions');
model.result.numerical('av3').label('Concentration');
model.result.numerical('av3').set('expr', {'c'});
model.result.numerical('av3').set('unit', {'mol/m^3'});
model.result.numerical('av3').set('descr', {'Concentration'});
model.result('pg5').set('data', 'none');
model.result('pg5').feature('glob1').set('expr', {'comp1.ht.QInt'
'comp1.heatsource'});
model.result('pg5').feature('glob1').set('unit', {'W' 'W'});
model.result('pg5').feature('glob1').set('descr', {'Total heat source' ''});
model.result.remove('pg6');

out = model;
```

Appendix B: MATLAB Code

Calorimeter Platform Design Optimization

```
clear all;
close all;

M = csvread('HotJunctionsUpdated_10ChHt.csv');

T = M(:,1);
hot10um = M(:,2);

M = csvread('HotJunctionsUpdated_25ChHt.csv');
hot25um = M(:,2);
M = csvread('HotJunctionsUpdated_50ChHt.csv');
hot50um = M(:,2);
M = csvread('HotJunctionsUpdated_75ChHt.csv');
hot75um = M(:,2);
M = csvread('HotJunctionsUpdated_100ChHt.csv');
hot100um = M(:,2);
M = csvread('HotJunctionsUpdated_150ChHt.csv');
hot150um = M(:,2);
M = csvread('HotJunctionsUpdated_200ChHt.csv');
hot200um = M(:,2);
M = csvread('HotJunctionsUpdated_250ChHt.csv');
hot250um = M(:,2);
M = csvread('HotJunctionsUpdated_300ChHt.csv');
hot300um = M(:,2);
M = csvread('ColdJunctionsUpdated_10ChHt.csv');
cold10um = M(:,2);
M = csvread('ColdJunctionsUpdated_25ChHt.csv');
cold25um = M(:,2);
M = csvread('ColdJunctionsUpdated_50ChHt.csv');
cold50um = M(:,2);
M = csvread('ColdJunctionsUpdated_75ChHt.csv');
cold75um = M(:,2);
M = csvread('ColdJunctionsUpdated_100ChHt.csv');
cold100um = M(:,2);
M = csvread('ColdJunctionsUpdated_150ChHt.csv');
cold150um = M(:,2);
M = csvread('ColdJunctionsUpdated_200ChHt.csv');
cold200um = M(:,2);
M = csvread('ColdJunctionsUpdated_250ChHt.csv');
cold250um = M(:,2);
M = csvread('ColdJunctionsUpdated_300ChHt.csv');
cold300um = M(:,2);

diff10um = hot10um-cold10um;
diff25um = hot25um-cold25um;
diff50um = hot50um-cold50um;
diff75um = hot75um-cold75um;
diff100um = hot100um-cold100um;
diff150um = hot150um-cold150um;
diff200um = hot200um-cold200um;
diff250um = hot250um-cold250um;
diff300um = hot300um-cold300um;

figure(1)
```

```
plot(T,diff10um,'x',T,diff25um,'x',T,diff50um,'x',T,diff75um,'x',T,diff100um,'x',T,dif
f150um,'x',T,diff200um,'x',T,diff250um,'x',T,diff300um,'x')
hold on
title('Temperature Change in Thermopiles by Channel Height')
legend('10 um','25 um','50 um','75 um','100 um','150 um','200 um','250 um','300 um')
xlabel('Time (s)')
ylabel('Thermopile Change in Temp (K)')
grid on
hold off

f = 10; %sample frequency
n=length(T);
temp_time=zeros(9,1);
for k=1:n   %length to integrate peak
    q=(diff10um(k))*(1/f);
    temp_time(1)=temp_time(1)+q;
    q=(diff25um(k))*(1/f);
    temp_time(2)=temp_time(2)+q;
    q=(diff50um(k))*(1/f);
    temp_time(3)=temp_time(3)+q;
    q=(diff75um(k))*(1/f);
    temp_time(4)=temp_time(4)+q;
    q=(diff100um(k))*(1/f);
    temp_time(5)=temp_time(5)+q;
    q=(diff150um(k))*(1/f);
    temp_time(6)=temp_time(6)+q;
    q=(diff200um(k))*(1/f);
    temp_time(7)=temp_time(7)+q;
    q=(diff250um(k))*(1/f);
    temp_time(8)=temp_time(8)+q;
    q=(diff300um(k))*(1/f);
    temp_time(9)=temp_time(9)+q;
end
disp('Total Change in Temp (T*s)')
disp(temp_time)

heights = [10 25 50 75 100 150 200 250 300];
figure(2)
plot(heights,temp_time,'o')
title('Integrated Temperature Change in Thermopiles by Channel Height')
xlabel('Channel Height (um)')
ylabel('Thermopile Change in Temp (K)')
%axis([0 325 0 7*10^-5])

figure(3)
plot(heights(3:7),temp_time(3:7),'o')
title('Integrated Temperature Change in Thermopiles by Channel Height')
xlabel('Channel Height (um)')
ylabel('Thermopile Change in Temp (K)')
%axis([0 325 0 2*10^-5])

seebeck = 2160*10^-6; %total seebeck coefficient V/K
TotEn = 2.454*10^-9; %total energy J
Voltage_time = temp_time*seebeck;
Sensitivity = Voltage_time/TotEn
figure(4)
plot(heights,Sensitivity,'o')
title('Sensitivity by Channel Height')
xlabel('Channel Height (um)')
ylabel('Sensitivity (V/W)')
axis([0 325 0 60])

figure(5)
```

```
plot(heights(2:9),Sensitivity(2:9),'o')
%title('Sensitivity by Channel Height')
xlabel('Channel Height (um)','fontsize',16)
ylabel('Sensitivity (V/W)','fontsize',16)
axis([0 325 0 30])
```

Catalase Model-assisted TELISA

```
close all
clear all


%%%%%%%%%%%%%%%%%%%%%%%%%%%%%%%%%%%%%%%%%%%%%%%%%%%%%%%%%%%%%%%%%%%%%%%%%%%%%%%%%%%%%%%%%%%%%%%%%%%%%%%%%%%%%%%
%%%%%%%
%Run1 2.5fmol parameter selection

seebeck = 2160*10^-6; %total seebeck coefficient V/K

f=100;  %sampling frequency
Data1=dlmread('190119_0450_250nMCat_10mMH2O2_01.txt','\t');
TELISA_2pt5fmol_Run1=Data1(1956:5456,2);
TELISA_2pt5fmol_Run1=TELISA_2pt5fmol_Run1/10000*1e6;    %amp gain correction
N=length(TELISA_2pt5fmol_Run1);
X_2pt5fmol_Run1=1/f:1/f:N/f;
X_2pt5fmol_Run1 = (X_2pt5fmol_Run1-5);
preBaseline_2pt5fmol_Run1 = mean(TELISA_2pt5fmol_Run1(10:260));
TELISA_2pt5fmol_Run1 = TELISA_2pt5fmol_Run1-preBaseline_2pt5fmol_Run1;

M = csvread('190428_CombModel_EnzDeg_C10mM_E2pt5fmol_kcat100k_quarter_hot.csv');
M2 = csvread('190428_CombModel_EnzDeg_C10mM_E2pt5fmol_kcat100k_quarter_cold.csv');
T_comb = M(:,1);
hotC10mM_E2pt5fmol_kcat100k_EnzDegComb_quarter = M(:,2);
coldC10mM_E2pt5fmol_kcat100k_EnzDegComb_quarter = M2(:,2);

diffC10mM_E2pt5fmol_kcat100k_EnzDegComb_quarter =
hotC10mM_E2pt5fmol_kcat100k_EnzDegComb_quarter -
coldC10mM_E2pt5fmol_kcat100k_EnzDegComb_quarter;
calresponse_C10mM_E2pt5fmol_kcat100k_EnzDegComb_quarter =
diffC10mM_E2pt5fmol_kcat100k_EnzDegComb_quarter*seebeck;

M = csvread('190429_CombModel_rerun_EnzDeg_C10mM_E2pt5fmol_kcat100k_quarter_hot.csv');
M2 =
csvread('190429_CombModel_rerun_EnzDeg_C10mM_E2pt5fmol_kcat100k_quarter_cold.csv');
hotC10mM_E2pt5fmol_kcat100k_EnzDegComb_rerun_quarter = M(:,2);
coldC10mM_E2pt5fmol_kcat100k_EnzDegComb_rerun_quarter = M2(:,2);

diffC10mM_E2pt5fmol_kcat100k_EnzDegComb_rerun_quarter =
hotC10mM_E2pt5fmol_kcat100k_EnzDegComb_rerun_quarter -
coldC10mM_E2pt5fmol_kcat100k_EnzDegComb_rerun_quarter;
calresponse_C10mM_E2pt5fmol_kcat100k_EnzDegComb_rerun_quarter =
diffC10mM_E2pt5fmol_kcat100k_EnzDegComb_rerun_quarter*seebeck;


M = csvread('190430_CombModel_EnzDeg_C10mM_E2pt5fmol_kcat90k_110k_quarter_hot.csv');
M2 = csvread('190430_CombModel_EnzDeg_C10mM_E2pt5fmol_kcat90k_110k_quarter_cold.csv');
hotC10mM_E2pt5fmol_kcat90k_EnzDegComb_quarter = M(1:751,4);
coldC10mM_E2pt5fmol_kcat90k_EnzDegComb_quarter = M2(1:751,4);
hotC10mM_E2pt5fmol_kcat110k_EnzDegComb_quarter = M(752:1502,4);
coldC10mM_E2pt5fmol_kcat110k_EnzDegComb_quarter = M2(752:1502,4);
```

```
diffC10mM_E2pt5fmol_kcat90k_EnzDegComb_quarter =
hotC10mM_E2pt5fmol_kcat90k_EnzDegComb_quarter -
coldC10mM_E2pt5fmol_kcat90k_EnzDegComb_quarter;
calresponse_C10mM_E2pt5fmol_kcat90k_EnzDegComb_quarter =
diffC10mM_E2pt5fmol_kcat90k_EnzDegComb_quarter*seebeck;

diffC10mM_E2pt5fmol_kcat110k_EnzDegComb_quarter =
hotC10mM_E2pt5fmol_kcat110k_EnzDegComb_quarter -
coldC10mM_E2pt5fmol_kcat110k_EnzDegComb_quarter;
calresponse_C10mM_E2pt5fmol_kcat110k_EnzDegComb_quarter =
diffC10mM_E2pt5fmol_kcat110k_EnzDegComb_quarter*seebeck;

M = csvread('190430_CombModel_EnzDeg_C10mM_E2pt5fmol_kcat120k_130k_quarter_hot.csv');
M2 =
csvread('190430_CombModel_EnzDeg_C10mM_E2pt5fmol_kcat120k_130k_quarter_cold.csv');
hotC10mM_E2pt5fmol_kcat120k_EnzDegComb_quarter = M(1:751,4);
coldC10mM_E2pt5fmol_kcat120k_EnzDegComb_quarter = M2(1:751,4);
hotC10mM_E2pt5fmol_kcat130k_EnzDegComb_quarter = M(752:1502,4);
coldC10mM_E2pt5fmol_kcat130k_EnzDegComb_quarter = M2(752:1502,4);

diffC10mM_E2pt5fmol_kcat120k_EnzDegComb_quarter =
hotC10mM_E2pt5fmol_kcat120k_EnzDegComb_quarter -
coldC10mM_E2pt5fmol_kcat120k_EnzDegComb_quarter;
calresponse_C10mM_E2pt5fmol_kcat120k_EnzDegComb_quarter =
diffC10mM_E2pt5fmol_kcat120k_EnzDegComb_quarter*seebeck;

diffC10mM_E2pt5fmol_kcat130k_EnzDegComb_quarter =
hotC10mM_E2pt5fmol_kcat130k_EnzDegComb_quarter -
coldC10mM_E2pt5fmol_kcat130k_EnzDegComb_quarter;
calresponse_C10mM_E2pt5fmol_kcat130k_EnzDegComb_quarter =
diffC10mM_E2pt5fmol_kcat130k_EnzDegComb_quarter*seebeck;

M = csvread('190430_CombModel_EnzDeg_C10mM_E2pt5fmol_kcat80k_quarter_hot.csv');
M2 = csvread('190430_CombModel_EnzDeg_C10mM_E2pt5fmol_kcat80k_quarter_cold.csv');
hotC10mM_E2pt5fmol_kcat80k_EnzDegComb_quarter = M(:,2);
coldC10mM_E2pt5fmol_kcat80k_EnzDegComb_quarter = M2(:,2);

diffC10mM_E2pt5fmol_kcat80k_EnzDegComb_quarter =
hotC10mM_E2pt5fmol_kcat80k_EnzDegComb_quarter -
coldC10mM_E2pt5fmol_kcat80k_EnzDegComb_quarter;
calresponse_C10mM_E2pt5fmol_kcat80k_EnzDegComb_quarter =
diffC10mM_E2pt5fmol_kcat80k_EnzDegComb_quarter*seebeck;


M =
csvread('190502_CombModel_EnzDeg_C10mM_E2pt5fmol_kcat80k90k100k110k_threeeighths_hot.c
sv');
M2 =
csvread('190502_CombModel_EnzDeg_C10mM_E2pt5fmol_kcat80k90k100k110k_threeeighths_cold.
csv');
hotC10mM_E2pt5fmol_kcat80k_EnzDegComb_threeeighths = M(1:751,4);
coldC10mM_E2pt5fmol_kcat80k_EnzDegComb_threeeighths = M2(1:751,4);
hotC10mM_E2pt5fmol_kcat90k_EnzDegComb_threeeighths = M(752:1502,4);
coldC10mM_E2pt5fmol_kcat90k_EnzDegComb_threeeighths = M2(752:1502,4);
hotC10mM_E2pt5fmol_kcat100k_EnzDegComb_threeeighths = M(1503:2253,4);
coldC10mM_E2pt5fmol_kcat100k_EnzDegComb_threeeighths = M2(1503:2253,4);
hotC10mM_E2pt5fmol_kcat110k_EnzDegComb_threeeighths = M(2254:3004,4);
coldC10mM_E2pt5fmol_kcat110k_EnzDegComb_threeeighths = M2(2254:3004,4);


diffC10mM_E2pt5fmol_kcat80k_EnzDegComb_threeeighths =
hotC10mM_E2pt5fmol_kcat80k_EnzDegComb_threeeighths -
coldC10mM_E2pt5fmol_kcat80k_EnzDegComb_threeeighths;
```

```
calresponse_C10mM_E2pt5fmol_kcat80k_EnzDegComb_threeeighths =
diffC10mM_E2pt5fmol_kcat80k_EnzDegComb_threeeighths*seebeck;

diffC10mM_E2pt5fmol_kcat90k_EnzDegComb_threeeighths =
hotC10mM_E2pt5fmol_kcat90k_EnzDegComb_threeeighths -
coldC10mM_E2pt5fmol_kcat90k_EnzDegComb_threeeighths;
calresponse_C10mM_E2pt5fmol_kcat90k_EnzDegComb_threeeighths =
diffC10mM_E2pt5fmol_kcat90k_EnzDegComb_threeeighths*seebeck;

diffC10mM_E2pt5fmol_kcat100k_EnzDegComb_threeeighths =
hotC10mM_E2pt5fmol_kcat100k_EnzDegComb_threeeighths -
coldC10mM_E2pt5fmol_kcat100k_EnzDegComb_threeeighths;
calresponse_C10mM_E2pt5fmol_kcat100k_EnzDegComb_threeeighths =
diffC10mM_E2pt5fmol_kcat100k_EnzDegComb_threeeighths*seebeck;

diffC10mM_E2pt5fmol_kcat110k_EnzDegComb_threeeighths =
hotC10mM_E2pt5fmol_kcat110k_EnzDegComb_threeeighths -
coldC10mM_E2pt5fmol_kcat110k_EnzDegComb_threeeighths;
calresponse_C10mM_E2pt5fmol_kcat110k_EnzDegComb_threeeighths =
diffC10mM_E2pt5fmol_kcat110k_EnzDegComb_threeeighths*seebeck;


M = csvread('190501_CombModel_EnzDeg_C10mM_E2pt5fmol_kcat80k90k100k_eight_hot.csv');
M2 = csvread('190501_CombModel_EnzDeg_C10mM_E2pt5fmol_kcat80k90k100k_eight_cold.csv');
hotC10mM_E2pt5fmol_kcat80k_EnzDegComb_eighths = M(1:751,4);
coldC10mM_E2pt5fmol_kcat80k_EnzDegComb_eighths = M2(1:751,4);
hotC10mM_E2pt5fmol_kcat90k_EnzDegComb_eighths = M(752:1502,4);
coldC10mM_E2pt5fmol_kcat90k_EnzDegComb_eighths = M2(752:1502,4);
hotC10mM_E2pt5fmol_kcat100k_EnzDegComb_eighths = M(1503:2253,4);
coldC10mM_E2pt5fmol_kcat100k_EnzDegComb_eighths = M2(1503:2253,4);


M = csvread('190502_CombModel_EnzDeg_C10mM_E2pt5fmol_kcat110k_eighth_hot.csv');
M2 = csvread('190502_CombModel_EnzDeg_C10mM_E2pt5fmol_kcat110k_eighth_cold.csv');
hotC10mM_E2pt5fmol_kcat110k_EnzDegComb_eighths = M(1:751,4);
coldC10mM_E2pt5fmol_kcat110k_EnzDegComb_eighths = M2(1:751,4);


diffC10mM_E2pt5fmol_kcat80k_EnzDegComb_eighths =
hotC10mM_E2pt5fmol_kcat80k_EnzDegComb_eighths -
coldC10mM_E2pt5fmol_kcat80k_EnzDegComb_eighths;
calresponse_C10mM_E2pt5fmol_kcat80k_EnzDegComb_eighths =
diffC10mM_E2pt5fmol_kcat80k_EnzDegComb_eighths*seebeck;

diffC10mM_E2pt5fmol_kcat90k_EnzDegComb_eighths =
hotC10mM_E2pt5fmol_kcat90k_EnzDegComb_eighths -
coldC10mM_E2pt5fmol_kcat90k_EnzDegComb_eighths;
calresponse_C10mM_E2pt5fmol_kcat90k_EnzDegComb_eighths =
diffC10mM_E2pt5fmol_kcat90k_EnzDegComb_eighths*seebeck;

diffC10mM_E2pt5fmol_kcat100k_EnzDegComb_eighths =
hotC10mM_E2pt5fmol_kcat100k_EnzDegComb_eighths -
coldC10mM_E2pt5fmol_kcat100k_EnzDegComb_eighths;
calresponse_C10mM_E2pt5fmol_kcat100k_EnzDegComb_eighths =
diffC10mM_E2pt5fmol_kcat100k_EnzDegComb_eighths*seebeck;

diffC10mM_E2pt5fmol_kcat110k_EnzDegComb_eighths =
hotC10mM_E2pt5fmol_kcat110k_EnzDegComb_eighths -
coldC10mM_E2pt5fmol_kcat110k_EnzDegComb_eighths;
calresponse_C10mM_E2pt5fmol_kcat110k_EnzDegComb_eighths =
diffC10mM_E2pt5fmol_kcat110k_EnzDegComb_eighths*seebeck;
```

```
M =
csvread('190502_CombModel_EnzDeg_C10mM_E2pt5fmol_kcat80k90k100k110k_nodeg_hot.csv');
M2 =
csvread('190502_CombModel_EnzDeg_C10mM_E2pt5fmol_kcat80k90k100k110k_nodeg_cold.csv');
hotC10mM_E2pt5fmol_kcat80k_EnzDegComb_nodeg = M(1:751,4);
coldC10mM_E2pt5fmol_kcat80k_EnzDegComb_nodeg = M2(1:751,4);
hotC10mM_E2pt5fmol_kcat90k_EnzDegComb_nodeg = M(752:1502,4);
coldC10mM_E2pt5fmol_kcat90k_EnzDegComb_nodeg = M2(752:1502,4);
hotC10mM_E2pt5fmol_kcat100k_EnzDegComb_nodeg = M(1503:2253,4);
coldC10mM_E2pt5fmol_kcat100k_EnzDegComb_nodeg = M2(1503:2253,4);
hotC10mM_E2pt5fmol_kcat110k_EnzDegComb_nodeg = M(2254:3004,4);
coldC10mM_E2pt5fmol_kcat110k_EnzDegComb_nodeg = M2(2254:3004,4);


diffC10mM_E2pt5fmol_kcat80k_EnzDegComb_nodeg =
hotC10mM_E2pt5fmol_kcat80k_EnzDegComb_nodeg -
coldC10mM_E2pt5fmol_kcat80k_EnzDegComb_nodeg;
calresponse_C10mM_E2pt5fmol_kcat80k_EnzDegComb_nodeg =
diffC10mM_E2pt5fmol_kcat80k_EnzDegComb_nodeg*seebeck;

diffC10mM_E2pt5fmol_kcat90k_EnzDegComb_nodeg =
hotC10mM_E2pt5fmol_kcat90k_EnzDegComb_nodeg -
coldC10mM_E2pt5fmol_kcat90k_EnzDegComb_nodeg;
calresponse_C10mM_E2pt5fmol_kcat90k_EnzDegComb_nodeg =
diffC10mM_E2pt5fmol_kcat90k_EnzDegComb_nodeg*seebeck;

diffC10mM_E2pt5fmol_kcat100k_EnzDegComb_nodeg =
hotC10mM_E2pt5fmol_kcat100k_EnzDegComb_nodeg -
coldC10mM_E2pt5fmol_kcat100k_EnzDegComb_nodeg;
calresponse_C10mM_E2pt5fmol_kcat100k_EnzDegComb_nodeg =
diffC10mM_E2pt5fmol_kcat100k_EnzDegComb_nodeg*seebeck;

diffC10mM_E2pt5fmol_kcat110k_EnzDegComb_nodeg =
hotC10mM_E2pt5fmol_kcat110k_EnzDegComb_nodeg -
coldC10mM_E2pt5fmol_kcat110k_EnzDegComb_nodeg;
calresponse_C10mM_E2pt5fmol_kcat110k_EnzDegComb_nodeg =
diffC10mM_E2pt5fmol_kcat110k_EnzDegComb_nodeg*seebeck;


M =
csvread('190502_CombModel_EnzDeg_C10mM_E2pt5fmol_kcat80k90k100k110k_half_hot.csv');
M2 =
csvread('190502_CombModel_EnzDeg_C10mM_E2pt5fmol_kcat80k90k100k110k_half_cold.csv');
hotC10mM_E2pt5fmol_kcat80k_EnzDegComb_half = M(1:751,4);
coldC10mM_E2pt5fmol_kcat80k_EnzDegComb_half = M2(1:751,4);
hotC10mM_E2pt5fmol_kcat90k_EnzDegComb_half = M(752:1502,4);
coldC10mM_E2pt5fmol_kcat90k_EnzDegComb_half = M2(752:1502,4);
hotC10mM_E2pt5fmol_kcat100k_EnzDegComb_half = M(1503:2253,4);
coldC10mM_E2pt5fmol_kcat100k_EnzDegComb_half = M2(1503:2253,4);
hotC10mM_E2pt5fmol_kcat110k_EnzDegComb_half = M(2254:3004,4);
coldC10mM_E2pt5fmol_kcat110k_EnzDegComb_half = M2(2254:3004,4);


diffC10mM_E2pt5fmol_kcat80k_EnzDegComb_half =
hotC10mM_E2pt5fmol_kcat80k_EnzDegComb_half -
coldC10mM_E2pt5fmol_kcat80k_EnzDegComb_half;
calresponse_C10mM_E2pt5fmol_kcat80k_EnzDegComb_half =
diffC10mM_E2pt5fmol_kcat80k_EnzDegComb_half*seebeck;

diffC10mM_E2pt5fmol_kcat90k_EnzDegComb_half =
hotC10mM_E2pt5fmol_kcat90k_EnzDegComb_half -
coldC10mM_E2pt5fmol_kcat90k_EnzDegComb_half;
```

```
calresponse_C10mM_E2pt5fmol_kcat90k_EnzDegComb_half =
diffC10mM_E2pt5fmol_kcat90k_EnzDegComb_half*seebeck;

diffC10mM_E2pt5fmol_kcat100k_EnzDegComb_half =
hotC10mM_E2pt5fmol_kcat100k_EnzDegComb_half -
coldC10mM_E2pt5fmol_kcat100k_EnzDegComb_half;
calresponse_C10mM_E2pt5fmol_kcat100k_EnzDegComb_half =
diffC10mM_E2pt5fmol_kcat100k_EnzDegComb_half*seebeck;

diffC10mM_E2pt5fmol_kcat110k_EnzDegComb_half =
hotC10mM_E2pt5fmol_kcat110k_EnzDegComb_half -
coldC10mM_E2pt5fmol_kcat110k_EnzDegComb_half;
calresponse_C10mM_E2pt5fmol_kcat110k_EnzDegComb_half =
diffC10mM_E2pt5fmol_kcat110k_EnzDegComb_half*seebeck;



M = csvread('190505_CombModel_EnzDeg_C10mM_E2pt5fmol_kcat95k_quarter_hot.csv');
M2 = csvread('190505_CombModel_EnzDeg_C10mM_E2pt5fmol_kcat95k_quarter_cold.csv');
hotC10mM_E2pt5fmol_kcat95k_EnzDegComb_quarter = M(1:751,5);
coldC10mM_E2pt5fmol_kcat95k_EnzDegComb_quarter = M2(1:751,5);


M =
csvread('190505_CombModel_EnzDeg_C10mM_E2pt5fmol_kcat95k_half_threeeighths_hot.csv');
M2 =
csvread('190505_CombModel_EnzDeg_C10mM_E2pt5fmol_kcat95k_half_threeeighths_cold.csv');
hotC10mM_E2pt5fmol_kcat95k_EnzDegComb_half = M(1:751,5);
coldC10mM_E2pt5fmol_kcat95k_EnzDegComb_half = M2(1:751,5);
hotC10mM_E2pt5fmol_kcat95k_EnzDegComb_threeeighths = M(752:1502,5);
coldC10mM_E2pt5fmol_kcat95k_EnzDegComb_threeeighths = M2(752:1502,5);

M = csvread('190505_CombModel_EnzDeg_C10mM_E2pt5fmol_kcat95k_eighths_nodeg_hot.csv');
M2 =
csvread('190505_CombModel_EnzDeg_C10mM_E2pt5fmol_kcat95k_eighths_nodeg_cold.csv');
hotC10mM_E2pt5fmol_kcat95k_EnzDegComb_eighths = M(1:751,5);
coldC10mM_E2pt5fmol_kcat95k_EnzDegComb_eighths = M2(1:751,5);
hotC10mM_E2pt5fmol_kcat95k_EnzDegComb_nodeg = M(752:1502,5);
coldC10mM_E2pt5fmol_kcat95k_EnzDegComb_nodeg = M2(752:1502,5);

M = csvread('190506_CombModel_EnzDeg_C10mM_E0pt6_1pt4fmol_kcat95k_quarter_hot.csv');
M2 = csvread('190506_CombModel_EnzDeg_C10mM_E0pt6_1pt4fmol_kcat95k_quarter_cold.csv');
hotC10mM_E0pt6fmol_kcat95k_EnzDegComb_quarter = M(1:751,5);
coldC10mM_E0pt6fmol_kcat95k_EnzDegComb_quarter = M2(1:751,5);
hotC10mM_E1pt4fmol_kcat95k_EnzDegComb_quarter = M(752:1502,5);
coldC10mM_E1pt4fmol_kcat95k_EnzDegComb_quarter = M2(752:1502,5);

diffC10mM_E2pt5fmol_kcat95k_EnzDegComb_half =
hotC10mM_E2pt5fmol_kcat95k_EnzDegComb_half -
coldC10mM_E2pt5fmol_kcat95k_EnzDegComb_half;
calresponse_C10mM_E2pt5fmol_kcat95k_EnzDegComb_half =
diffC10mM_E2pt5fmol_kcat95k_EnzDegComb_half*seebeck;

diffC10mM_E2pt5fmol_kcat95k_EnzDegComb_threeeighths =
hotC10mM_E2pt5fmol_kcat95k_EnzDegComb_threeeighths -
coldC10mM_E2pt5fmol_kcat95k_EnzDegComb_threeeighths;
calresponse_C10mM_E2pt5fmol_kcat95k_EnzDegComb_threeeighths =
diffC10mM_E2pt5fmol_kcat95k_EnzDegComb_threeeighths*seebeck;

diffC10mM_E2pt5fmol_kcat95k_EnzDegComb_quarter =
hotC10mM_E2pt5fmol_kcat95k_EnzDegComb_quarter -
coldC10mM_E2pt5fmol_kcat95k_EnzDegComb_quarter;
```

```
calresponse_C10mM_E2pt5fmol_kcat95k_EnzDegComb_quarter =
diffC10mM_E2pt5fmol_kcat95k_EnzDegComb_quarter*seebeck;

diffC10mM_E2pt5fmol_kcat95k_EnzDegComb_eighths =
hotC10mM_E2pt5fmol_kcat95k_EnzDegComb_eighths -
coldC10mM_E2pt5fmol_kcat95k_EnzDegComb_eighths;
calresponse_C10mM_E2pt5fmol_kcat95k_EnzDegComb_eighths =
diffC10mM_E2pt5fmol_kcat95k_EnzDegComb_eighths*seebeck;

diffC10mM_E2pt5fmol_kcat95k_EnzDegComb_nodeg =
hotC10mM_E2pt5fmol_kcat95k_EnzDegComb_nodeg -
coldC10mM_E2pt5fmol_kcat95k_EnzDegComb_nodeg;
calresponse_C10mM_E2pt5fmol_kcat95k_EnzDegComb_nodeg =
diffC10mM_E2pt5fmol_kcat95k_EnzDegComb_nodeg*seebeck;

diffC10mM_E1pt4fmol_kcat95k_EnzDegComb_quarter =
hotC10mM_E1pt4fmol_kcat95k_EnzDegComb_quarter -
coldC10mM_E1pt4fmol_kcat95k_EnzDegComb_quarter;
calresponse_C10mM_E1pt4fmol_kcat95k_EnzDegComb_quarter =
diffC10mM_E1pt4fmol_kcat95k_EnzDegComb_quarter*seebeck;


kcat_R1 = [80000 90000 100000 110000 120000 130000];
kcat_full_R1 = [80000 90000 95000 100000 110000];
degredation_R1 = [0.5e-7 0.375e-7 0.25e-7 0.125e-7 0];

TELISA_2pt5fmol_run1_aligned = zeros(751,1);
TELISA_2pt5fmol_run1_aligned(1:500) = TELISA_2pt5fmol_Run1(501:1000);
TELISA_2pt5fmol_run1_aligned(501:751) = decimate(TELISA_2pt5fmol_Run1(1001:3501),10);

error_R1_kcat80k_DegQuarter = TELISA_2pt5fmol_run1_aligned(:)-(-
calresponse_C10mM_E2pt5fmol_kcat80k_EnzDegComb_quarter(:)*10^6);
error_R1_kcat90k_DegQuarter = TELISA_2pt5fmol_run1_aligned(:)-(-
calresponse_C10mM_E2pt5fmol_kcat90k_EnzDegComb_quarter(:)*10^6);
error_R1_kcat100k_DegQuarter = TELISA_2pt5fmol_run1_aligned(:)-(-
calresponse_C10mM_E2pt5fmol_kcat100k_EnzDegComb_rerun_quarter(:)*10^6);
error_R1_kcat110k_DegQuarter = TELISA_2pt5fmol_run1_aligned(:)-(-
calresponse_C10mM_E2pt5fmol_kcat110k_EnzDegComb_quarter(:)*10^6);
error_R1_kcat120k_DegQuarter = TELISA_2pt5fmol_run1_aligned(:)-(-
calresponse_C10mM_E2pt5fmol_kcat120k_EnzDegComb_quarter(:)*10^6);
error_R1_kcat130k_DegQuarter = TELISA_2pt5fmol_run1_aligned(:)-(-
calresponse_C10mM_E2pt5fmol_kcat130k_EnzDegComb_quarter(:)*10^6);

error_R1_kcat80k_DegEighths = TELISA_2pt5fmol_run1_aligned(:)-(-
calresponse_C10mM_E2pt5fmol_kcat80k_EnzDegComb_eighths(:)*10^6);
error_R1_kcat90k_DegEighths = TELISA_2pt5fmol_run1_aligned(:)-(-
calresponse_C10mM_E2pt5fmol_kcat90k_EnzDegComb_eighths(:)*10^6);
error_R1_kcat100k_DegEighths = TELISA_2pt5fmol_run1_aligned(:)-(-
calresponse_C10mM_E2pt5fmol_kcat100k_EnzDegComb_eighths(:)*10^6);
error_R1_kcat110k_DegEighths = TELISA_2pt5fmol_run1_aligned(:)-(-
calresponse_C10mM_E2pt5fmol_kcat110k_EnzDegComb_eighths(:)*10^6);

error_R1_kcat80k_DegThreeEighths = TELISA_2pt5fmol_run1_aligned(:)-(-
calresponse_C10mM_E2pt5fmol_kcat80k_EnzDegComb_threeeighths(:)*10^6);
error_R1_kcat90k_DegThreeEighths = TELISA_2pt5fmol_run1_aligned(:)-(-
calresponse_C10mM_E2pt5fmol_kcat90k_EnzDegComb_threeeighths(:)*10^6);
error_R1_kcat100k_DegThreeEighths = TELISA_2pt5fmol_run1_aligned(:)-(-
calresponse_C10mM_E2pt5fmol_kcat100k_EnzDegComb_threeeighths(:)*10^6);
error_R1_kcat110k_DegThreeEighths = TELISA_2pt5fmol_run1_aligned(:)-(-
calresponse_C10mM_E2pt5fmol_kcat110k_EnzDegComb_threeeighths(:)*10^6);

error_R1_kcat80k_DegNoDeg = TELISA_2pt5fmol_run1_aligned(:)-(-
calresponse_C10mM_E2pt5fmol_kcat80k_EnzDegComb_nodeg(:)*10^6);
```

```
error_R1_kcat90k_DegNoDeg = TELISA_2pt5fmol_run1_aligned(:)-(-
calresponse_C10mM_E2pt5fmol_kcat90k_EnzDegComb_nodeg(:)*10^6);
error_R1_kcat100k_DegNoDeg = TELISA_2pt5fmol_run1_aligned(:)-(-
calresponse_C10mM_E2pt5fmol_kcat100k_EnzDegComb_nodeg(:)*10^6);
error_R1_kcat110k_DegNoDeg = TELISA_2pt5fmol_run1_aligned(:)-(-
calresponse_C10mM_E2pt5fmol_kcat110k_EnzDegComb_nodeg(:)*10^6);

error_R1_kcat80k_DegHalf = TELISA_2pt5fmol_run1_aligned(:)-(-
calresponse_C10mM_E2pt5fmol_kcat80k_EnzDegComb_half(:)*10^6);
error_R1_kcat90k_DegHalf = TELISA_2pt5fmol_run1_aligned(:)-(-
calresponse_C10mM_E2pt5fmol_kcat90k_EnzDegComb_half(:)*10^6);
error_R1_kcat100k_DegHalf = TELISA_2pt5fmol_run1_aligned(:)-(-
calresponse_C10mM_E2pt5fmol_kcat100k_EnzDegComb_half(:)*10^6);
error_R1_kcat110k_DegHalf = TELISA_2pt5fmol_run1_aligned(:)-(-
calresponse_C10mM_E2pt5fmol_kcat110k_EnzDegComb_half(:)*10^6);

error_R1_kcat95k_DegHalf = TELISA_2pt5fmol_run1_aligned(:)-(-
calresponse_C10mM_E2pt5fmol_kcat95k_EnzDegComb_half(:)*10^6);
error_R1_kcat95k_DegThreeEighths = TELISA_2pt5fmol_run1_aligned(:)-(-
calresponse_C10mM_E2pt5fmol_kcat95k_EnzDegComb_threeeighths(:)*10^6);
error_R1_kcat95k_DegQuarter = TELISA_2pt5fmol_run1_aligned(:)-(-
calresponse_C10mM_E2pt5fmol_kcat95k_EnzDegComb_quarter(:)*10^6);
error_R1_kcat95k_DegEighths = TELISA_2pt5fmol_run1_aligned(:)-(-
calresponse_C10mM_E2pt5fmol_kcat95k_EnzDegComb_eighths(:)*10^6);
error_R1_kcat95k_DegNoDeg = TELISA_2pt5fmol_run1_aligned(:)-(-
calresponse_C10mM_E2pt5fmol_kcat95k_EnzDegComb_nodeg(:)*10^6);


figure(1)
subplot(2,1,1)
plot(T_comb,-calresponse_C10mM_E2pt5fmol_kcat80k_EnzDegComb_quarter(:)*10^6,T_comb,-
calresponse_C10mM_E2pt5fmol_kcat90k_EnzDegComb_quarter(:)*10^6,T_comb,-
calresponse_C10mM_E2pt5fmol_kcat100k_EnzDegComb_rerun_quarter(:)*10^6,T_comb,-
calresponse_C10mM_E2pt5fmol_kcat110k_EnzDegComb_quarter(:)*10^6,T_comb,-
calresponse_C10mM_E2pt5fmol_kcat120k_EnzDegComb_quarter(:)*10^6,T_comb,-
calresponse_C10mM_E2pt5fmol_kcat130k_EnzDegComb_quarter(:)*10^6,T_comb,TELISA_2pt5fmol
_run1_aligned,'--')
subplot(2,1,2)
plot(T_comb,error_R1_kcat80k_DegQuarter,T_comb,error_R1_kcat90k_DegQuarter,T_comb,erro
r_R1_kcat100k_DegQuarter,T_comb,error_R1_kcat110k_DegQuarter,T_comb,error_R1_kcat120k_
DegQuarter,T_comb,error_R1_kcat130k_DegQuarter)



%30 second error window
RMSE_R1_kcat80k_DegQuarter =
sqrt(sum(error_R1_kcat80k_DegQuarter.^2)/length(TELISA_2pt5fmol_run1_aligned(:)));
RMSE_R1_kcat90k_DegQuarter =
sqrt(sum(error_R1_kcat90k_DegQuarter.^2)/length(TELISA_2pt5fmol_run1_aligned(:)));
RMSE_R1_kcat100k_DegQuarter =
sqrt(sum(error_R1_kcat100k_DegQuarter.^2)/length(TELISA_2pt5fmol_run1_aligned(:)));
RMSE_R1_kcat110k_DegQuarter =
sqrt(sum(error_R1_kcat110k_DegQuarter.^2)/length(TELISA_2pt5fmol_run1_aligned(:)));
RMSE_R1_kcat120k_DegQuarter =
sqrt(sum(error_R1_kcat120k_DegQuarter.^2)/length(TELISA_2pt5fmol_run1_aligned(:)));
RMSE_R1_kcat130k_DegQuarter =
sqrt(sum(error_R1_kcat130k_DegQuarter.^2)/length(TELISA_2pt5fmol_run1_aligned(:)));


RMSE_R1_kcat80k_DegEighths =
sqrt(sum(error_R1_kcat80k_DegEighths.^2)/length(TELISA_2pt5fmol_run1_aligned(:)));
RMSE_R1_kcat90k_DegEighths =
sqrt(sum(error_R1_kcat90k_DegEighths.^2)/length(TELISA_2pt5fmol_run1_aligned(:)));
```

```
RMSE_R1_kcat100k_DegEighths =
sqrt(sum(error_R1_kcat100k_DegEighths.^2)/length(TELISA_2pt5fmol_run1_aligned(:)));
RMSE_R1_kcat110k_DegEighths =
sqrt(sum(error_R1_kcat110k_DegEighths.^2)/length(TELISA_2pt5fmol_run1_aligned(:)));

RMSE_R1_kcat80k_DegThreeEighths =
sqrt(sum(error_R1_kcat80k_DegThreeEighths.^2)/length(TELISA_2pt5fmol_run1_aligned(:)))
;
RMSE_R1_kcat90k_DegThreeEighths =
sqrt(sum(error_R1_kcat90k_DegThreeEighths.^2)/length(TELISA_2pt5fmol_run1_aligned(:)))
;
RMSE_R1_kcat100k_DegThreeEighths =
sqrt(sum(error_R1_kcat100k_DegThreeEighths.^2)/length(TELISA_2pt5fmol_run1_aligned(:))
);
RMSE_R1_kcat110k_DegThreeEighths =
sqrt(sum(error_R1_kcat110k_DegThreeEighths.^2)/length(TELISA_2pt5fmol_run1_aligned(:))
);


RMSE_R1_kcat80k_DegNoDeg =
sqrt(sum(error_R1_kcat80k_DegNoDeg.^2)/length(TELISA_2pt5fmol_run1_aligned(:)));
RMSE_R1_kcat90k_DegNoDeg =
sqrt(sum(error_R1_kcat90k_DegNoDeg.^2)/length(TELISA_2pt5fmol_run1_aligned(:)));
RMSE_R1_kcat100k_DegNoDeg =
sqrt(sum(error_R1_kcat100k_DegNoDeg.^2)/length(TELISA_2pt5fmol_run1_aligned(:)));
RMSE_R1_kcat110k_DegNoDeg =
sqrt(sum(error_R1_kcat110k_DegNoDeg.^2)/length(TELISA_2pt5fmol_run1_aligned(:)));

RMSE_R1_kcat80k_DegHalf =
sqrt(sum(error_R1_kcat80k_DegHalf.^2)/length(TELISA_2pt5fmol_run1_aligned(:)));
RMSE_R1_kcat90k_DegHalf =
sqrt(sum(error_R1_kcat90k_DegHalf.^2)/length(TELISA_2pt5fmol_run1_aligned(:)));
RMSE_R1_kcat100k_DegHalf =
sqrt(sum(error_R1_kcat100k_DegHalf.^2)/length(TELISA_2pt5fmol_run1_aligned(:)));
RMSE_R1_kcat110k_DegHalf =
sqrt(sum(error_R1_kcat110k_DegHalf.^2)/length(TELISA_2pt5fmol_run1_aligned(:)));

RMSE_R1_kcat95k_DegHalf =
sqrt(sum(error_R1_kcat95k_DegHalf.^2)/length(TELISA_2pt5fmol_run1_aligned(:)));
RMSE_R1_kcat95k_DegThreeEighths =
sqrt(sum(error_R1_kcat95k_DegThreeEighths.^2)/length(TELISA_2pt5fmol_run1_aligned(:)))
;
RMSE_R1_kcat95k_DegQuarter =
sqrt(sum(error_R1_kcat95k_DegQuarter.^2)/length(TELISA_2pt5fmol_run1_aligned(:)));
RMSE_R1_kcat95k_DegEighths =
sqrt(sum(error_R1_kcat95k_DegEighths.^2)/length(TELISA_2pt5fmol_run1_aligned(:)));
RMSE_R1_kcat95k_DegNoDeg =
sqrt(sum(error_R1_kcat95k_DegNoDeg.^2)/length(TELISA_2pt5fmol_run1_aligned(:)));

RMSE_R1 = [RMSE_R1_kcat80k_DegQuarter RMSE_R1_kcat90k_DegQuarter
RMSE_R1_kcat100k_DegQuarter RMSE_R1_kcat110k_DegQuarter RMSE_R1_kcat120k_DegQuarter
RMSE_R1_kcat130k_DegQuarter];


RMSE_R1_full = [RMSE_R1_kcat80k_DegHalf RMSE_R1_kcat90k_DegHalf
RMSE_R1_kcat95k_DegHalf RMSE_R1_kcat100k_DegHalf RMSE_R1_kcat110k_DegHalf;
RMSE_R1_kcat80k_DegThreeEighths RMSE_R1_kcat90k_DegThreeEighths
RMSE_R1_kcat95k_DegThreeEighths RMSE_R1_kcat100k_DegThreeEighths
RMSE_R1_kcat110k_DegThreeEighths; RMSE_R1_kcat80k_DegQuarter
RMSE_R1_kcat90k_DegQuarter RMSE_R1_kcat95k_DegQuarter RMSE_R1_kcat100k_DegQuarter
RMSE_R1_kcat110k_DegQuarter; RMSE_R1_kcat80k_DegEighths RMSE_R1_kcat90k_DegEighths
RMSE_R1_kcat95k_DegEighths RMSE_R1_kcat100k_DegEighths RMSE_R1_kcat110k_DegEighths;
```

```
RMSE_R1_kcat80k_DegNoDeg RMSE_R1_kcat90k_DegNoDeg RMSE_R1_kcat95k_DegNoDeg
RMSE_R1_kcat100k_DegNoDeg RMSE_R1_kcat110k_DegNoDeg];

figure(2)
surf(kcat_full_R1,degredation_R1,RMSE_R1_full)
hold on
set(gca,'FontSize',13);
CO = jet;
CO = flipud(CO);
colormap(CO);
view(2)
ylabel('Inactivation Factor')
xlabel('kcat (1/s)')
contour(kcat_full_R1,degredation_R1,RMSE_R1_full)
shading interp
h = colorbar;
ylabel(h,'RMSE')
%text(95000,0.25,'Minimum RMSE (95k, 0.25)')
hold off

%%%%%%%%%%%%%%%%%%%%%%%%%%%%%%%%%%%%%%%%%%%%%%%%%%%%%%%%%%%%%%%%%%%%%%%%%%%%%%%%%%%%%%%
%%%%%
%Run1 1.5 fmol and 1.0 fmol

%%%%%%%%%%%%%%%%%%%%%%%%%%%%%%%%%%%%%%%%%%%%%%%%%%%%%%%%%%%%%%%%%%%%%%%%%%%%%%%
M = csvread('190723_CombModel_EnzDeg_C10mM_Esweep_nonstrict_kcat95k_quarter_hot.csv');
M2 =
csvread('190723_CombModel_EnzDeg_C10mM_Esweep_nonstrict_kcat95k_quarter_cold.csv');
hotC10mM_E0pt2fmol_kcat95k_EnzDegComb_quarter = M(1:751,5);
coldC10mM_E0pt2fmol_kcat95k_EnzDegComb_quarter = M2(1:751,5);
hotC10mM_E0pt4fmol_kcat95k_EnzDegComb_quarter = M(752:1502,5);
coldC10mM_E0pt4fmol_kcat95k_EnzDegComb_quarter = M2(752:1502,5);
hotC10mM_E1pt45fmol_kcat95k_EnzDegComb_quarter = M(1503:2253,5);
coldC10mM_E1pt45fmol_kcat95k_EnzDegComb_quarter = M2(1503:2253,5);
hotC10mM_E1pt95fmol_kcat95k_EnzDegComb_quarter = M(2254:3004,5);
coldC10mM_E1pt95fmol_kcat95k_EnzDegComb_quarter = M2(2254:3004,5);
M =
csvread('190723_CombModel_EnzDeg_C10mM_Esweep2_nonstrict_kcat95k_quarter_hot.csv');
M2 =
csvread('190723_CombModel_EnzDeg_C10mM_Esweep2_nonstrict_kcat95k_quarter_cold.csv');
hotC10mM_E0pt95fmol_kcat95k_EnzDegComb_quarter = M(1:751,5);
coldC10mM_E0pt95fmol_kcat95k_EnzDegComb_quarter = M2(1:751,5);

%%%%%%%%%%%%%%%%%%%%%%%%%%%%%%%%%%%%%%%%%%%%%%%%%%%%%%%%%%%%%%%%%%%%%%%%%%%%%

Data1=dlmread('190329_0459_150nMCat_10mMH2O2_01.txt','\t');
TELISA_1pt5fmol_Run1=Data1(2645:6145,2);
TELISA_1pt5fmol_Run1=TELISA_1pt5fmol_Run1/10000*1e6;    %amp gain correction
X_1pt5fmol_Run1=1/f:1/f:N/f;
X_1pt5fmol_Run1 = (X_1pt5fmol_Run1-5);
preBaseline_1pt5fmol_Run1 = mean(TELISA_1pt5fmol_Run1(10:260));
TELISA_1pt5fmol_Run1 = TELISA_1pt5fmol_Run1-preBaseline_1pt5fmol_Run1;

TELISA_1pt5fmol_run1_aligned = zeros(751,1);
TELISA_1pt5fmol_run1_aligned(1:500) = TELISA_1pt5fmol_Run1(501:1000);
TELISA_1pt5fmol_run1_aligned(501:751) = decimate(TELISA_1pt5fmol_Run1(1001:3501),10);

M = csvread('190504_CombModel_EnzDeg_C10mM_E1pt5fmol_kcat95k_quarter_hot.csv');
M2 = csvread('190504_CombModel_EnzDeg_C10mM_E1pt5fmol_kcat95k_quarter_cold.csv');
hotC10mM_E1pt5fmol_kcat95k_EnzDegComb_quarter = M(1:751,5);
coldC10mM_E1pt5fmol_kcat95k_EnzDegComb_quarter = M2(1:751,5);

M = csvread('190505_CombModel_EnzDeg_C10mM_E1pt1to1pt9fmol_kcat95k_quarter_hot.csv');
```

```
M2 =
csvread('190505_CombModel_EnzDeg_C10mM_E1pt1to1pt9fmol_kcat95k_quarter_cold.csv');
hotC10mM_E1pt1fmol_kcat95k_EnzDegComb_quarter = M(1:751,5);
coldC10mM_E1pt1fmol_kcat95k_EnzDegComb_quarter = M2(1:751,5);
hotC10mM_E1pt3fmol_kcat95k_EnzDegComb_quarter = M(752:1502,5);
coldC10mM_E1pt3fmol_kcat95k_EnzDegComb_quarter = M2(752:1502,5);
hotC10mM_E1pt7fmol_kcat95k_EnzDegComb_quarter = M(1503:2253,5);
coldC10mM_E1pt7fmol_kcat95k_EnzDegComb_quarter = M2(1503:2253,5);
hotC10mM_E1pt9fmol_kcat95k_EnzDegComb_quarter = M(2254:3004,5);
coldC10mM_E1pt9fmol_kcat95k_EnzDegComb_quarter = M2(2254:3004,5);

M = csvread('190722_CombModel_EnzDeg_C10mM_E0pt95_1pt45fmol_kcat95k_quarter_hot.csv');
M2 =
csvread('190722_CombModel_EnzDeg_C10mM_E0pt95_1pt45fmol_kcat95k_quarter_cold.csv');
hotC10mM_E0pt95fmol_kcat95k_EnzDegStrict_quarter = M(1:751,5);
coldC10mM_E0pt95fmol_kcat95k_EnzDegStrict_quarter = M2(1:751,5);
hotC10mM_E1pt45fmol_kcat95k_EnzDegStrict_quarter = M(752:1502,5);
coldC10mM_E1pt45fmol_kcat95k_EnzDegStrict_quarter = M2(752:1502,5);

diffC10mM_E0pt95fmol_kcat95k_EnzDegComb_quarter =
hotC10mM_E0pt95fmol_kcat95k_EnzDegComb_quarter -
coldC10mM_E0pt95fmol_kcat95k_EnzDegComb_quarter;
calresponse_C10mM_E0pt95fmol_kcat95k_EnzDegComb_quarter =
diffC10mM_E0pt95fmol_kcat95k_EnzDegComb_quarter*seebeck;

diffC10mM_E1pt1fmol_kcat95k_EnzDegComb_quarter =
hotC10mM_E1pt1fmol_kcat95k_EnzDegComb_quarter -
coldC10mM_E1pt1fmol_kcat95k_EnzDegComb_quarter;
calresponse_C10mM_E1pt1fmol_kcat95k_EnzDegComb_quarter =
diffC10mM_E1pt1fmol_kcat95k_EnzDegComb_quarter*seebeck;

diffC10mM_E1pt3fmol_kcat95k_EnzDegComb_quarter =
hotC10mM_E1pt3fmol_kcat95k_EnzDegComb_quarter -
coldC10mM_E1pt3fmol_kcat95k_EnzDegComb_quarter;
calresponse_C10mM_E1pt3fmol_kcat95k_EnzDegComb_quarter =
diffC10mM_E1pt3fmol_kcat95k_EnzDegComb_quarter*seebeck;

diffC10mM_E1pt45fmol_kcat95k_EnzDegComb_quarter =
hotC10mM_E1pt45fmol_kcat95k_EnzDegComb_quarter -
coldC10mM_E1pt45fmol_kcat95k_EnzDegComb_quarter;
calresponse_C10mM_E1pt45fmol_kcat95k_EnzDegComb_quarter =
diffC10mM_E1pt45fmol_kcat95k_EnzDegComb_quarter*seebeck;

diffC10mM_E1pt5fmol_kcat95k_EnzDegComb_quarter =
hotC10mM_E1pt5fmol_kcat95k_EnzDegComb_quarter -
coldC10mM_E1pt5fmol_kcat95k_EnzDegComb_quarter;
calresponse_C10mM_E1pt5fmol_kcat95k_EnzDegComb_quarter =
diffC10mM_E1pt5fmol_kcat95k_EnzDegComb_quarter*seebeck;

diffC10mM_E1pt7fmol_kcat95k_EnzDegComb_quarter =
hotC10mM_E1pt7fmol_kcat95k_EnzDegComb_quarter -
coldC10mM_E1pt7fmol_kcat95k_EnzDegComb_quarter;
calresponse_C10mM_E1pt7fmol_kcat95k_EnzDegComb_quarter =
diffC10mM_E1pt7fmol_kcat95k_EnzDegComb_quarter*seebeck;

diffC10mM_E1pt9fmol_kcat95k_EnzDegComb_quarter =
hotC10mM_E1pt9fmol_kcat95k_EnzDegComb_quarter -
coldC10mM_E1pt9fmol_kcat95k_EnzDegComb_quarter;
calresponse_C10mM_E1pt9fmol_kcat95k_EnzDegComb_quarter =
diffC10mM_E1pt9fmol_kcat95k_EnzDegComb_quarter*seebeck;

error_R1_c1pt1fmol_kcat95k_DegQuarter = TELISA_1pt5fmol_run1_aligned(:)-(-
calresponse_C10mM_E1pt1fmol_kcat95k_EnzDegComb_quarter(:)*10^6);
```

```
error_R1_c1pt3fmol_kcat95k_DegQuarter = TELISA_1pt5fmol_run1_aligned(:)-(-
calresponse_C10mM_E1pt3fmol_kcat95k_EnzDegComb_quarter(:)*10^6);
error_R1_c1pt4fmol_kcat95k_DegQuarter = TELISA_1pt5fmol_run1_aligned(:)-(-
calresponse_C10mM_E1pt4fmol_kcat95k_EnzDegComb_quarter(:)*10^6);
error_R1_c1pt45fmol_kcat95k_DegQuarter = TELISA_1pt5fmol_run1_aligned(:)-(-
calresponse_C10mM_E1pt45fmol_kcat95k_EnzDegComb_quarter(:)*10^6);
error_R1_c1pt5fmol_kcat95k_DegQuarter = TELISA_1pt5fmol_run1_aligned(:)-(-
calresponse_C10mM_E1pt5fmol_kcat95k_EnzDegComb_quarter(:)*10^6);
error_R1_c1pt7fmol_kcat95k_DegQuarter = TELISA_1pt5fmol_run1_aligned(:)-(-
calresponse_C10mM_E1pt7fmol_kcat95k_EnzDegComb_quarter(:)*10^6);
error_R1_c1pt9fmol_kcat95k_DegQuarter = TELISA_1pt5fmol_run1_aligned(:)-(-
calresponse_C10mM_E1pt9fmol_kcat95k_EnzDegComb_quarter(:)*10^6);

RMSE_R1_c1pt1fmol_kcat95k_DegQuarter =
sqrt(sum(error_R1_c1pt1fmol_kcat95k_DegQuarter.^2)/length(TELISA_1pt5fmol_run1_aligned
(:)));
RMSE_R1_c1pt3fmol_kcat95k_DegQuarter =
sqrt(sum(error_R1_c1pt3fmol_kcat95k_DegQuarter.^2)/length(TELISA_1pt5fmol_run1_aligned
(:)));
RMSE_R1_c1pt4fmol_kcat95k_DegQuarter =
sqrt(sum(error_R1_c1pt4fmol_kcat95k_DegQuarter.^2)/length(TELISA_1pt5fmol_run1_aligned
(:)));
RMSE_R1_c1pt45fmol_kcat95k_DegQuarter =
sqrt(sum(error_R1_c1pt45fmol_kcat95k_DegQuarter.^2)/length(TELISA_1pt5fmol_run1_aligne
d(:)));
RMSE_R1_c1pt5fmol_kcat95k_DegQuarter =
sqrt(sum(error_R1_c1pt5fmol_kcat95k_DegQuarter.^2)/length(TELISA_1pt5fmol_run1_aligned
(:)));
RMSE_R1_c1pt7fmol_kcat95k_DegQuarter =
sqrt(sum(error_R1_c1pt7fmol_kcat95k_DegQuarter.^2)/length(TELISA_1pt5fmol_run1_aligned
(:)));
RMSE_R1_c1pt9fmol_kcat95k_DegQuarter =
sqrt(sum(error_R1_c1pt9fmol_kcat95k_DegQuarter.^2)/length(TELISA_1pt5fmol_run1_aligned
(:)));

RMSE_R1_1pt5fmol = [RMSE_R1_c1pt1fmol_kcat95k_DegQuarter
RMSE_R1_c1pt3fmol_kcat95k_DegQuarter RMSE_R1_c1pt4fmol_kcat95k_DegQuarter
RMSE_R1_c1pt45fmol_kcat95k_DegQuarter RMSE_R1_c1pt5fmol_kcat95k_DegQuarter
RMSE_R1_c1pt7fmol_kcat95k_DegQuarter RMSE_R1_c1pt9fmol_kcat95k_DegQuarter];



M =
csvread('190723_CombModel_EnzDeg_C10mM_Esweep_1pt5fmolRun1_kcat95k_quarter_hot.csv');
M2 =
csvread('190723_CombModel_EnzDeg_C10mM_Esweep_1pt5fmolRun1_kcat95k_quarter_cold.csv');
hotC10mM_E1pt1fmol_kcat95k_EnzDegStrict_quarter = M(1:751,5);
coldC10mM_E1pt1fmol_kcat95k_EnzDegStrict_quarter = M2(1:751,5);
hotC10mM_E1pt3fmol_kcat95k_EnzDegStrict_quarter = M(752:1502,5);
coldC10mM_E1pt3fmol_kcat95k_EnzDegStrict_quarter = M2(752:1502,5);
hotC10mM_E1pt4fmol_kcat95k_EnzDegStrict_quarter = M(1503:2253,5);
coldC10mM_E1pt4fmol_kcat95k_EnzDegStrict_quarter = M2(1503:2253,5);
hotC10mM_E1pt5fmol_kcat95k_EnzDegStrict_quarter = M(2254:3004,5);
coldC10mM_E1pt5fmol_kcat95k_EnzDegStrict_quarter = M2(2254:3004,5);
hotC10mM_E1pt7fmol_kcat95k_EnzDegStrict_quarter = M(3005:3755,5);
coldC10mM_E1pt7fmol_kcat95k_EnzDegStrict_quarter = M2(3005:3755,5);
hotC10mM_E1pt9fmol_kcat95k_EnzDegStrict_quarter = M(3756:4506,5);
coldC10mM_E1pt9fmol_kcat95k_EnzDegStrict_quarter = M2(3756:4506,5);

calresponse_C10mM_E1pt1fmol_kcat95k_EnzDegStrict_quarter =
(hotC10mM_E1pt1fmol_kcat95k_EnzDegStrict_quarter -
coldC10mM_E1pt1fmol_kcat95k_EnzDegStrict_quarter)*seebeck;
```

```
calresponse_C10mM_E1pt3fmol_kcat95k_EnzDegStrict_quarter =
(hotC10mM_E1pt3fmol_kcat95k_EnzDegStrict_quarter -
coldC10mM_E1pt3fmol_kcat95k_EnzDegStrict_quarter)*seebeck;
calresponse_C10mM_E1pt4fmol_kcat95k_EnzDegStrict_quarter =
(hotC10mM_E1pt4fmol_kcat95k_EnzDegStrict_quarter -
coldC10mM_E1pt4fmol_kcat95k_EnzDegStrict_quarter)*seebeck;
calresponse_C10mM_E1pt5fmol_kcat95k_EnzDegStrict_quarter =
(hotC10mM_E1pt5fmol_kcat95k_EnzDegStrict_quarter -
coldC10mM_E1pt5fmol_kcat95k_EnzDegStrict_quarter)*seebeck;
calresponse_C10mM_E1pt7fmol_kcat95k_EnzDegStrict_quarter =
(hotC10mM_E1pt7fmol_kcat95k_EnzDegStrict_quarter -
coldC10mM_E1pt7fmol_kcat95k_EnzDegStrict_quarter)*seebeck;
calresponse_C10mM_E1pt9fmol_kcat95k_EnzDegStrict_quarter =
(hotC10mM_E1pt9fmol_kcat95k_EnzDegStrict_quarter -
coldC10mM_E1pt9fmol_kcat95k_EnzDegStrict_quarter)*seebeck;

error_R1strict_c1pt1fmol_kcat95k_DegQuarter = TELISA_1pt5fmol_run1_aligned(:)-(-
calresponse_C10mM_E1pt1fmol_kcat95k_EnzDegStrict_quarter(:)*10^6);
error_R1strict_c1pt3fmol_kcat95k_DegQuarter = TELISA_1pt5fmol_run1_aligned(:)-(-
calresponse_C10mM_E1pt3fmol_kcat95k_EnzDegStrict_quarter(:)*10^6);
error_R1strict_c1pt4fmol_kcat95k_DegQuarter = TELISA_1pt5fmol_run1_aligned(:)-(-
calresponse_C10mM_E1pt4fmol_kcat95k_EnzDegStrict_quarter(:)*10^6);
error_R1strict_c1pt5fmol_kcat95k_DegQuarter = TELISA_1pt5fmol_run1_aligned(:)-(-
calresponse_C10mM_E1pt5fmol_kcat95k_EnzDegStrict_quarter(:)*10^6);
error_R1strict_c1pt7fmol_kcat95k_DegQuarter = TELISA_1pt5fmol_run1_aligned(:)-(-
calresponse_C10mM_E1pt7fmol_kcat95k_EnzDegStrict_quarter(:)*10^6);
error_R1strict_c1pt9fmol_kcat95k_DegQuarter = TELISA_1pt5fmol_run1_aligned(:)-(-
calresponse_C10mM_E1pt9fmol_kcat95k_EnzDegStrict_quarter(:)*10^6);

RMSE_R1strict_c1pt1fmol_kcat95k_DegQuarter =
sqrt(sum(error_R1strict_c1pt1fmol_kcat95k_DegQuarter.^2)/length(TELISA_1pt5fmol_run1_a
ligned(:)));
RMSE_R1strict_c1pt3fmol_kcat95k_DegQuarter =
sqrt(sum(error_R1strict_c1pt3fmol_kcat95k_DegQuarter.^2)/length(TELISA_1pt5fmol_run1_a
ligned(:)));
RMSE_R1strict_c1pt4fmol_kcat95k_DegQuarter =
sqrt(sum(error_R1strict_c1pt4fmol_kcat95k_DegQuarter.^2)/length(TELISA_1pt5fmol_run1_a
ligned(:)));
RMSE_R1strict_c1pt5fmol_kcat95k_DegQuarter =
sqrt(sum(error_R1strict_c1pt5fmol_kcat95k_DegQuarter.^2)/length(TELISA_1pt5fmol_run1_a
ligned(:)));
RMSE_R1strict_c1pt7fmol_kcat95k_DegQuarter =
sqrt(sum(error_R1strict_c1pt7fmol_kcat95k_DegQuarter.^2)/length(TELISA_1pt5fmol_run1_a
ligned(:)));
RMSE_R1strict_c1pt9fmol_kcat95k_DegQuarter =
sqrt(sum(error_R1strict_c1pt9fmol_kcat95k_DegQuarter.^2)/length(TELISA_1pt5fmol_run1_a
ligned(:)));

RMSE_R1strict_1pt5fmol = [RMSE_R1strict_c1pt1fmol_kcat95k_DegQuarter
RMSE_R1strict_c1pt3fmol_kcat95k_DegQuarter RMSE_R1strict_c1pt4fmol_kcat95k_DegQuarter
RMSE_R1strict_c1pt5fmol_kcat95k_DegQuarter RMSE_R1strict_c1pt7fmol_kcat95k_DegQuarter
RMSE_R1strict_c1pt9fmol_kcat95k_DegQuarter];



figure(3)
subplot(2,1,1)
plot(T_comb,-calresponse_C10mM_E1pt1fmol_kcat95k_EnzDegComb_quarter*10^6,'r',T_comb,-
calresponse_C10mM_E1pt3fmol_kcat95k_EnzDegComb_quarter*10^6,'r',T_comb,-
calresponse_C10mM_E1pt4fmol_kcat95k_EnzDegComb_quarter*10^6,'r',T_comb,-
calresponse_C10mM_E1pt45fmol_kcat95k_EnzDegComb_quarter*10^6,'r',T_comb,-
calresponse_C10mM_E1pt5fmol_kcat95k_EnzDegComb_quarter*10^6,'r',T_comb,-
calresponse_C10mM_E1pt7fmol_kcat95k_EnzDegComb_quarter*10^6,'r',T_comb,-
```

```
calresponse_C10mM_E1pt9fmol_kcat95k_EnzDegComb_quarter*10^6,'r',X_1pt5fmol_Run1,TELISA
_1pt5fmol_Run1,'b',T_comb,-
calresponse_C10mM_E1pt1fmol_kcat95k_EnzDegStrict_quarter*10^6,'m',T_comb,-
calresponse_C10mM_E1pt3fmol_kcat95k_EnzDegStrict_quarter*10^6,'m',T_comb,-
calresponse_C10mM_E1pt4fmol_kcat95k_EnzDegStrict_quarter*10^6,'m',T_comb,-
calresponse_C10mM_E1pt5fmol_kcat95k_EnzDegStrict_quarter*10^6,'m',T_comb,-
calresponse_C10mM_E1pt7fmol_kcat95k_EnzDegStrict_quarter*10^6,'m',T_comb,-
calresponse_C10mM_E1pt9fmol_kcat95k_EnzDegStrict_quarter*10^6,'m')
axis([-2 30 -12.5 2])
subplot(2,1,2)
plot([1.1 1.3 1.4 1.45 1.5 1.7 1.9],RMSE_R1_1pt5fmol,'-o',[1.1 1.3 1.4 1.5 1.7
1.9],RMSE_R1strict_1pt5fmol,'-ro')



M = csvread('190505_CombModel_EnzDeg_C10mM_E0pt8to1pt2fmol_kcat95k_quarter_hot.csv');
M2 =
csvread('190505_CombModel_EnzDeg_C10mM_E0pt8to1pt2fmol_kcat95k_quarter_cold.csv');
hotC10mM_E0pt8fmol_kcat95k_EnzDegComb_quarter = M(1:751,5);
coldC10mM_E0pt8fmol_kcat95k_EnzDegComb_quarter = M2(1:751,5);
hotC10mM_E1pt0fmol_kcat95k_EnzDegComb_quarter = M(752:1502,5);
coldC10mM_E1pt0fmol_kcat95k_EnzDegComb_quarter = M2(752:1502,5);
hotC10mM_E1pt2fmol_kcat95k_EnzDegComb_quarter = M(1503:2253,5);
coldC10mM_E1pt2fmol_kcat95k_EnzDegComb_quarter = M2(1503:2253,5);



M = csvread('190722_CombModel_EnzDeg_C10mM_E0pt2_0pt4fmol_kcat95k_quarter_hot.csv');
M2 = csvread('190722_CombModel_EnzDeg_C10mM_E0pt2_0pt4fmol_kcat95k_quarter_cold.csv');
hotC10mM_E0pt2fmol_kcat95k_EnzDegStrict_quarter = M(1:751,5);
coldC10mM_E0pt2fmol_kcat95k_EnzDegStrict_quarter = M2(1:751,5);
hotC10mM_E0pt4fmol_kcat95k_EnzDegStrict_quarter = M(752:1502,5);
coldC10mM_E0pt4fmol_kcat95k_EnzDegStrict_quarter = M2(752:1502,5);

diffC10mM_E0pt2fmol_kcat95k_EnzDegComb_quarter =
hotC10mM_E0pt2fmol_kcat95k_EnzDegComb_quarter -
coldC10mM_E0pt2fmol_kcat95k_EnzDegComb_quarter;
calresponse_C10mM_E0pt2fmol_kcat95k_EnzDegComb_quarter =
diffC10mM_E0pt2fmol_kcat95k_EnzDegComb_quarter*seebeck;

diffC10mM_E0pt4fmol_kcat95k_EnzDegComb_quarter =
hotC10mM_E0pt4fmol_kcat95k_EnzDegComb_quarter -
coldC10mM_E0pt4fmol_kcat95k_EnzDegComb_quarter;
calresponse_C10mM_E0pt4fmol_kcat95k_EnzDegComb_quarter =
diffC10mM_E0pt4fmol_kcat95k_EnzDegComb_quarter*seebeck;

diffC10mM_E0pt6fmol_kcat95k_EnzDegComb_quarter =
hotC10mM_E0pt6fmol_kcat95k_EnzDegComb_quarter -
coldC10mM_E0pt6fmol_kcat95k_EnzDegComb_quarter;
calresponse_C10mM_E0pt6fmol_kcat95k_EnzDegComb_quarter =
diffC10mM_E0pt6fmol_kcat95k_EnzDegComb_quarter*seebeck;

diffC10mM_E0pt8fmol_kcat95k_EnzDegComb_quarter =
hotC10mM_E0pt8fmol_kcat95k_EnzDegComb_quarter -
coldC10mM_E0pt8fmol_kcat95k_EnzDegComb_quarter;
calresponse_C10mM_E0pt8fmol_kcat95k_EnzDegComb_quarter =
diffC10mM_E0pt8fmol_kcat95k_EnzDegComb_quarter*seebeck;

diffC10mM_E1pt0fmol_kcat95k_EnzDegComb_quarter =
hotC10mM_E1pt0fmol_kcat95k_EnzDegComb_quarter -
coldC10mM_E1pt0fmol_kcat95k_EnzDegComb_quarter;
calresponse_C10mM_E1pt0fmol_kcat95k_EnzDegComb_quarter =
diffC10mM_E1pt0fmol_kcat95k_EnzDegComb_quarter*seebeck;
```

```
diffC10mM_E1pt2fmol_kcat95k_EnzDegComb_quarter =
hotC10mM_E1pt2fmol_kcat95k_EnzDegComb_quarter -
coldC10mM_E1pt2fmol_kcat95k_EnzDegComb_quarter;
calresponse_C10mM_E1pt2fmol_kcat95k_EnzDegComb_quarter =
diffC10mM_E1pt2fmol_kcat95k_EnzDegComb_quarter*seebeck;



M = csvread('191023_CombModel_Remesh_C10mM_E0pt9_1pt1_kcat95k_quarter_hot.csv');
M2 = csvread('191023_CombModel_Remesh_C10mM_E0pt9_1pt1_kcat95k_quarter_cold.csv');
hotC10mM_E0pt9fmol_kcat95k_EnzDegComb_quarter_remesh = M(1:751,5);
coldC10mM_E0pt9fmol_kcat95k_EnzDegComb_quarter_remesh = M2(1:751,5);
hotC10mM_E1pt1fmol_kcat95k_EnzDegComb_quarter_remesh = M(752:1502,5);
coldC10mM_E1pt1fmol_kcat95k_EnzDegComb_quarter_remesh = M2(752:1502,5);

diffC10mM_E0pt9fmol_kcat95k_EnzDegComb_quarter_remesh =
hotC10mM_E0pt9fmol_kcat95k_EnzDegComb_quarter_remesh -
coldC10mM_E0pt9fmol_kcat95k_EnzDegComb_quarter_remesh;
calresponse_C10mM_E0pt9fmol_kcat95k_EnzDegComb_quarter_remesh =
diffC10mM_E0pt9fmol_kcat95k_EnzDegComb_quarter_remesh*seebeck;
diffC10mM_E1pt1fmol_kcat95k_EnzDegComb_quarter_remesh =
hotC10mM_E1pt1fmol_kcat95k_EnzDegComb_quarter_remesh -
coldC10mM_E1pt1fmol_kcat95k_EnzDegComb_quarter_remesh;
calresponse_C10mM_E1pt1fmol_kcat95k_EnzDegComb_quarter_remesh =
diffC10mM_E1pt1fmol_kcat95k_EnzDegComb_quarter_remesh*seebeck;



Data1=dlmread('190329_0461_100nMCat_10mMH2O2_01.txt','\t');
TELISA_1pt0fmol_Run1=Data1(3455:6955,2);
TELISA_1pt0fmol_Run1=TELISA_1pt0fmol_Run1/10000*1e6;    %amp gain correction
X_1pt0fmol_Run1=1/f:1/f:N/f;
X_1pt0fmol_Run1 = (X_1pt0fmol_Run1-5);
preBaseline_1pt0fmol_Run1 = mean(TELISA_1pt0fmol_Run1(10:260));
TELISA_1pt0fmol_Run1 = TELISA_1pt0fmol_Run1-preBaseline_1pt0fmol_Run1;

TELISA_1pt0fmol_run1_aligned = zeros(751,1);
TELISA_1pt0fmol_run1_aligned(1:500) = TELISA_1pt0fmol_Run1(501:1000);
TELISA_1pt0fmol_run1_aligned(501:751) = decimate(TELISA_1pt0fmol_Run1(1001:3501),10);

error_R1_c0pt2fmol_kcat95k_DegQuarter = TELISA_1pt0fmol_run1_aligned(:)-(-
calresponse_C10mM_E0pt2fmol_kcat95k_EnzDegComb_quarter(:)*10^6);
error_R1_c0pt4fmol_kcat95k_DegQuarter = TELISA_1pt0fmol_run1_aligned(:)-(-
calresponse_C10mM_E0pt4fmol_kcat95k_EnzDegComb_quarter(:)*10^6);
error_R1_c0pt6fmol_kcat95k_DegQuarter = TELISA_1pt0fmol_run1_aligned(:)-(-
calresponse_C10mM_E0pt6fmol_kcat95k_EnzDegComb_quarter(:)*10^6);
error_R1_c0pt8fmol_kcat95k_DegQuarter = TELISA_1pt0fmol_run1_aligned(:)-(-
calresponse_C10mM_E0pt8fmol_kcat95k_EnzDegComb_quarter(:)*10^6);
error_R1_c1pt0fmol_kcat95k_DegQuarter = TELISA_1pt0fmol_run1_aligned(:)-(-
calresponse_C10mM_E1pt0fmol_kcat95k_EnzDegComb_quarter(:)*10^6);
error_R1_c1pt2fmol_kcat95k_DegQuarter = TELISA_1pt0fmol_run1_aligned(:)-(-
calresponse_C10mM_E1pt2fmol_kcat95k_EnzDegComb_quarter(:)*10^6);
error_R1_c1pt4fmol_kcat95k_DegQuarter = TELISA_1pt0fmol_run1_aligned(:)-(-
calresponse_C10mM_E1pt4fmol_kcat95k_EnzDegComb_quarter(:)*10^6);

RMSE_R1_c0pt2fmol_kcat95k_DegQuarter =
sqrt(sum(error_R1_c0pt2fmol_kcat95k_DegQuarter.^2)/length(TELISA_1pt0fmol_run1_aligned
(:)));
RMSE_R1_c0pt4fmol_kcat95k_DegQuarter =
sqrt(sum(error_R1_c0pt4fmol_kcat95k_DegQuarter.^2)/length(TELISA_1pt0fmol_run1_aligned
(:)));
```

```
RMSE_R1_c0pt6fmol_kcat95k_DegQuarter =
sqrt(sum(error_R1_c0pt6fmol_kcat95k_DegQuarter.^2)/length(TELISA_1pt0fmol_run1_aligned
(:)));
RMSE_R1_c0pt8fmol_kcat95k_DegQuarter =
sqrt(sum(error_R1_c0pt8fmol_kcat95k_DegQuarter.^2)/length(TELISA_1pt0fmol_run1_aligned
(:)));
RMSE_R1_c1pt0fmol_kcat95k_DegQuarter =
sqrt(sum(error_R1_c1pt0fmol_kcat95k_DegQuarter.^2)/length(TELISA_1pt0fmol_run1_aligned
(:)));
RMSE_R1_c1pt2fmol_kcat95k_DegQuarter =
sqrt(sum(error_R1_c1pt2fmol_kcat95k_DegQuarter.^2)/length(TELISA_1pt0fmol_run1_aligned
(:)));
RMSE_R1_c1pt4fmol_kcat95k_DegQuarter =
sqrt(sum(error_R1_c1pt4fmol_kcat95k_DegQuarter.^2)/length(TELISA_1pt0fmol_run1_aligned
(:)));

RMSE_R1_1fmol = [RMSE_R1_c0pt2fmol_kcat95k_DegQuarter
RMSE_R1_c0pt4fmol_kcat95k_DegQuarter RMSE_R1_c0pt6fmol_kcat95k_DegQuarter
RMSE_R1_c0pt8fmol_kcat95k_DegQuarter RMSE_R1_c1pt0fmol_kcat95k_DegQuarter
RMSE_R1_c1pt2fmol_kcat95k_DegQuarter RMSE_R1_c1pt4fmol_kcat95k_DegQuarter];

figure(4)
subplot(2,1,1)
plot(T_comb,-calresponse_C10mM_E0pt2fmol_kcat95k_EnzDegComb_quarter*10^6,'r',T_comb,-
calresponse_C10mM_E0pt4fmol_kcat95k_EnzDegComb_quarter*10^6,'r',T_comb,-
calresponse_C10mM_E0pt6fmol_kcat95k_EnzDegComb_quarter*10^6,'r',T_comb,-
calresponse_C10mM_E0pt8fmol_kcat95k_EnzDegComb_quarter*10^6,'r',T_comb,-
calresponse_C10mM_E1pt0fmol_kcat95k_EnzDegComb_quarter*10^6,'r',T_comb,-
calresponse_C10mM_E1pt2fmol_kcat95k_EnzDegComb_quarter*10^6,'r',T_comb,-
calresponse_C10mM_E1pt4fmol_kcat95k_EnzDegComb_quarter*10^6,'r',X_1pt0fmol_Run1,TELISA
_1pt0fmol_Run1,'b')
axis([-2 30 -12.5 2])
subplot(2,1,2)
plot([0.2 0.4 0.6 0.8 1.0 1.2 1.4],RMSE_R1_1fmol,'-o')
```